Nanoscale Dynamic Nuclear Polarization in Force-Detected Magnetic Resonance

by

Namanish Singh

A thesis
presented to the University of Waterloo
in fulfillment of the
thesis requirement for the degree of
Master of Science
in
Physics (Quantum Information)

Waterloo, Ontario, Canada, 2024

© Namanish Singh 2024

Author's Declaration

I hereby declare that I am the sole author of this thesis. This is a true copy of the thesis, including any required final revisions, as accepted by my examiners.

I understand that my thesis may be made electronically available to the public.

Abstract

Nuclear magnetic resonance (NMR) has played a pivotal role in modern science with its ability to perform non-destructive imaging and spectroscopy of various systems. Despite this, NMR has been plagued by low detection sensitivity when trying to study nanoscale ensembles of spins, primarily due to the small thermal polarization of nuclear spins. Extending the capabilities of NMR to address nanoscale sample volumes would present exciting opportunities for studying biological systems, enabling high-resolution imaging of single biomolecules and virus particles. Over the years, a great deal of techniques to improve the detection sensitivity of the measurement apparatus have been made. Force-detected magnetic resonance is one such technique, that has demonstrated the capability to detect nanoscale ensembles of spins, where it has been successfully used to achieve three dimensional images of virus particles [1]. Nevertheless, further improvements are needed to achieve high resolution atomic scale imaging of nanoscale systems. Techniques such as dynamic nuclear polarization (DNP) have been widely implemented in traditional NMR experiments for boosting the signal, by transferring the comparatively larger polarization of electrons to surrounding nuclei [2]. The use of DNP in force-detected magnetic resonance platforms however, has remained relatively limited though [3]. Bringing DNP to nanoscale force-detected magnetic resonance setups would mark a significant next step in improving the detection sensitivity of nanoscale NMR experiments.

In this thesis, we discuss the implementation of DNP in a force-detected magnetic resonance experiment in order to achieve sensitivities needed to realize high resolution imaging of nanoscale spin ensembles. In these experiments, we observed a 100 fold enhancement in the proton thermal signal in a nanoscale droplet composed of trityl-OX063 radicals suspended in a sugar-water glassy matrix. We also compare the signal-to-noise ratio (SNR) boost this provides over measurements that rely upon statistical polarization, where we demonstrate a reduction in averaging time by a factor of 204. This work explores various tunable parameters to optimize the enhancement such as the proton and radical relaxation times. This work also investigates the role fast-relaxing paramagnetic defect centers from the surrounding environment play in reducing the radicals spin-lattice relaxation time, a crucial component for efficient DNP.

Acknowledgments

During my time pursuing an MSc degree, I have learnt more and progressed more as an individual than I ever thought possible. None of this would be possible without the many people who have supported me and guided me throughout my time here. First and foremost, I would like to thank my supervisor Raffi Budakian, who has been an incredibly positive force in my life. I have learned a great deal about science from him and am grateful for his constant willingness to engage with me and teach me new concepts. In particular, I have enjoyed our many long and creative discussions when solving new problems, where his creativity, diversity of thought, and knack for solving problems have been a constant source of inspiration and are skills I try to emulate.

My time in the Budakian group has been intellectually enlightening and has yielded great experiences. I would like to thank my collaborators and group members Sahand Tabatabaei, Pritam Priyadarsi, Pardis Sahafi, Ben Yager, and Daniel Tay, who have made this positive experience possible and from whom I have learned a great deal. In particular, I would like to thank Sahand and Pritam, who have been incredible mentors to me and with whom I have enjoyed many long, intellectually rewarding discussions. I would also like to thank them for the hand they have given me in satisfying my relentless curiosity.

I would also like to thank my mom and my dad, who have supported me for many years and who have sacrificed a great deal to allow me to pursue my passions.

I am also grateful for the learning environment and opportunities provided by the University of Waterloo and the Institute for Quantum Computing. The university's environment has created a diversity of knowledge that has always felt easily accessible, whether it be approaching other professors or students to discuss new ideas. Also, I have made many incredible friends at the university whom I would like to thank. Thank you to Jeremy, Trevor, Nandini, Matt, Ahmad, James, Kevin, and the many others whom I can not list for the memorable moments and time we have enjoyed together. Lastly, I would also like to thank my best friend and kindest person I know, Harleen, who has tolerated me these many years and provided a great deal of encouragement and support.

Dedication

To Harley

Table of Contents

Author's Declaration ii

Abstract iii

Acknowledgments iv

Dedication v

List of Figures viii

List of Tables xv

1 Introduction 1

1.1 Thesis Outline 5

1.2 Introduction to Magnetic Resonance 6

1.3 Thermal and Statistical Polarization 9

1.4 Dynamic Nuclear Polarization 12

1.5 Spin Diffusion 17

2 Experimental Setup and MAGGIC Protocol 21

2.1 Magnetic Resonance Force Microscopy 21

2.1.1 Silicon Nanowire Force Sensor 22

2.1.2 Samples . . . 22
2.1.3 Current-Focusing Field Gradient Source . . . 24
2.1.4 Experimental Setup . . . 27
2.2 Spin Detection Protocol . . . 29
2.3 Mean and Statistical Polarization Measurements . . . 32
2.3.1 Thermal Polarization Measurements . . . 32
2.3.2 Statistical Polarization Measurements . . . 34
2.4 Electronics . . . 38

3 Ramped Amplitude DNP Protocol **46**

4 Nanoscale DNP **50**
4.1 DNP measurements . . . 51
4.2 Comparison of Statistical Polarization and DNP Enhanced Thermal Polarization SNR . . . 55
4.3 Relaxation . . . 58
4.4 Surface-Induced Spin-Lattice Relaxation . . . 62
4.4.1 Software and Hardware Implementation of Spin Diffusion Simulations 68
4.5 Conclusion and Outlook . . . 75

References **76**

APPENDICES **85**

A Expectation value of the Random Telegraph Function **86**

B Code for Simulations of Surface Induced Spin Relaxation **88**
B.1 Random Spatial Distribution of Spins . . . 88
B.2 Pre-computing Spin Flip Probabilites . . . 91
B.3 Functions for Evolving the Spin States . . . 95

List of Figures

1.1 **Comparison of Thermal and Statistical Fractional Polarizations in Nanoscale Spin Ensembles. (A)** Calculated fractional polarization for N proton spins at T = 4.2 K and $B_0 = 0.32$ T the thermal polarization of the protons is $p_T = 7.78 \times 10^{-5}$. The maximum enhancement in proton polarization is given by $\gamma_e/\gamma_n = 658$ shown by the red line. The $N > N_c = 382$ the region (shaded) shows the region in which the DNP-enhanced thermal polarization exceeds the statistical. Note that the $N_c = (2kBT/\hbar\gamma_e B_0)^2$ in this case refers to the critical number of spins needed for the DNP-enahanced and statistical polarizations to be equal to one another. The second dashed line in the figure is used to represent the number of spins needed for the thermal and statistical polarizations to be equal. The top axis is calculated with a representative proton density of 10 nm^{-3} for organic samples, for example the Tobacco Mosaic Virus [1]. **(B)** The minimum enhancement required for the DNP-enhanced thermal polarization to exceed statistical as function of the number of proton spins in the detection volume. 11

1.2 **Tilted Rotating Frame Coordinate Axis.** 14

1.3 **NOVEL DNP Timing Diagram**. The DNP method begins by tipping the electron spins into the transverse plane with a $(\pi/2)_x$ pulse, after which a resonant spin locking drive is applied. The electron polarization is transferred to nearby protons and is allowed to repolarize for a period τ. By applying successive applications of the primitive, for a duration T_b, the proton polarization is built up in a sample. 16

2.1 **Trityl OX063 Polarizing Agent**. **(A)** SEM images taken of the nanodroplets attached to the tip of the SiNW showing the different morphologies of the samples. **(B)** Schematic of the SiNW positioned over the CFFGS device and the trityl-OX063 radical suspended in the glassy matrix. **(C)** Chemical structure of the trityl-OX063 radical. Due the symmetric structure of the radical, the electron spin exhibits low g-anisotropy and narrow linewidths [4]. 23

2.2 **Optical Images of CFFGS**. **(A)** Optical image of CFFGS composited from multiple snapshots of different regions. **(B)** Optical image of the central head section of the CFFGS, along with a gate wire that can be used to apply an electrostatic potential to the CFFGS. **(C, D)** SEMs of the CFFGS device with a minimum feature size of 150 nm. **(E)** Electrical connections are made to the CFFGS device with Al wirebonds connecting the device to a 50 Ω microstrip line on a carrier PCB. **(F)** Coaxial connections to the PCB are made with mini-SMP connectors. 25

2.3 **CFFGS Field Profiles**. **(A)** Simulated Rabi field contours at 100, 200, and 300 nm distances above the center of the constriction with $I_{pk} = 29$ mA. **(B)** Simulated detection gradients at different heights from the center of the CFFGS with $I_{pk} = 47$ mA. 26

2.4 **Schematic of the Experimental Setup** 28

2.5 **MAGGIC Measurement Protocol**. (**A**) Magnetic Resonance experiments are usually made up of successive blocks of some spin control sequence in which we encode some information of interest and are followed by measurement blocks which employ the MAGGIC protocol to detect the z-axis magnetization of the spin ensemble. (**B**) MAGGIC waveform primitive. (**C**) Spectrum of a spin signal and modulation sidebands generated by the CFFGS. 30

2.6 **Average Force time Record.** Average force time record (blue) and fitted data (red) of hyperpolarized proton spins. To increase the response time of the oscillator, the SiNW was damped to a quality factor of 900. 33

2.7 **Average Single Sided Displacement Spectral Density of Proton Spin signal.** The average single-sided displacement spectral density of the proton signal superimposed on the damped SiNW response. (Inset) The fitted baseline response of the SiNW has been subtracted and converted to force units to show the force spectral density of the signal. Both spectra are shown as a function of offset frequency δf from the carrier frequency, which is referenced to the mechanical resonance of the SiNW. 35

2.8 **Timing diagram for Statistical Polarization measurements** 36

2.9 **Block Diagram of Electronics** Schematic of the circuit used for spin manipulation and detection. The circuitry for generating gradient modulation waveform is shown in the LF section. The RF pulses applied to the protons are generated via the circuitry in the NMR section. Both the RF and LF pulses are driven differentially to minimize the electrostatic coupling to the sample and are combined using a passive filter network. The microwave electronics used for electron control are shown in the ESR section, are driven single ended and are combined with the LF and RF pulses using the diplexer. 39

2.10 **BiasTee Filter** Measured LF and RF responses through the bias-Tee network. To measure the low pass response of the circuit V_{LF} was excited while the V_{RF} port was terminated to ground. Similarly, the high pass response was measured by exciting V_{RF} and terminating the V_{LF} port. 40

2.11 **Frequency Upconversion.** IQ mixer multiples LO with the baseband IQ signals and combines them to generate an output at $\omega_{LO}+\omega_{IF}$. A non-ideal IQ mixer can also generate unwanted sidebands at harmonics of ω_{IF} as well as spectral content at ω_{LO} (LO leakage) 41

2.12 **Amplitude and Phase Response of Reactel 8CX1-9200-X400 Filter. (A)** Amplitude Response. The passband of the filter is designed to be between 9 and 9.4 GHz. **(B)** Phase Response. 42

2.13 **Phase Noise of LO supplied by nardarmiteq.** 43

2.14 **Output power of Microwave Electronics circuit.** Measured output power at the output of the diplexer as a function of the input power incident to the IQ mixer. The measured $P_{1\text{dB}}$ compression point is at 29.44 dBm. . 44

3.1 **Double Quantum and Zero Quantum Transitions**. The eigenstates trajectory calculated from Equation 1.33 and 1.34. The Rabi field is swept adiabatically through the Hartmann-Hahn matching frequency (shown in red arrows). The state adiabatically follows the trajectory from the $|\uparrow\uparrow\rangle \leftrightarrow |\downarrow\downarrow\rangle$ for the double quantum transition, and $|\downarrow\uparrow\rangle \leftrightarrow |\uparrow\downarrow\rangle$ for the zero quantum transition. The energy splitting between the two eigenstates is also shown, where at $\omega_{1S} = \pm\omega_{0I}$, the splitting is $B/2$, where B is the pseudo-secular hyperfine coupling. Note, that the $|\uparrow\downarrow\rangle, |\downarrow\uparrow\rangle$ states are left invariant during the double quantum transition and similarly the $|\uparrow\uparrow\rangle, |\downarrow\downarrow\rangle$ states are left invariant during the zero quantum transitions. 47

3.2 **RA-NOVEL. (A)** RA-NOVEL waveform primitive applied to the electrons consisting of an adiabatic half passage (AHP) to the tip the spins into the transverse plane, followed by an electron spin locking pulse that is swept to 0 over a duration T_{ramp}, followed by repolarization of the electrons for a time T_{pol}. By repeating the waveform N times, the proton polarization in the sample can be built up for a time T_b, which is limited by the T_{1p} of the protons. **(B)** The time at which the Hartmann-Hahn matching condition is met (t_{HH}) for an electron-proton pair at a distance z from the center of the CFFGS ($x = 0, y = 0$) during the ramp waveform. **(C)** Rabi contours during different stages of the ramp. The yellow contour outlines where the Hartmann-Hahn condition is met. As ω_{1S} is swept through the matching condition, an electron-proton pair (white circle) will undergo adiabatic transfer of polarization. Due to the inhomogeneity in the B_1 field spin furthest away from the CFFGS undergo exchange at earlier times of the ramp than spins near the sample tip. The arrows shown indicate the spin states in the tilted rotating frame. 48

4.1 **DNP Measurements. (A)** Pulse sequence used for DNP measurements. The proton polarization is first scrambled using $(\pi/2)_x$ and $(\pi/2)_y$ pulses with a dephasing time in between. Repeated applications of the RA-NOVEL waveform primitive are then applied to the electrons for a build-up time T_b before measuring the magnetization of the proton spins. **(B)** Measured expectation values of the hyperpolarized (58 averages) and thermal (7080 averages) signals for Sample A. The data is fitted to a model of the mechanical response of the SiNW (dashed lines), with the initial rise in the data being due to the finite bandwidth of the oscillator. The signals decay with a spin correlation time $\tau_m = 31.9(2)$ ms. (Inset) DNP enhanced proton polarization as a function of build time (58 averages/point). **(C)** The DNP enhancement is shown for different T_{pol} and T_{ramp} for an optimal buildup time $T_{b,opt} = 7.7$ s (58 averages/point). (Inset) The enhancement per ramp depicts the increase in efficiency and saturation of polarization transfer for longer T_{pol} and T_{ramp}. We found the maximum enhancement $\eta = 105(8)$ in proton polarization with a $T_{\text{pol}} = 10.24$ ms and $T_{\text{ramp}} = 16$ μs. 53

4.2 **SNR Comparison of DNP Enhanced and Statistical Polarization Experiments.** **(A)** Measured time-domain Fourier encoding data for **(A)** statistically polarized and **(C)** hyperpolarized proton spins in sample A. The corresponding images in the Rabi frequency domain are shown in **(B)** and **(D)**, with the top axis indicating the distance from the surface of the CFFGS ($z = 0$) along the center of the constriction ($x = y = 0$ line). The frequency resolution of each image is 50 kHz. The shaded regions indicate the standard deviation of the acquired data (open circles) for each point in the time record, and the corresponding Rabi frequency distributions. The insets show the pulse sequence used for the two types of measurement. We applied a constant amplitude excitation at ω_{0S} to decouple the electrons while acquiring the proton signal. The decoupling procedure resulted in extending the proton spin correlation time from 31.9 ms to 135.6 ms during the acquisition period. The differences observed in the statistical and hyperpolarized distributions stem from how each spin interacts with the detection gradient. In statistical polarization, the contribution of a spin at position $\mathbf{r}$ to the signal is proportional to $G^2(\mathbf{r})$, while for the hyperpolarized signal, $G(\mathbf{r})$. Consequently, spins closer to the CFFGS have a more pronounced impact on the statistically polarized image, leading to increased spectral content at higher Rabi frequencies in **(B)** compared to **(D)**. 56

4.3 **Relaxation Times.** Spin relaxation data for Sample A, with associated pulse sequences. **(A)** T_{1e} measurement, with inversion recovery pulse sequence. **(B)** Electron T_{2e}^* measurement using a Ramsey experiment with a time-proportional phase increment (TPPI) scheme, ($\omega_{\mathrm{TPPI}}/(2\pi) = 30$ MHz). **(C)** Electron $T_{1\rho e}$ measurement with a resonant constant-amplitude drive. **(D)** Proton T_{1p} measurement by measuring the decay in the longitudinal magnetization of the hyperpolarized proton ensemble. **(E)** Proton T_{2p}^* measurement using a Ramsey experiment on the hyperpolarized proton ensemble with $\omega_{\mathrm{TPPI}}/(2\pi) = 80$ kHz. **(F)** Proton T_{2p} measurement with a σ_z decoupling sequence on the proton hyperpolarized ensemble. 59

4.4 **Thermometry Meausurements for 1.3 mM Reference Sample. (A)** (right axis) measured thermal displacement power as a function of the incident laser power, (left axis) extrapolated SiNW temperature. The operating light level of the measurements for this sample is indicated by the blue data point. (**B**) Measurement of the thermal electron spin polarization as a function of the temperature of the SiNW. **(C)** T_{1e} measured at different tip-surface distances from the CFFGS. The T_{1e} remains consistent at different heights. 62

4.5 **Spin Diffusion Simulation of Surface Induced Spin Lattice Relaxation**. **(A)** Visualization of spin states at different points in T_{1e} decay for Sample A. At $t = 0$, the sample and surface defects are fully polarized. At $t = 2.5$ ms, the fast relaxing spins on the surface of the SiNW have reached thermal equilibrium. At $t = 21$ ms, the bulk polarization has reached the $1/e$ point, and we observe an increase in the number of spins in the down state. At $t = 81.2$ ms ($\sim 3T_{1e}$), the sample has reached thermal equilibrium. The simulated fractional polarization as a function of time for sample A is shown with $T_{1e} = 21$ ms. **(B)** Spin-lattice relaxation times for samples A, B, and C and the reference sample for different defect densities on the surface of the SiNW. 67

4.6 **Caption next page.** 70

4.6 (Previous page.) **Flow Chart of Simulation Code.** In the Python section, we pre-computed the dipole-dipole mediated transition probabilities for all spin pairs within a minimum radius $r_{\min}$ as described in Section 4.4, and store them in a 1D array (`flip_array`). We also stored the indices of the (i, j) interacting spin pairs for the corresponding transition probability. For example, the 0^{th} entry in `flip_array` may correspond to the probability of a spin flip between the 4^{th} and 10^{th} labelled spins in our geometry. As a result, the 0^{th} entry of `i_array` and `j_array` will be 4, and 10 respectively. We also assign each spin its own intrinsic T_1 based on whether the spin resides in the bulk sample or on the surface of the SiNW. The arrays are then exported to binary files. In the GPU program, we begin by loading the arrays from the binary files. The simulation is conducted for a simulation time T with step size $\delta t = 1$ ns. A pseudo-random number generator is then used to generate $M = \text{len}$`(flip_array)` random numbers in parallel. The spin-flip conditions are also evaluated in parallel, where the spin states are swapped if the necessary conditions are met. A similar procedure was followed for evaluating spin flips due to the T_1 process. After each time step, the gradient-weighted magnetization is calculated and stored in a text file. 71

4.7 **Overview of GPU Architecture Schematic.** Each thread is responsible for generating its own stream of random numbers. The number of threads is equal to the number of pairwise interactions between the spins that are being considered in the simulation. Each random number X is compared to the $\mathbb{P}$(flip) of the spin pair. If $X < \mathbb{P}$(flip) then the spin states are swapped. Different threads are organized into thread blocks that share memory resources, and multiple blocks are organized into a grid. 72

List of Tables

2.1 **Constituent table,** including all the components used to prepare the measured samples. 24

4.1 **Summary of nanoscale DNP results**, including measured DNP enhancements and spin relaxation times. 52

4.2 **Electron and proton relaxation times** for the measured samples. T_{2p} and T_{2p}^{*} were not measured for sample D. 60

4.3 **Parameters used for Semi-Classical Spin Diffusion Simulations.** Ref. sample refers to the 1.3 mM sample used for investigating different electron relaxation mechanisms. 66

Chapter 1

Introduction

The development of nuclear magnetic resonance (NMR) has revolutionized modern science, finding applications in fields as diverse as medical imaging, studying condensed matter systems, and molecular structure determination. NMR has become an especially powerful tool in chemistry and biology, enabling the study of complex structures and dynamics of proteins and viruses. Traditionally, resolving the spatial structure of singular biomolecules has relied upon X-ray scattering or cryogenic electron microscopy. Though powerful, these techniques can be hindered by challenges such as radiation-induced sample damage limiting achievable resolutions, difficulties in sample preparation, and a lack of chemical information about the sample [5]. Conversely, the non-destructive nature of NMR allows for both imaging and spectroscopy of materials that can be used for imaging biological samples, revealing information about their chemical environments and the spatial configurations of atoms, ultimately providing insights into their function [6]. For example, NMR has been used to measure the atomic scale distances between spin labels attached to different regions of a protein, enabling the study of conformational changes in protein structure [6]. This has provided information on how proteins fold, bind, and interact with other molecules, which is important for drug development.

Despite this, complete three-dimensional imaging of single macromolecules and nanoscale complexes remains a challenge, due to the low detection sensitivity of NMR. Nanoscale magnetic resonance imaging (nanoMRI) has been developed over recent decades to extend the capabilities of NMR to the nanoscale [1, 7–14]. Techniques used in nanoMRI include optically-detected magnetic resonance using nitrogen-vacancy (NV) centres, and magnetic resonance force microscopy (MRFM). MRFM is a mechanical detection approach to nanoMRI that couples large magnetic field gradients to a spin sample generating a force on it. This force is coupled to the displacement of a ultra-sensitive nano-mechanical can-

tilever, and measured using optical interferometry [15]. The detection sensitivity of MRFM surpasses that of traditional NMR where a coil is used to measure the free induction decay signal of spins is measured. As a result, the detection sensitivity of MRFM, can be much greater than traditional inductively detected signals in NMR. MRFM has been successfully employed to image nanoscale ensembles, such as imaging the tobacco mosaic virus in three-dimensions with a spatial resolution of 10 nm, and has even demonstrated the sensitivity to detect single electron spins [1, 12].

The detection sensitivity in MRFM is ultimately limited by 1) the spin polarization in the sample, 2) the mechanical noise or dissipation of the cantilever, 3) the strength of the magnetic field gradients needed for spin detection, 4) the cantilever force noise generated from fluctuating electric fields in a nearby surface. To improve force sensitivities, ultra-low dissipation nano-mechanical cantilevers and membranes [16–19] have been developed, with thermal force noise as low as 90 zN/$\sqrt{\text{Hz}}$. Additionally, magnetic field sources capable of generating large gradients as high as 10^7 T/m [7, 20, 21] have been developed. In the MRFM experiments presented in this work, we make use of silicon nanowires (SiNWs) as nano-mechanical oscillators, as they exhibit low mechanical dissipation, and are well suited for use as highly sensitive force sensors [7, 18]. In typical MRFM experiments, permanent static field gradient sources are used to generate the magnetic field gradients needed for spin detection. This however, hinders the ability of such experiments to utilize sophisticated NMR spin control techniques that can be used to improve imaging resolution [3]. In contrast, we utilize a current-focusing field gradient source (CFFGS) which passes current through a narrow metallic constriction in order to generate large time-dependent magnetic field gradients [7, 13]. Importantly, as we will discuss later, the CFFGS device can be used to apply and separately optimize the gradient pulses used for spin detection, and spin encoding pulses used for imaging experiments. Such devices have been used to successfully implement angstrom-resolution Fourier imaging experiments, utilizing dynamical decoupling sequences to extend spin coherence times, which is often an important component for high-resolution imaging [14, 22]. Despite these advancements, further enhancements are needed for nanoMRI to achieve its goal of full three-dimensional imaging of nanoscale ensembles with atomic resolution. For example, the thermal polarization of protons at 1 K and 3 T is roughly only 0.08%.

In conventional magnetic resonance, the strength of the detected signal is directly proportional to the mean spin polarization of the samples. Even at cryogenic temperatures, and large static magnetic fields, the average nuclear spin polarization is very small, leading to low detection sensitivity. For example, the average fractional polarization of protons at 1 K and 3 T is roughly only 0.08%. Thus, to compensate for the relatively small fraction of polarized spins, the total number of spins in the sample must be large in order to improve

the detection sensitivity and boost the signal-to-noise ratio (SNR) of the NMR signal. As a result, this limits its applicability when imaging nanoscale ensembles where the number of spins in the sample volume is small. Comparatively, the mean spin polarization of electrons relative to protons is roughly $\gamma_e/\gamma_p \sim 658$ times larger, owing to a larger magnetic moment. Dynamic nuclear polarization (DNP) is a technique that has been well developed in traditional NMR, to transfer this larger polarization of electron spins to nearby nuclei through their hyperfine interactions, thereby providing large improvements in detection sensitivity, and extending the capabilities of NMR to detect smaller sample volumes. Implementing DNP alongside force-detected magnetic resonance would further push the limits of detection sensitivity and spatial resolution, enabling the study of even smaller or more dilute nanoscale systems. In a typical DNP experiment, a sample is doped with a polarizing agent, that contains an unpaired electron, which is used to transfer the electron polarization to surrounding nuclei. Once the transfer is completed, nuclear spin diffusion is responsible for distributing the polarization throughout the sample. Through successive repetitions of the polarization transfer followed by nuclear spin diffusion, the polarization of nuclei in the bulk sample can be built up to at most, the ratio of the gyromagnetic ratios of the different spin species, assuming the nuclear polarization doesn't decay due to relaxation processes.

Previous work done in extending DNP to MRFM was done by Thuber et al. who achieved an enhancement of 12 in the mean nuclear spin polarization [23]. This work utilized optically pumped DNP to polarize gallium nuclei in a GaAs sample. The work by Isaac et al. further demonstrated the use of cross effect DNP to hyperpolarize polystyrene films doped with TEMPAMINE free radicals [3]. The enhancement achieved here at 4 K and 0.6 T were between 10 - 20 [3]. The experiment presented by Isaac et al. used a permanent magnet attached to the tip of a silicon cantilever as the field gradient source used for spin detection [3]. Importantly, this static field gradient source used for spin detection also presents challenges that the authors note. Primarily, the inability to turn off the gradient during the DNP process makes it difficult to achieve large enhancements in proton polarization throughout the sample [3]. In addition, the authors note another limitation of their experimental setup was the ability to suspend nuclear spin diffusion, which as the authors note limits the applicability of using their DNP method for doing high-resolution nanoscale imaging [3]. As mentioned previously, in our experiments since the magnetic fields generated depend only on the time-dependent current passing through the CFFGS. Hence, it enables us to separately optimize and apply pulses used for DNP, spin encoding, and spin detection [24] thereby, overcoming the challenges presented in previous DNP MRFM works which were limited to low DNP enhancements.

In NMR, for bulk samples, we typically detect the average population difference in the

number of up and down spins, in the presence of a large static magnetic field. This is often referred to as the the mean, thermal, or Boltzmann polarization. In nanoscale ensembles however, statistical fluctuations in the number of up and down spins (statistical polarization) are usually much larger than the mean polarization. As a result, force-detected magnetic resonance platforms typically measure the statistical polarization when working with nanoscale spin systems as it offers two key advantages 1) better SNR when working with nanoscale ensembles due to the larger statistical polarization, and 2) in comparison to measurements of the thermal polarization that require a constant overhead time on the order of the spin-lattice relaxation time T_1 for the spins to reach thermal equilibrium, statistically polarized samples can be continuously measured, enabling higher acquisition rates. As a result, in order for DNP to provide an SNR advantage in measurements involving nanoscale ensembles, it must provide a sufficiently large enhancement to the thermal polarization to overcome not only the larger statistical polarization, but also the higher acquisition rate of a statistically polarized signal.

As previously mentioned, DNP transfers the polarization of electrons to nearby nuclei. Following this transfer, the electron spin polarization re-equilibrates on a timescale governed by the spin-lattice relaxation time T_{1e}. The spin-lattice relaxation time determines how quickly electron spins return to thermal equilibrium, impacting the frequency at which polarization can be effectively transferred to protons. Consequently, this affects the overall buildup of nuclear polarization. In bulk DNP, the role T_{1e} plays in the DNP efficiency has been explored before [25,26]. In nanoscale ensembles, a larger fraction of the spins can be coupled to spins in the sample boundary, which can consist of paramagnetic defect spins. As a result, surface defects can significantly affect the spin-lattice relaxation times, or create local field inhomogeneities, all of which affect the overall DNP efficiency. In our experiment in particular, our samples are attached to the surface of a SiNW. On the surface of the SiNW is a Si/SiO_2 interface at which there are unterminated bonds between the Si and and SiO_2 layers. These give rise to paramagnetic defect centers with short spin-lattice relaxation times [27,28]. Strong couplings to these defect centers can affect the relaxation time of the bulk spins affecting the efficiency of the DNP process. In this work, we investigate this mechanism and conduct simulations to verify whether interactions with these defect centers is significant in the DNP process.

The DNP experiments presented in this thesis use trityl-OX063 free radicals as the polarizing agent. We use these radicals as they are known to exhibit narrow linewidths that make them useful for the pulsed DNP [25,29,30]. Additionally, trityl-OX063 radicals are highly soluble in water, and have demonstrated good stability in biological samples [30]. The radicals are encapsulated in a sugar-water matrix which in prior works has been used as a cyroprotectant for biological samples that prevents the formation of ice crystals

at cryogenic temperatures [31, 32]. The DNP experiments presented, use the radicals to hyperpolarize proton spins in the sugar-water matrix. This sample was prepared for varying concentrations of the trityl radicals to observe the dependence the of the DNP enhancements on electron and proton concentrations.

This dissertation explores the implementation of pulsed DNP experiments in a force detected magnetic resonance platform to achieve large enhancements in thermal polarization. We explore the potential of DNP to provide an SNR advantage over measurements made with statistical polarization, thereby extending force detected magnetic resonance as a platform for realizing high-resolution imaging of nanoscale ensembles. The thesis will also explore the different phenomena that affect the performance of the DNP experiment such as heating of the sample, surface induced spin-lattice relaxation of electrons, electronic induced noise in the system, and concentration and size of trityl OX063 droplets, among other factors.

The work presented in this thesis was conducted in collaboration with the author's colleagues and supervisor Sahand Tabatabaei, Pritam Priyadarsi, Daniel Tay, and Raffi Budakian. The author's contribution primarily consisted of characterization of the electronics necessary for proton and electron spin control. This includes programming of the arbitrary waveform generators (AWGs) and ensuring synchronized generation of all output pulses. I also conducted spin diffusion simulations that were developed to model the role paramagnetic defects on the surface of the SiNW play in spin-lattice relaxation of bulk spins in our samples. Alongside my colleagues, I was involved in all measurements of the data presented in this thesis. Greater details on the challenges and solutions of some these topics is provided in the thesis. Some areas not discussed in the thesis but in which I was also involved include developing software for the attocube nano-positioners used to align the CFFGS and SiNW devices in our experiment, as well as the mechanical design of the components used in our experimental probe.

1.1 Thesis Outline

- Chapter 1 provides an introduction to the theory of magnetic resonance. This section introduces the rotating wave approximation (RWA) and the interaction frame Hamiltonian that is used throughout the dissertation. A brief background on the difference between thermal and statistical polarization is provided, along with the theory of nuclear orientation via electron spin locking (NOVEL) DNP – the protocol utilized in the DNP measurements. This is followed by a brief discussion on the role of spin diffusion in the dynamics of DNP process.

- Chapter 2 provides details of the experimental setup and a brief background into the measurement protocol used in our force-detected magnetic resonance platform. Some discussion around the benefits of measuring statistical over thermal polarization is provided. This section then touches upon the sample concentrations used in the measurement and characterization of the electronics used for ESR/NMR pulse generation.

- Chapter 3 discusses a detailed analysis of a modified version of the the NOVEL DNP protocol, ramped amplitude NOVEL (RA-NOVEL), which is robust to spatial variations in applied fields and allows for efficient adiabatic transfer of polarization.

- Chapter 4 presents the measured DNP data and 1D Fourier image taken with the DNP-enhanced and statistical polarizations. We use this to compare the signal-to-noise-ratio (SNR) of the two schemes and show that the DNP-enhanced polarization can provide a 200-fold reduction in averaging time compared to statistical polarization to achieve the same image quality. In this section, we also discuss the optimal parameters needed for maximum enhancement DNP. Importantly, we show that our measured electron spin-lattice relaxation times are significantly faster than values reported in the literature for OX063 radials in bulk. We investigate different sources that may be responsible for the accelerated relaxation, and provide in depth simulations of surface-induced spin-lattice relaxation to explain this discrepancy. Finally, we also detail future directions for DNP in nanoMRI.

1.2 Introduction to Magnetic Resonance

For any closed quantum system, the time evolution of a pure state $|\psi(t)\rangle$ is given by the Schrödinger equation

$$i\hbar\frac{d}{dt}|\psi(t)\rangle = H(t)|\psi(t)\rangle\,, \tag{1.1}$$

where $H(t)$ is the Hamiltonian. Equivalently, we can describe the evolution of the system with a unitary operator $U(t)$ which maps the initial state $|\psi_0\rangle$ to a state at time t as $|\psi(t)\rangle = U(t)|\psi(0)\rangle$, and has the property $U(t)U^\dagger(t) = U^\dagger(t)U(t) = \mathbb{1}$, where $\mathbb{1}$ is the identity operator. Accordingly, Equation 1.1 can be recast into an equivalent initial value problem for $U(t)$:

$$\frac{d}{dt}U(t) = -iH(t)U(t), \tag{1.2}$$

with the initial condition $U(0) = \mathbb{1}$. Note we have chosen to set $\hbar = 1$ for convenience such that we measure energy in angular frequency units, and we will follow this convention throughout the thesis unless otherwise mentioned. In the case where the Hamiltonian is time independent, we can express the solution of 1.2 as $U(t) = e^{-iHt}$. However in general, if the Hamiltonian is time dependent and does not commute with itself at all times, then the unitary becomes

$$U(t) = \text{Texp}\left[-i\int_0^t dt'\ H(t')\right], \tag{1.3}$$

where Texp[·] refers to a time ordered exponential [33].

In general, a closed form solution for the unitary may not exist. The unitary can be calculated using a Dyson series expansion [34]

$$U(t) = \sum_{n=0}^{\infty}(-i)^n \int_0^t dt_1 \ldots \int_0^{t_{n-1}} dt_n \prod_{i=1}^{n} H(t_i), \tag{1.4}$$

For an exact expression of $U(t)$, all terms in the expansion must be considered. However, if the Hamiltonian were rewritten in a frame where the norm of each successive term in the expansion is smaller than the previous term, truncating the expansion becomes a good approximation. In the case where the Hamilton $H(t)$ is close to an exactly solvable Hamiltonian $H_0(t)$, we can transform $H(t)$ to the *interaction frame* of $H_0(t)$ with $V(t) = e^{-iH_0t}$. The Hamiltonian $H(t)$ can be decomposed as $H(t) = H_0(t) + \delta H(t)$, where $\delta H(t)$ is a small perturbation acting on the system, and $\|\delta H(t)\| \ll \|H_0(t)\|$, where the norm of an operator A is given by the Frobenius norm $\|A\| = \sqrt{\text{Tr}(A^\dagger A)}$. For simplicity we assume that H_0 is time independent. We will define a new state in the interaction frame as $|\psi'(t)\rangle = V^\dagger(t)\,|\psi(t)\rangle$. Substituting $|\psi'(t)\rangle$ into Equation 1.1

$$\begin{aligned}
i\frac{d}{dt}(V(t)\,|\psi'(t)\rangle) &= (H_0 + \delta H)V(t)\,|\psi'(t)\rangle \\
H_0V(t)\,|\psi'(t)\rangle + iV(t)\frac{d}{dt}\,|\psi'(t)\rangle &= (H_0 + \delta H)V(t)\,|\psi'(t)\rangle \\
i\frac{d}{dt}\,|\psi'(t)\rangle &= (-H_0 + V^\dagger(t)H_0V(t) + V^\dagger(t)\delta HV(t))\,|\psi'(t)\rangle\,.
\end{aligned} \tag{1.5}$$

Since $[H_0, e^{-itH_0}] = 0$, Equation 1.5 simplifies to

$$i\frac{d}{dt}\,|\psi'(t)\rangle = \underbrace{V^\dagger(t)\delta HV(t)}_{H_{\text{int}}}\,|\psi'(t)\rangle\,, \tag{1.6}$$

which is known as the Schrödinger equation in the interaction frame, which describes the dynamics under $H_{\text{int}} = V^{\dagger}(t)\delta H V(t)$.

A spin-1/2 particle placed in a magnetic field $\mathbf{B}(t)$ will undergo an energy splitting according to Zeeman Hamiltonian

$$H(t) = -\boldsymbol{\mu} \cdot \mathbf{B}(t), \tag{1.7}$$

where $\boldsymbol{\mu}$ is the magnetic moment of the particle and can be written in terms of the spin angular momentum operators, $\boldsymbol{\mu} = \gamma(S_x, S_y, S_z)$ with γ being the gyromagnetic ratio. Protons have a gyromagnetic ratio $\gamma_p/(2\pi) = 42.577$ MHz/T, and for electrons $\gamma_e/(2\pi) =$ 28 024 MHz/T, around 658 times larger. Throughout this thesis, we will use $\mathbf{I}$ and $\mathbf{S}$ to denote the spin angular momentum operators of nuclei and electrons, respectively.

The Hamiltonian governing a spin-1/2 particle subject to a static magnetic field $B_0\hat{\mathbf{z}}$ is $H = -\gamma B_0 I_z$, where $\omega_0 = \gamma B_0$ is known as the Larmor frequency which is the rate of precession of the magnetic moment around a static field. The eigenstates of the Zeeman Hamiltonian can be denoted as $|\uparrow\rangle, |\downarrow\rangle$ with eigenvalues $-\omega_0/2$, and $\omega_0/2$.

We will now show that the phenomena of magnetic resonance occurs when an oscillating field perpendicular to the static field is applied at a frequency ω_0, resulting in transitions between the $|\uparrow\rangle, |\downarrow\rangle$ states of the system. Consider a $\mathbf{B}(t)$ vector with the following form

$$\mathbf{B}(t) = B_0\hat{\mathbf{z}} + 2B_1 \cos(\omega_T t)\hat{\mathbf{x}} \tag{1.8}$$

ω_T being the frequency of the AC magnetic field, and B_1 is called the Rabi field. The corresponding Hamiltonian is

$$H(t) = -\omega_0 I_z - 2\omega_1 \cos(\omega_T t) I_x, \tag{1.9}$$

where $\omega_0 = \gamma B_0$ is the Larmor frequency, and $\omega_1 = \gamma B_1$ is known as the Rabi frequency.

To solve Equation 1.1 with the Hamiltonian of Equation 1.9 we transform to a frame rotating around the static field with frequency ω_T, sometimes referred to as the *transciever* or *rotating frame*, with a unitary $V(t) = e^{i\omega_T I_z t}$. The magnitude of the static field in magnetic resonance experiments is usually much greater, on the order of a few Tesla, whereas the Rabi field is usually a few hundred Gauss, $|\omega_1| \ll |\omega_0|$. We can rewrite the Hamiltonian as

$$H(t) = \underbrace{-\omega_T I_z}_{H_0} \underbrace{-(\omega_0 - \omega_T) I_z - 2\omega_1 \cos(\omega_T t) I_x}_{\delta H}, \tag{1.10}$$

We assume that the transmitter frequency ω_T is close to the Larmor frequency such that $\|\delta H\| \ll \|H_0\|$ holds. We can transform the Hamiltonian to the rotating frame as follows

$$\begin{aligned}\tilde{H}(t) &= V^\dagger(t)\delta H(t)V(t) \\ &= e^{-i\omega_T I_z t}(-(\omega_0-\omega_T)I_z - 2\omega_1\cos(\omega_T t)I_x)e^{i\omega_T I_z t} \\ &= e^{-i\omega_T I_z t}(-(\omega_0-\omega_T)I_z - \omega_1(e^{i\omega_T t}+e^{-i\omega_T t})I_x)e^{i\omega_T I_z t}, \end{aligned} \tag{1.11}$$

rewriting Equation 1.11 in terms of raising and lowering ladder operators, $I_\pm = I_x \pm iI_y$, and using the fact that $e^{-i\theta I_z}I_\pm e^{i\theta I_z} = e^{\mp i\theta}I_\pm$ we have

$$\tilde{H}(t) = -\Delta\omega I_z - \frac{\omega_1}{2}(e^{i\omega_T t}+e^{-i\omega_T t})(e^{-i\omega_T I_z t}(I_+ + I_-)e^{i\omega_T I_z t}) \tag{1.12}$$

$$= -\Delta\omega I_z - \frac{\omega_1}{2}(e^{i\omega_T t}+e^{-i\omega_T t})(e^{-i\omega_T t}I_+ + e^{i\omega_T t}I_-) \tag{1.13}$$

$$= -\Delta\omega I_z - \frac{\omega_1}{2}(I_+ + I_- + e^{2i\omega_T t}I_- + e^{-2i\omega_T t}I_+) \tag{1.14}$$

$$\approx -\Delta\omega I_z - \frac{\omega_1}{2}(I_+ + I_-) \tag{1.15}$$

$$\approx -\Delta\omega I_z - \omega_1 I_x, \tag{1.16}$$

where $\Delta\omega = \omega_0 - \omega_T$. In Equation 1.14 we have dropped the time dependent terms rapidly oscillating terms that average out over a timescale greater than the Larmor period. This is known as the *rotating wave approximation* (RWA) or the *secular approximation*, and is a good approximation so long as $|\omega_1| \ll |\omega_0|$ and $|\Delta\omega| \ll |\omega_0|$. In the case where $\omega_T = \omega_0$, the so called resonance condition in magnetic resonance, the Hamiltonian is $\tilde{H}(t) = -\omega_1 I_x$. From this we can see that the state $|\psi'(t)\rangle$ oscillates between the $|\uparrow\rangle, |\downarrow\rangle$ states at the Rabi frequency ω_1.

1.3 Thermal and Statistical Polarization

In most magnetic resonance experiments, the measured spin signal is proportional to the mean polarization of the spins at thermal equilibrium, sometimes referred to as the Boltzmann polarization. However, as the size of the spin ensembles decreases, statistical fluctuations in the spin polarization, referred to as *statistical polarization*, can exceed the mean polarization [1, 35]. As we discuss later on, to extract information about the spin system through these statistical fluctuations, we often measure other statistics of the polarization, such as the variance, spectral density or correlations.

The equilibrium state of a single spin-1/2 particle at temperature T is described by a Boltzmann distribution expressed by the density matrix $\rho = \exp(-\beta H)/\mathcal{Z}$, where $\beta = 1/k_B T$, k_B is the Boltzmann constant, T is the temperature in Kelvin, and $\mathcal{Z} = \mathrm{Tr}\{\exp(-\beta H)\}$. Since magnetization is an extensive quantity, the mean magnetization is $M_z = N\mathrm{Tr}\{\sigma_z \rho\}$ and the variance is $\sigma^2_{M_z} = N\left(\mathrm{Tr}\{\sigma_z^2 \rho\} - \mathrm{Tr}\{\sigma_z \rho\}^2\right)$. In most magnetic resonance experiments, the energy splitting between eigenstates due to the static field is much smaller than the thermal energy, $\hbar\gamma B_0 \ll k_B T$. In this *high temperature limit*, we can Taylor expand and truncate ρ as

$$\rho = \frac{1}{2}\left(\mathbb{1} + \frac{\varepsilon\sigma_z}{2} + \mathcal{O}(\varepsilon^2)\right) \tag{1.17}$$

where $\varepsilon = \hbar\gamma B_0/k_B T$. We then find that

$$M_z = N\frac{\hbar\gamma B_0}{2k_B T} \tag{1.18}$$

$$\sigma^2_{M_z} = N. \tag{1.19}$$

The fractional thermal and statistical polarization are defined as $M_z/M_{100\%} = \hbar\gamma B_0/2k_B T$ and $\sigma_{M_z}/M_{100\%} = 1/\sqrt{N}$, where $M_{100\%} = N$. From Equations 1.17 and 1.19, the number of spins in the ensemble can be expressed in terms of the ratios of M_z and σ_{M_z} as

$$N = \left(\frac{2k_B T}{\hbar\gamma B_0}\right)^2 \left(\frac{M_z}{\sigma_{M_z}}\right)^2. \tag{1.20}$$

From Equation 1.20, the critical number of spins needed for the thermal and statistical polarization to be equal is $N_{cT} = (2k_B T/\hbar\gamma B_0)^2$. Figure 1.1 provides a comparison of the fractional thermal and statistical polarization's for protons at $B_0 = 0.32$ T [24].

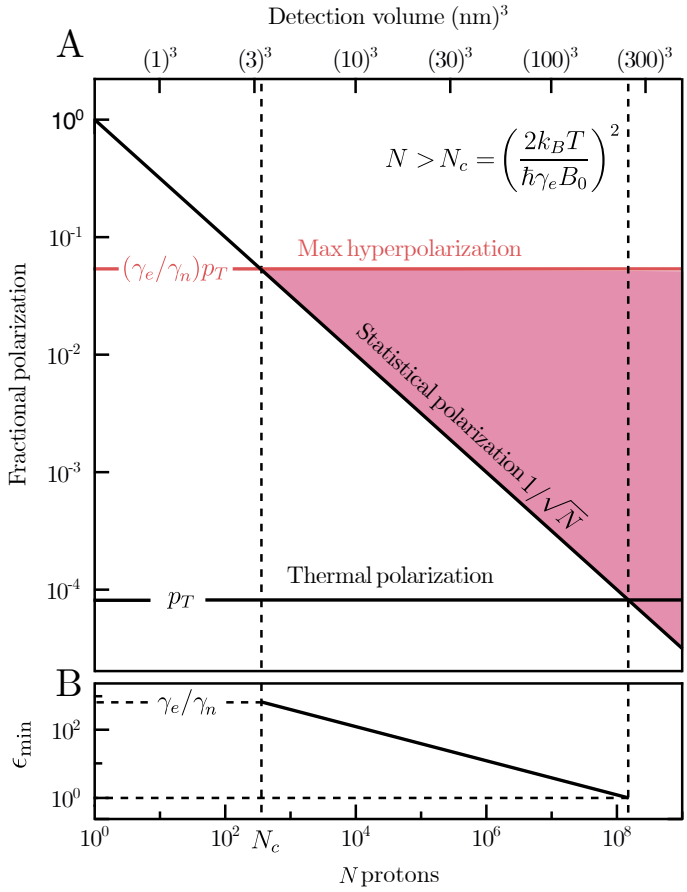


Figure 1.1: **Comparison of Thermal and Statistical Fractional Polarizations in Nanoscale Spin Ensembles. (A)** Calculated fractional polarization for N proton spins at T = 4.2 K and $B_0 = 0.32$ T the thermal polarization of the protons is $p_T = 7.78 \times 10^{-5}$. The maximum enhancement in proton polarization is given by $\gamma_e/\gamma_n = 658$ shown by the red line. The $N > N_c = 382$ the region (shaded) shows the region in which the DNP-enhanced thermal polarization exceeds the statistical. Note that the $N_c = (2kBT/\hbar\gamma_e B_0)^2$ in this case refers to the critical number of spins needed for the DNP-enahanced and statistical polarizations to be equal to one another. The second dashed line in the figure is used to represent the number of spins needed for the thermal and statistical polarizations to be equal. The top axis is calculated with a representative proton density of 10 nm^{-3} for organic samples, for example the Tobacco Mosaic Virus [1]. **(B)** The minimum enhancement required for the DNP-enhanced thermal polarization to exceed statistical as function of the number of proton spins in the detection volume.

Owing to the small gyromagnetic ratio of protons, Figure 1.1 illustrates that the fractional statistical polarization often exceeds the Boltzmann polarization in nanoscale volumes. As a result, measuring the statistical polarization yields a greater signal-to-noise ratio (SNR) compared to the signal acquired from thermal polarization. Comparatively, the gyromagnetic ratio, and polarization of electrons is much greater, marked by the hyperpolarization line in Figure 1.1. By transferring this larger polarization to protons, DNP can offer a significant boost to the SNR when measuring the mean polarization of the spins [36, 37]. Figure 1.1 shows the minimum enhancement that would be needed in order for a DNP-enhanced thermal polarization (hyperpolarization) to be greater than statistical polarization. The maximum possible enhancement is given by the ratio of the gyromagnetic ratios of electrons and protons, $\gamma_e/\gamma_p \sim 658$. We have also shaded the area in Figure 1.1 that corresponds to where the thermally enhanced polarization exceeds the statistical.

1.4 Dynamic Nuclear Polarization

DNP is a powerful technique in magnetic resonance to improve the detection sensitivity of NMR [36, 37]. In DNP, the larger polarization of unpaired electrons is transferred to surrounding nuclei. In typical samples, the unpaired electrons are in localized states, and only transfer their polarization to nearby, hyperfine-coupled nuclei, after which nuclear dipole-dipole interactions distribute this polarization into the bulk [37–39]. Through repeated applications of this process, the polarization in the overall sample can be built up, where the build-up time is often limited by the spin-lattice relaxation time of the nuclear spins T_{1n}. There exist many methods to achieve the polarization transfer, and in this thesis we focus on transferring the Boltzmann polarization of electrons to nuclei using microwave fields to induce transitions between spin states. If the polarization transfer for an electron-proton system is 100% efficient, the maximum enhancement is $\gamma_e/\gamma_p \sim 658$, where γ_e, γ_p are the gyromagnetic ratios of an electron and proton respectively. In practice, enhancements tend to be smaller than the theoretical limit. However, enhancements of 100 can yield significant improvements in averaging time by a factor of 10^4 [40].

In 1953, Overhauser proposed, that through microwave irradiation of conduction electrons, the electron polarization could be transferred to nearby protons through paramagnetic relaxation processes mediated by hyperfine interactions between the electron-nuclear system [2, 37]. Over the years, many other DNP mechanisms have been proposed and demonstrated for polarization enhancement, with an important one being, nuclear orientation via electron spin locking (NOVEL), which uses microwave pulses to induce transitions between the electron-nuclear spin states by matching the electron Rabi frequency to the

nuclear Larmor frequency, also known as the Hartmann-Hahn matching condition, which we will discuss in greater detail in this section [40, 41]. Other commonly used DNP techniques include the solid and cross effects, both of which have shown large enhancements, on the order of $100 - 200$ in solid state samples. [36, 40, 42–46].

In this this thesis, we will focus on using NOVEL DNP to enhance the polarization of proton spins. In this section, we provide a derivation of the energy matching condition necessary to induce transitions between an electron and a nuclear spin using the NOVEL protocol, where we refer to Reference [47] for an in depth description on the theory of NOVEL.

Consider the Hamiltonian for a two spin system with one electron spin $\mathbf{S}$, and one nuclear spin $\mathbf{I}$

$$H(t) = \underbrace{-\omega_{0S} S_z}_{H_0} \underbrace{-\omega_{0I} I_z - \mathbf{I}\cdot\mathbf{A}\cdot\mathbf{S} - 2\omega_{1s}\cos(\omega_t t) S_x}_{\delta H}, \tag{1.21}$$

where $\omega_{0I} I_z$ is the nuclear Zeeman term, $\omega_{0S} S_z$ is the electron Zeeman term, the electron Rabi drive is $2\omega_{1s}\cos(\omega_t t) S_x$, and $\mathbf{I}\cdot\mathbf{A}\cdot\mathbf{S}$ is the hyperfine interaction between the nuclear and electron spins, where $\mathbf{A}$ is the hyperfine interaction tensor. For convenienve the hyperfine term can be rewritten as

$$\mathbf{I}\cdot\mathbf{A}\cdot\mathbf{S} = \sum_{\alpha,\beta} A_{\alpha\beta} I_\alpha S_\beta = \mathbf{a}\cdot\mathbf{S}, \tag{1.22}$$

where $\mathbf{a} = \sum_{\alpha,\beta} A_{\alpha\beta} I_\alpha \hat{\mathbf{e}}_\beta$ where $\hat{\mathbf{e}}_\beta$ is the unit vector along the $\beta \in \{x, y, z\}$ direction. In Equation 1.21 we assume $\omega_{0S} \gg \omega_{0I}, \omega_{1s}, \|\mathbf{A}\|$ from which it follows $\|H_0\| \gg \|\delta H\|$. We can transform the Hamiltonian to the rotating frame of the electron Larmor term as $\tilde{H}(t) = V(t)^\dagger \delta H V(t)$ with $V(t) = e^{i\omega_{0S} S_z t}$ using a procedure similar to one outlined in Chapter 1.

$$\begin{aligned}\tilde{H}(t) = -\omega_{0I} I_z - \omega_{1S} S_x &- a_x(\cos(\omega_{0S} t) S_x + \sin(\omega_{0S} t) S_y) \\ &- a_y(-\sin(\omega_{0S} t) S_x + \cos(\omega_{0S} t) S_y) \\ &- a_z S_z.\end{aligned} \tag{1.23}$$

The time dependent terms in the Hamiltonian can be neglected since they oscillate on a time scale much faster than the time scale of the nuclear Larmor, or electron Rabi drive. Expanding the $a_z S_z$ term

$$\tilde{H}(t) = -\omega_{0I} I_z - \omega_{1S} S_x - (A_{xz} I_x S_z + A_{yz} I_y S_z + A_{zz} I_z S_z). \tag{1.24}$$

We now transform our coordinate axis such that the y-component of the hyperfine coupling is zero and in our new coordinate axis $A = A_{zz}$ and $B = \sqrt{A_{xz}^2 + A_{yz}^2}$, where A and B are known as the secular, and pseudo-secular hyperfine coupling constants respectively. Thus, the Hamiltonian in the electron rotating frame is

$$\tilde{H} = -\omega_{0I} I_z - \omega_{1S} S_x - B I_x S_z - A I_z S_z. \tag{1.25}$$

The Hamiltonian above was transformed to the electron Larmor frame to simplify the expression for the hyperfine interaction. We now transform the Hamiltonian in Equation 1.21 to the transceiver frame using the operator $V(t) = e^{i\omega_t S_z t}$ and truncating, we have a similar Hamiltonian to equation 1.25

$$\tilde{H} = -\omega_{0I} I_z - \Delta\omega_S S_z - \omega_{1S} S_x - B I_x S_z - A I_z S_z, \tag{1.26}$$

where $\Delta\omega_S = \omega_{0S} - \omega_t$. Using $\mathbf{\Omega}$ to denote the direction of the applied effective magnetic field on the electron, $\mathbf{\Omega} = (\omega_{1S}, 0, \Delta\omega)$, $|\mathbf{\Omega}| = \sqrt{\omega_{1S}^2 + \Delta\omega^2}$. Equation 1.26 can be written as

$$\tilde{H} = -\omega_{0I} I_z - \mathbf{\Omega} \cdot \mathbf{S} - B I_x S_z - A I_z S_z. \tag{1.27}$$

A coordinate transformation to the *tilted frame* is made such that $S_z = -\cos(\theta) S_{x'} + \sin(\theta) S_{z'}$, where $\cos(\theta) = \omega_{1S}/|\mathbf{\Omega}|, \sin(\theta) = \Delta\omega/|\mathbf{\Omega}|$.

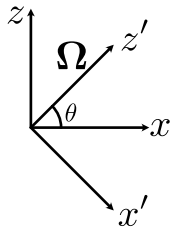


Figure 1.2: **Tilted Rotating Frame Coordinate Axis.**

The Hamiltonian in the tilted frame is then

$$\tilde{H}_T = \underbrace{-\omega_{0I} I_z - |\mathbf{\Omega}| S_{z'}}_{\tilde{H}_0} \underbrace{-(B I_x + A I_z)(-\cos(\theta) S_{x'} + \sin(\theta) S_{z'})}_{\delta\tilde{H}}. \tag{1.28}$$

Rewriting $\delta\tilde{H}$ in terms of spin ladder operators yields

$$\begin{aligned}\delta\tilde{H} = {} & \frac{\cos(\theta)}{4} B (I_+ + I_-)(S_+ + S_-) + \frac{\cos(\theta)}{2} A I_z (S_+ + S_-) \\ & - \frac{\sin(\theta)}{2} B (I_+ + I_-) S_{z'} - A \sin(\theta) I_z S_{z'}\end{aligned} \tag{1.29}$$

If the magnitude of the effective field is greater than the hyperfine couplings we can transform the tilted frame Hamiltonian with $V(t) = e^{i\omega_{0I}tI_z}e^{i|\mathbf{\Omega}|tS_{z'}}$. Considering the special case where $|\mathbf{\Omega}| = \omega_{0I}$ we have

$$\begin{aligned}
\tilde{H}'_T &= U^\dagger(t)\delta\tilde{H}U(t) \\
&= \frac{\cos(\theta)}{4}B\left(e^{-2i\omega_{0I}t}I_+S_+ + I_+S_- + I_-S_+ + e^{2i\omega_{0I}t}I_-S_-\right) \\
&\quad + \frac{\cos(\theta)}{2}AI_z\left(e^{-i\omega_{0I}t}S_+ + e^{i\omega_{0I}t}S_-\right) - \frac{\sin(\theta)}{2}B\left(e^{-i\omega_{0I}t}I_+ + e^{i\omega_{0I}t}I_-\right)S_{z'} \\
&\quad - A\sin(\theta)I_zS_{z'} \\
&= \frac{\cos(\theta)}{4}B\left(I_+S_- + I_-S_+\right) - A\sin(\theta)I_zS_{z'} \qquad (1.30)
\end{aligned}$$

where we have truncated and dropped the terms that pick up a time dependence. The Hamiltonian in the tilted rotating frame becomes

$$\tilde{H}_T = -\omega_{0I}I_z - |\mathbf{\Omega}|S_{z'} + \cos(\theta)\frac{B}{4}\left(I_+S_- + I_-S_+\right) - A\sin(\theta)I_zS_{z'}. \qquad (1.31)$$

Using a similar procedure to the one outlined above, and if instead we define the applied effect magnetic field as $\mathbf{\Omega} = (-\omega_{1S}, 0, \Delta\omega)$, and define our coordinate transformation to the tilted frame as $S_z = \cos(\theta)S_{x'} - \sin(\theta)S_{z'}$ the Hamiltonian takes a modified form which can be written as

$$\tilde{H}_T = -\omega_{0I}I_z - |\mathbf{\Omega}|S_{z'} + \cos(\theta)\frac{B}{4}\left(I_+S_+ + I_-S_-\right) - A\sin(\theta)I_zS_{z'}, \qquad (1.32)$$

From Equations 1.31 and 1.32 we can see that the polarization transfer will be maximized when the effective field points along the applied microwave direction only, $\mathbf{\Omega} = (\pm\omega_{1S}, 0, 0)$. Equation 1.31 and 1.32 can be simplified to

$$\tilde{H}_T = -\omega_{0I}I_z - \omega_{1S}S_{z'} + \frac{B}{4}\left(I_+S_- + I_-S_+\right), \qquad (1.33)$$

$$\tilde{H}_T = -\omega_{0I}I_z - \omega_{1S}S_{z'} + \frac{B}{4}\left(I_+S_+ + I_-S_-\right), \qquad (1.34)$$

Comparing Equations 1.33 and 1.34 to Equation 1.27, we can see that we have changed the form of the pseudo-secular hyperfine term into a flip-flop or flop-flop term that can create transitions between the electron proton spin states. Th condition under which that transition is allowed energetically is when we meet the so called Hartmann-Hahn energy

matching condition, where the Rabi frequency of the electron in the tilted rotating frame is matched with the nuclear Larmor Frequency as shown in Equation 1.35 [41, 46]

$$\omega_{1S} = \pm\omega_{0I}. \tag{1.35}$$

Equation 1.35 is known as the Hartmann-Hahn matching condition, which is necessary to induce transition between electron-proton spin states, where the applied effective field in the tilted rotating frame is the same as the nuclear Larmor frequency [41, 46]. Without the resonance condition there is a large energy penalty for these transitions to occur but if we satisfy the resonance condition then there is no energy penalty and the system is free to undergo these flip flop transitions.

The eigenstates of $\tilde{H}_T$ in Equation 1.33 and 1.34 are

$$\left\{|\uparrow\uparrow\rangle, |\downarrow\downarrow\rangle, |\psi_{\pm}\rangle \propto \left((\omega_{1S} - \omega_{0I}) \pm \sqrt{(\omega_{1S} - \omega_{0I})^2 + B^2}\right)|\uparrow\downarrow\rangle - B\,|\downarrow\uparrow\rangle\right\},$$
$$\left\{|\uparrow\downarrow\rangle, |\downarrow\uparrow\rangle, |\psi_{\pm}\rangle \propto \left((\omega_{1S} + \omega_{0I}) \pm \sqrt{(\omega_{1S} + \omega_{0I})^2 + B^2}\right)|\uparrow\uparrow\rangle - B\,|\downarrow\downarrow\rangle\right\},$$

respectively. The states are written in the product state notation where the electron spin comes first. Applying Equation 1.31 to the $|\uparrow\uparrow\rangle$ or $|\downarrow\downarrow\rangle$ states leaves them invariant, while applying it to $|\uparrow\downarrow\rangle$ or $|\downarrow\uparrow\rangle$ gives the *flip-flop* $|\uparrow\downarrow\rangle \leftrightarrow |\downarrow\uparrow\rangle$ transitions we previously mentioned. Likewise, applying Equation 1.32 to the $|\uparrow\downarrow\rangle$ or $|\downarrow\uparrow\rangle$ states leaves them invariant while applying it to $|\uparrow\uparrow\rangle$ or $|\downarrow\downarrow\rangle$ gives a *flop-flop* $|\uparrow\uparrow\rangle \leftrightarrow |\downarrow\downarrow\rangle$ transtion. These are sometimes referred to as *zero-quantum* (ZQ) and *double-quantum* (DQ) transitions, respectively.

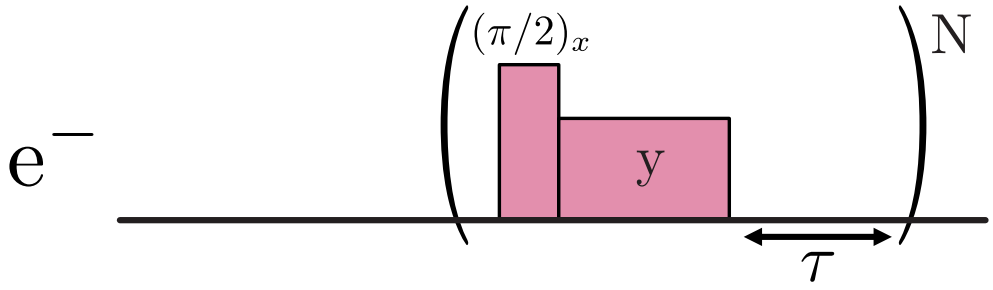


Figure 1.3: **NOVEL DNP Timing Diagram**. The DNP method begins by tipping the electron spins into the transverse plane with a $(\pi/2)_x$ pulse, after which a resonant spin locking drive is applied. The electron polarization is transferred to nearby protons and is allowed to repolarize for a period τ. By applying successive applications of the primitive, for a duration T_b, the proton polarization is built up in a sample.

Figure 1.3 outlines a NOVEL DNP experiment for an electron-proton system. A $\pi/2$ pulse is applied to tip the spins into the transverse plane followed by a spin locking drive is applied for some time to allow for the electrons and protons to undergo a transition mediated by the pseudo-secular hyperfine coupling B. We then wait a time τ, in which spin diffusion carryies the magnetization into the bulk sample. During this time, the electron also repolarizes to thermal equilibrium on a timescale set by the spin-lattice relaxation time of the electrons, T_{1e}. The DNP process is then repeated N times to build the polarization throughout the sample for a time T_b. Note that the maximum buildup time is limited by T_{1p}, which we will discuss in greater detail later on. As a result, the the enhancement achieved will usually saturate before reaching the theoretical maximum enhancement.

It is worth noting that the previously mentioned solid effect DNP mechanism is conceptually similar to the NOVEL protocol discussed above. The difference lies in the fact that rather than matching the Rabi field to the nuclear Larmor frequency, the Hartmann-Hahn matching condition is instead satisfied by modulating the microwave field at $\omega_t = \omega_{0S} \pm \omega_{0I}$ [48]. Consequently, this approach to DNP causes the efficiency of polarization transfer, and the signal enhancements to scale unfavorably with increasing B_0 fields, showing a $1/\omega_{0I}^2$ dependence [40, 48, 49]. As a result, this limits the utility of solid effect DNP to low-field DNP experiments. In contrast, as we have shown above pulsed DNP methods such as NOVEL allow for efficient polarization transfer with no dependence on the static field. The main difficulty of NOVEL DNP is that, as the static field strength increases, the B_1 field strength needed to satisfy Hartmann-Hahn matching condition also becomes larger, which may be technologically challenging. As we discuss later however, the CFFGS devices used in our experiment are capable of generating the necessary B_1 fields, to an extent, when operating at higher static fields. For example, in our current DNP experiment the static field strength is 0.33 T which corresponds to $\omega_{0S} = 9.26$ GHz. We expect that increasing the field $B_0 = 3$ T should be possible considering the main limitation for working at higher fields is currently related to coaxial losses that significantly attenuate the strength of the signals.

1.5 Spin Diffusion

The goal of this section is to provide an overview, and some historical context on the complex dynamics of the spin transport process in DNP. Electron or nuclear spins in a sample are coupled to one another through dipole-dipole interactions. The network of pairwise dipolar interactions between different spins thus forms a dense interconnected system whose dynamics can be difficult to model. However, for a sample in which the

high-temperature approximation holds, and the length scale of variation in magnetization is much larger than the spacing between spins, it has been shown that the dynamics of the coarse-grained magnetization density $M_z(\mathbf{r}, t)$ along the z-direction can be modelled by a classical diffusion equation [50]

$$\frac{\partial M_z(\mathbf{r}, t)}{\partial t} = D\nabla^2 M_z(\mathbf{r}, t), \tag{1.36}$$

where D is the diffusion constant. This evolution of the longitudinal magnetization is often referred to as *spin diffusion*, which for DNP in solid-state materials, is the primary mechanism behind the transport of the enhanced polarization from hyperfine-coupled nuclei to the bulk.

In 1949, Bloembergen proposed that spin diffusion to paramagnetic impurities could account for the reduced nuclear spin-lattice relaxation times that were being observed in crystalline samples [38]. Similarly, as shown in future chapters, spin diffusion to paramagnetic defects is the dominant electron spin-lattice relaxation mechanism in our experiments. Additionally, this same nuclear spin diffusion process also plays a significant role in the DNP process, as we have previously mentioned [39, 51].

Spin diffusion occurs due to energy-conserving *flip-flop* transitions that happen under evolution of the dipolar Hamiltonian [38]. In the presence of a strong external field, the secular dipolar Hamiltonian can be written as

$$H_D = \sum_{i<j} D_{ij} \left(2I_z^i I_z^j - \frac{1}{2}(I_+^i I_-^j + I_-^i I_+^j) \right), \tag{1.37}$$

where $D_{ij} = \mu_0 \hbar \gamma^2 (1 - 3\cos^2\theta_{ij})/(4\pi r_{ij}^3)$ in angular frequency units, θ_{ij} is the angle the static field makes with the line connecting the spin pair, and r_{ij} is the distance between the i and j spins [24]. The $\frac{1}{2}(I_+^i I_-^j + I_-^i I_+^j)$ term in the secular dipolar Hamiltonian represent the flip-flop interaction that can swap the spin states of two nuclei. Specifically, it induces transitions, on a time scale given by the coupling strength, between the $|\uparrow\downarrow\rangle \leftrightarrow |\downarrow\uparrow\rangle$ states, which conserve total Zeeman energy. Thus, the flip-flop interactions facilitate spin diffusion by swapping spin states with neighboring spins, propagating through the sample enabling the spread of polarization throughout. Often, the spin transport process is the rate limiting step in bulk DNP experiments, when attempting to achieve efficient polarization and large enhancements [51] as without efficient spin diffusion the polarization remains localized to the area of the electron center.

For example in the DNP process, large local magnetic field gradients generated by the electron spin can affect the nuclear spin transport in surrounding nuclei. Specifically, large

local magnetic fields gradients generate a resonance shift on nearby nuclear spins that results in the flip-flop interaction being suppressed. To show this, consider a simplified model where we consider a two spin system with that are coupled through dipole-dipole interactions. The Hamiltonian for such a system is $H = -\omega_{01} I_z^1 - \omega_{02} I_z^2 + H_D$. Assuming the Larmor frequencies of the two spins are different from one another, we can transform to the Larmor frame of the second spin and rewrite the Hamiltonian as

$$H = -\Delta\omega I_z^1 + D_{1,2}\left(2I_z^1 I_z^2 - \frac{1}{2}(I_+^1 I_-^2 + I_-^1 I_+^2)\right). \tag{1.38}$$

where $\Delta\omega = \omega_{01} - \omega_{02}$, where ω_{01} and ω_{02} are the respective Larmor frequencies of the two spins. If this resonance offset is large relative to the dipolar frequency, $\Delta\omega \gg D_{1,2}$ we can show that the flip-flop interaction in the dipolar Hamiltonian is suppressed. Transforming to the frame of $H_0 = -\Delta\omega I_z^1$ with unitary $V = e^{-iH_0 t}$

$$\begin{aligned}\tilde{H} &= D_{1,2}\left(2I_z^1 I_z^2 - \frac{1}{2}(e^{-i\Delta\omega t} I_+^1 I_-^2 + e^{i\Delta\omega t} I_-^1 I_+^2)\right) \\ &= D_{1,2}\left(2I_z^1 I_z^2\right),\end{aligned} \tag{1.39}$$

where the fast oscillating time dependent terms have been dropped.

In DNP experiments, one possible source for these resonance shifts comes from large secular hyperfine interactions between the electrons and surrounding nuclear spins, which can shift the nuclear Zeeman energy by more than the proton linewidth. This energy difference results in a suppression of the energy-conserving flip-flop interactions [52]. Consequently, this creates a *spin diffusion barrier* around the electron spin, isolating the nuclear spins contained within the barrier. This results in the polarization being *frozen* at particular sites and inhibits spin diffusion. For modeling the length scale of this barrier, assuming there is no overlap between the wavefunction of the electron and nuclear spins, Blumberg defined the radius of this barrier to be the distance at which the magnetic field due to the electron equals the local dipolar field of nuclei in the bulk sample [52]. Using this definition, the radius of the barrier is approximately given by $(\mu_e/\mu_n)^{1/3}a$, where μ_e and μ_n are the magnetic moments of the electron and nuclear spins, respectively, and a is the spacing between nuclei [52]. The spin diffusion barrier thus initially seems to pose a significant challenge for efficient DNP, as nuclei near an electron center cannot exchange polarization with neighboring spins. However, the spin diffusion process is more complex than this simplified model suggests.

The impact of spin diffusion barriers on DNP was recognized early in its history. Some initial models for explaining the polarization transfer assumed that spin diffusion was not

possible between nuclear spins inside the barrier and the bulk sample. As a result, it was believed that spin diffusion occurred only between spins located outside the barrier, which were weakly coupled to the electron spin [52–54]. Over the years, various estimations for the distance at which spin diffusion becomes effective have been provided by authors such as Khutsishvili, Blumberg, and Goldman [52, 53, 55].

Moreover, even in the presence of large hyperfine interactions, polarization transfer through the spin diffusion barrier has been directly observed [56]. In such cases, the assumption that spin diffusion inside the barrier is completely quenched is false. As noted by Bloembergen, the spin transport process through the spin diffusion barrier no longer conserves Zeeman energy. As a result, the energy must be supplied from another source [38, 51]. Fluctuating fields from the electron spin due to spin-lattice relaxation have been proposed and later verified experimentally as a mechanism to facilitate polarization transfer through the barrier [57–60].

Overall, the role of spin diffusion and diffusion barriers play in the DNP process is difficult to quantify and model precisely due to various influencing mechanisms. Spin diffusion barriers arising from resonance shifts from local magnetic gradient sources play a significant role in the DNP process. On first glance, spin diffusion barriers appear to impede efficient DNP however, many body processes can still enable polarization transfer through the barrier. This subject, though extensively studied, is still not fully understood where there remains no exact model to describe the many body mechanism by which nuclear spin diffusion is facilitated [61].

Chapter 2

Experimental Setup and MAGGIC Protocol

2.1 Magnetic Resonance Force Microscopy

Magnetic resonance force microscopy (MRFM) is used to extend the capabailities of traditional magnetic resonance to nanoscale ensembles, ultimately aiming to achieve such things as atomic spatial resolution, and the ability to image individual molecules. In the experiments presented in this thesis, we combine the increase in detection sensitivity gained from force detected magnetic resonance, with DNP to extend the detection capabilities of magnetic resonance. In this section, we detail experimental setup and some background information on MRFM.

MRFM provides a pathway for enhancing the low detection sensitivity of NMR. There are three primary components that we will discuss that we use in our force detected magnetic resonance experiments. Firstly, an ultrasensitive force sensor with low mechanical dissipation is used to detect the force from nuclear or electron spin samples while in the presence of a strong magnetic field gradient [7]. Secondly, the displacement of the force sensor is measured via optical interferometry. Lastly, a current focusing field gradient source (CFFGS) is used to generate large field gradients required to generate the spin force, as well as for generating radio-frequency (RF) and microwave pulses for spin manipulation. Section 2.1.4 provides an overview of the experimental setup. To detect the magnetization of the spins attached to the tip, we make use of the modulated alternating gradients generated with currents (MAGGIC) protocol which we detail in Section 2.2. As an aside,

some of the discussion, Figures and Tables presented in this chapter can also be found in Reference [24].

2.1.1 Silicon Nanowire Force Sensor

Critical to the high force sensitivities needed to make nanoscale measurements of spins are cantilevers with ultra-low mechanical dissipation. In order to achieve these high force sensitivities, it is critical to reduce the random motion of the cantilever due to thermal fluctuations. In our work, we make use of silicon nanowires (SiNW) as our ultra-sensitive force sensors. SiNWs are characterized by their low mechanical dissipation and, importantly, maintain the low dissipation even when brought as close as 10 nm to a surface [7,18]. The spectral density of thermal force fluctuations for a cantilever with spring constant k, resonance frequency ω_c, and quality factor Q is given as $S_F = 4k_BT\Gamma$, where T is the temperature of the oscillator, k_B is the Boltzmann constant and $\Gamma = k/\omega_c Q$ is the mechanical dissipation, where k is the spring constant. The mechanical properties of SiNWs, such as their natural frequency, dimensions, and spring constant can all be tailored for minimizing the thermal force noise and maximizing displacement sensitivity [18]. In the DNP measurements, we will discuss later the typical force noise was, $S_F^{1/2} \sim 2$ aN$/\sqrt{\text{Hz}}$ at 4 K under vacuum pressures of 10^{-6} Torr [24].

2.1.2 Samples

For the DNP experiments presented in this thesis, we use trityl-OX063 radicals as our polarizing agent. The trityl-OX063 radicals are suspended in a sugar-water matrix attached to the tip of the SiNW. The sugar-water mixture serves as a biologically compatible cryoprotectant that prevents the formation of ice crystals in the sample when cooled to 4 K [24,31,32], which is useful for future experiments involving biomolecules. Additionally, in similar samples of the radicals suspended in glycerol-water, it has been shown that polarization transfer occurs between the electron and hydrogen atoms on the trityl molecules first before the polarization is carried away via spin diffusion to surrounding protons in the glassy matrix [39]. In our experiments, multiple samples were prepared to investigate the dependence of the DNP enhancement on the ratio of electrons and protons in the sample. Figure 2.1 shows the chemical structure of the OX063 along with SEM images of the four samples measured in this work, each attached to different SiNWs.

Trityl OX063 was chosen because of its relatively narrow linewidth and low g-anisotropy owing to the highly symmetric structure of the radical, as well as the fact that it is sur-

rounded by many spinless nuclei [4]. Narrow linewidths are important when doing DNP with the NOVEL protocol, as the effectiveness of the resonant spin locking drive depends on most of the electrons being near the Larmor frequency. Thus, smaller linewidths mean more electron spins will participate in the state transfer process, increasing the performance of the polarizing agent [4]. In addition, the secular hyperfine coupling is also relatively small compared to the pseudo-secular hyperfine which is $B/(2\pi) \sim 1$ MHz [62]. As we will show later. larger pseudo-secular hyperfine also help in ensuring efficient polarization transfer. As mentioned in Section 1.5, large secular hyperfine couplings act as spin diffusion barriers, that would limit the ability for the polarization to spread through the sample [39, 51], and are hence undesirable.

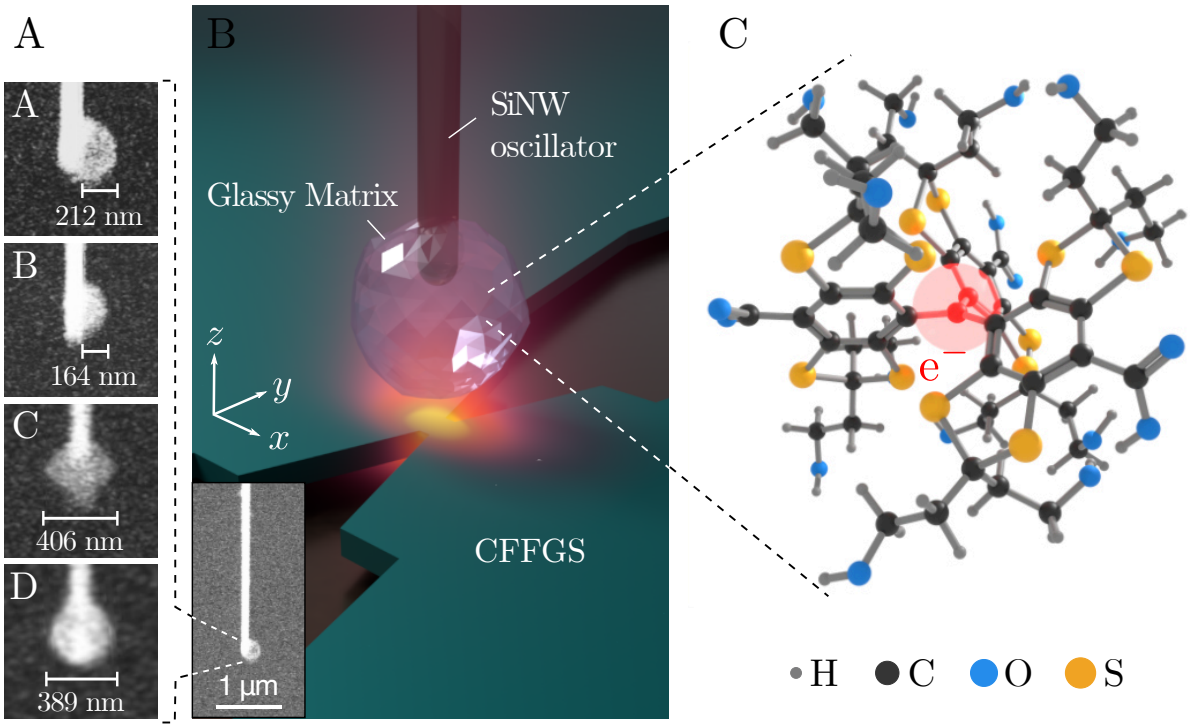


Figure 2.1: **Trityl OX063 Polarizing Agent**. **(A)** SEM images taken of the nanodroplets attached to the tip of the SiNW showing the different morphologies of the samples. **(B)** Schematic of the SiNW positioned over the CFFGS device and the trityl-OX063 radical suspended in the glassy matrix. **(C)** Chemical structure of the trityl-OX063 radical. Due the symmetric structure of the radical, the electron spin exhibits low g-anisotropy and narrow linewidths [4].

Table 2.1 provides a complete summary of the molecules used for the sample preparation. For details of the sample attachment process, refer to the supplements of Reference [24]. Unless otherwise stated, the majority of data presented will be for Sample A, where the largest enhancements were observed in the DNP process.

Table 2.1: **Constituent table,** including all the components used to prepare the measured samples.

Constituents	**A**	**B**	**C**	**D**
Sucrose (mg); $C_{12}H_{22}O_{11}$	-	-	-	80.7
Glucose (mg); $C_6H_{12}O_6$	6.0	6.1	6.1	-
d-12 Glucose (mg); $C_6D_{12}O_6$	54.0	54.4	54.4	-
H_2O (µL)	15	15	15	100
D_2O (µL)	135	135	135	-
Ethanol (µL)	-	-	-	50
d-Ethanol (µL)	150	150	150	-
OX063 (mg)	0.92	2.58	2.58	2.10
Concentration (mM)	17.8	49.4	49.4	29

2.1.3 Current-Focusing Field Gradient Source

The force the spins exert on the SiNW is proportional to the gradient of the magnetic field they experience, i.e. $\mathbf{F}(t) = \boldsymbol{\nabla}(\boldsymbol{\mu}(t) \cdot \mathbf{B}(\mathbf{r}, t))$, where $\mu(t)$ is the magnetic moment, and $\boldsymbol{\nabla}\mathbf{B}(\mathbf{r}, t)$ is the gradient at position $\mathbf{r}$. For generating the large gradients needed for spin detection as well as for generating radio-frequency (RF) and microwave pulses used for proton and electron spin control, a current is passed through a narrow metallic constriction, which we refer to as the current-focusing field gradient source (CFFGS) [7, 13, 14]. The CFFGS consists of an Aluminum (Al) thin film deposited on a sapphire substrate, patterned via e-beam lithography, with a minimum feature size of $\sim$ 150 nm [13, 14]. By focusing the currents passing through the film into this small region, large non-uniform magnetic field gradients are generated. The gradients generated by such devices can be as large as 10 G/nm [13]. Figure 2.2 shows SEM images of the design as well as an optical image of the overall device design [24].

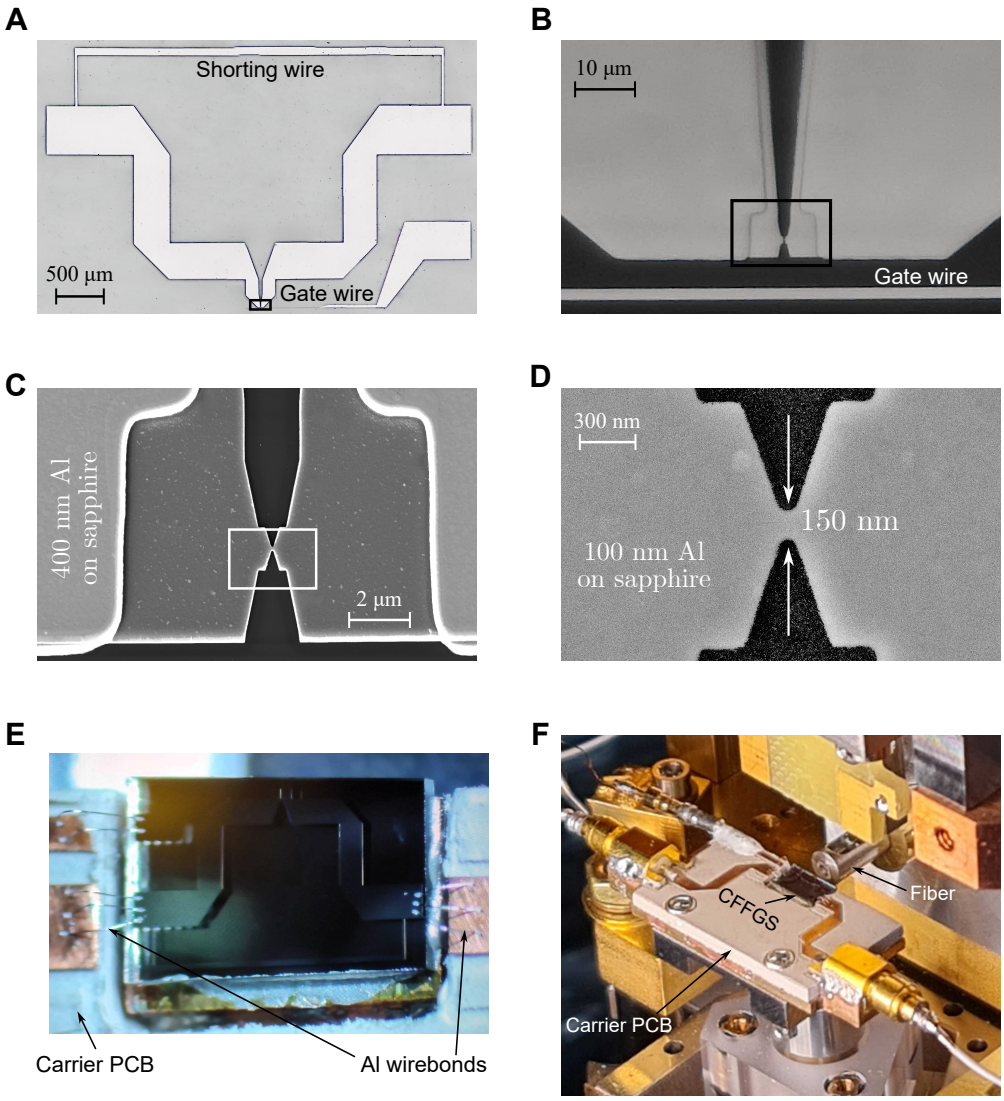


Figure 2.2: **Optical Images of CFFGS**. **(A)** Optical image of CFFGS composited from multiple snapshots of different regions. **(B)** Optical image of the central head section of the CFFGS, along with a gate wire that can be used to apply an electrostatic potential to the CFFGS. **(C, D)** SEMs of the CFFGS device with a minimum feature size of 150 nm. **(E)** Electrical connections are made to the CFFGS device with Al wirebonds connecting the device to a 50 Ω microstrip line on a carrier PCB. **(F)** Coaxial connections to the PCB are made with mini-SMP connectors.

The CFFGS devices used in our experiments were also designed to support the transmission of signals for a wide range of frequencies ($\sim$ DC $-$ 10 GHz) to manipulate proton and electron spins. Electronic connections to the CFFGS device are made through 25 μm diameter Al wirebonds, connecting it to a 50 Ω microstrip line. As mentioned previously, an important aspect of the current CFFGS devices is that the magnetic fields and gradients generated are non-uniform which results in a spatially varying B_1 field. The B_1 dispersion means that constant amplitude pulses can not be used for global control of spins rather, it necessitates the use of engineered pulses that can address a wide bandwidth of Rabi frequencies in order to effectively manipulate the majority of spins. In our experiment, we make use of numerically engineered adiabatic pulses as well as global unitaries implemented using optimal control theory for spin manipulation [63–65]. Using COMSOL finite element software, the Rabi fields $B_1(\mathbf{r}) = \sqrt{B_x^2(\mathbf{r}) + B_y^2(\mathbf{r})}/2$, and detection gradient $G_c(\mathbf{r}) = \partial B_z/\partial y$ generated by the CFFGS are presented in Figure 2.3. In our experiment, the peak current when generating the B_1 fields was 29 mA, and 47 mA for the detection gradients.

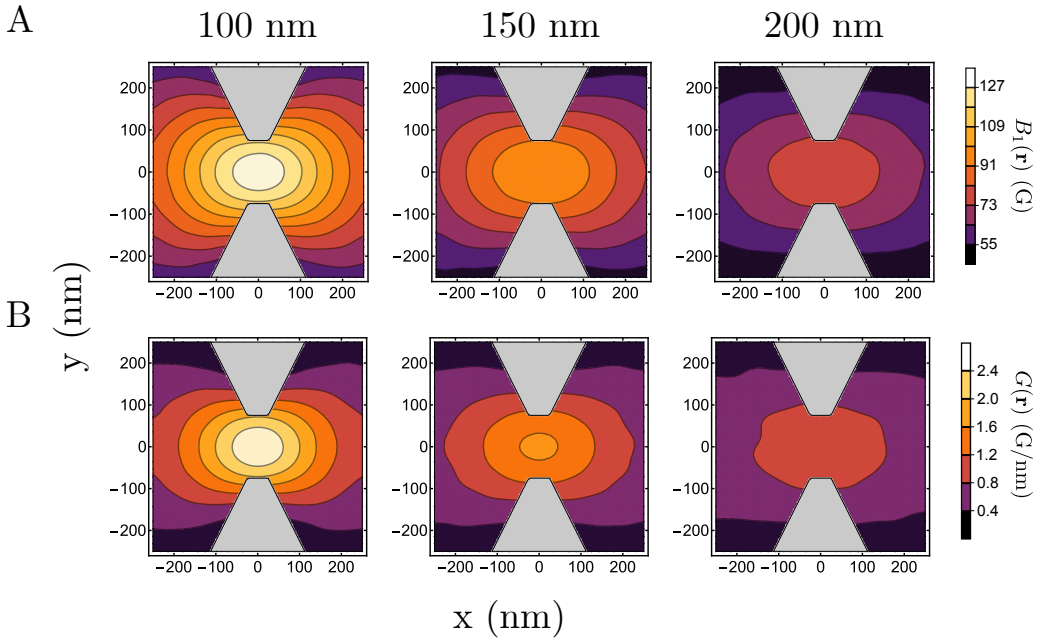


Figure 2.3: **CFFGS Field Profiles**. **(A)** Simulated Rabi field contours at 100, 200, and 300 nm distances above the center of the constriction with $I_{pk} = 29$ mA. **(B)** Simulated detection gradients at different heights from the center of the CFFGS with $I_{pk} = 47$ mA.

2.1.4 Experimental Setup

Figure 2.4 provides an overview of the force-detected magnetic resonance setup used in our DNP experiments. The details of the experimental setup are also presented in Reference [24]. Experiments are conducted in a cryogenic dewar at 4.2 K and high vacuum (10^{-6} Torr). The dewar is equipped with a superconducting magnet capable of generating large uniform static fields of up to 6 T. To align the CFFGS and SiNW with nanometer scale precision, we use three-axis Attocube positioners and scanners.

In order to maximize the force generated by the spins, large magnetic field gradients are required. To maximize the magnetic field gradients the sample is brought to within 100 nm of the CFFGS. As the sample-surface separation decreases, non-contact friction arising from fluctuating electric fields from the surface can significantly impact the performance of the SiNW oscillator and cause frequency jitter [7, 66, 67]. To mitigate this and improve the frequency stability of the oscillator, we employ feedback cooling which increases the detection bandwidth, thus reducing the response time of the oscillator [68, 69]. In our experiments, the intrinsic quality factor of the SiNW at 4 K was $Q \sim 30,000$, and after feedback cooling the damped quality factor was $Q_c = 900$. For employing the feedback cooling, we make use of a piezoelectric transducer attached to the SiNW chip for applying the feedback control signals. For vibrational isolation, the chips are then mounted to a 5 μm thin foil attached to a PCB as shown in Figure 2.4.

For interferometric detection, a diode laser operating at $\lambda = 1510\,\text{nm}$ is used to detect the SiNW displacement [24]. The light directed from the 5% output branch of the 95:5 fiber coupler is focused to a 1.5 µm spot size on the SiNW through a microlens assembly connected to a piezo scanner [24]. The displacement of the SiNW was then measured by interfering light reflected from the cleaved face of the fiber, with back-scatted light from the surface of SiNW with PD1 being used to detect the intensity of the interfered light. The generated photocurrent is converted to a voltage using a transimpedance amplifier. The voltage signal is then demodulated using a lock-in amplifier referenced to the frequency of the SiNW [14].

The light exiting the 95% branch of the fiber coupler is sent to PD2 which is used to monitor the output power of the laser diode. The field-programmable gate array (FPGA) shown in the Figure is responsible for processing the output of the lock-in amplifier as well as sending timing triggers to the arbitrary waveform generators (AWG) and switches which are used for generating pulses for the CFFGS. The electronics are discussed in greater detail in Section 2.4.

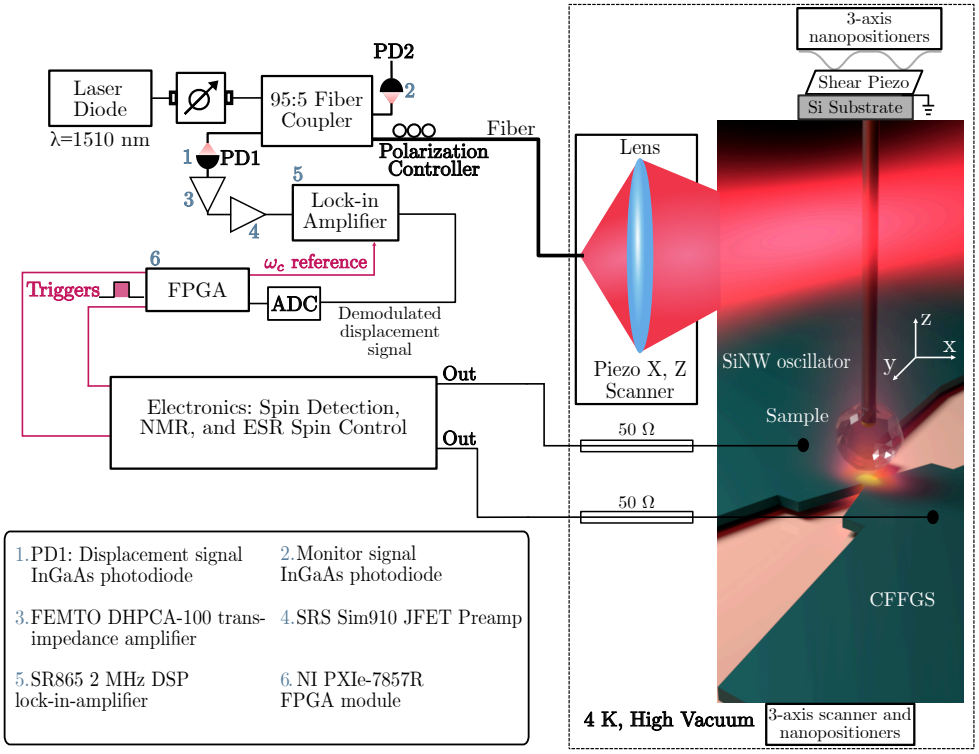


Figure 2.4: **Schematic of the Experimental Setup**

2.2 Spin Detection Protocol

In this section we briefly outline the spin detection protocol used for measuring the magnetization in our MRFM setup based on previous works [13,14]. As mentioned previously, the force a magnetic field gradients generates on a spin at position $\mathbf{r}$ is $\mathbf{F}(t) = \boldsymbol{\nabla}(\boldsymbol{\mu}(t)\cdot\mathbf{B}(\mathbf{r},t))$. For a spin aligned with the z-axis the force is $\mathbf{F}(t) = \mu_z(t)\nabla B_z(\mathbf{r},t)$. Measurement timescales are usually much greater than spin-spin relaxation time, T_2, meaning the transverse components of the magnetization decay and spins are always aligned with the z-axis. We detect the displacement of the SiNW along the y direction as shown above in Figure 2.4, thus the force component of interest is $F_y(t) = \mu_z(t)\partial B_z(\mathbf{r},t)/\partial y$. By engineering the time dependence of μ_z and the field gradient, we can generate a spin force that is on resonance with the SiNW oscillator and results in a displacement that can be measured via optical interferometry.

The simplest method to detect the spin signal is to modulate the magnetic field gradient $\partial B_z(\mathbf{r},t)/\partial y$ at the cantilever frequency ω_c by running a time dependent current through the CFFGS where $\partial B_z(\mathbf{r},t)/\partial y = G_c(\mathbf{r})\cos(\omega_c t)$, with $G_c(\mathbf{r})$ being the peak gradient at position $\mathbf{r}$. The drawback is that the time dependent current also generates an electric field at ω_c, which can couple to stray charges on the SiNW, resulting in a spurious force that masks the spin signal.

To mitigate this, we periodically alternate the phase of the gradient modulation, with a π phase shift between adjacent periods of the gradient modulation, while simultaneously inverting the spin magnetization using adiabatic fast passages (AFPs) (Figure 2.5). This protocol moves the spectral content of current and hence the electric field to sidebands that are at a frequency $2\pi/\tau$ away from resonance, where τ is the time between phase flips as shown in Figure 2.5. Meanwhile, the magnetic force on the spins as shown in Figure 2.5 retains a large spectral component at ω_c with an RMS value of $\mu DG(\mathbf{r})/\sqrt{2}$ where $D = \tau_1/(\tau_1+\tau_2)$ is the duty cycle of the gradient modulation, and $G(\mathbf{r})$ is the peak value of the readout gradient $\partial B_z(\mathbf{r},t)/\partial y$.

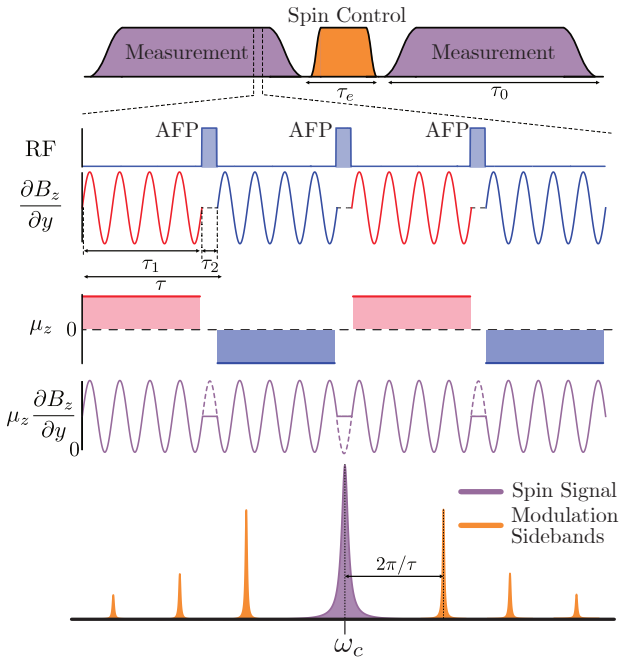


Figure 2.5: **MAGGIC Measurement Protocol**. (**A**) Magnetic Resonance experiments are usually made up of successive blocks of some spin control sequence in which we encode some information of interest and are followed by measurement blocks which employ the MAGGIC protocol to detect the z-axis magnetization of the spin ensemble. (**B**) MAGGIC waveform primitive. (**C**) Spectrum of a spin signal and modulation sidebands generated by the CFFGS.

Above, we have assumed a single spin with infinite spin lattice relaxation time and perfect AFP inversions. Generally, for a spin distribution with spin density $n(\mathbf{r})$ the total force on the SiNW will be the sum of the individual forces on the spins. Thus, the rms force is

$$F(t) = \frac{\mu D}{\sqrt{2}} \int d^3r \; n(\mathbf{r}) G(\mathbf{r}) h(\mathbf{r}, t), \tag{2.1}$$

where $h(\mathbf{r}, t) \in \{-1, 1\}$ is a stochastic telegraph process that is used to model random spin flips that occur due to spin-lattice relaxation, and imperfect AFP inversions during the MAGGIC protocol [13, 24]. The number of sign flips of $h(\mathbf{r}, t)$ in any given interval is Poisson-distributed with an autocorrelation function $\langle h(\mathbf{r}, t_1), h(\mathbf{r}, t_2) \rangle = e^{-|t_2 - t_1|/\tau_m}$, where τ_m is the spin correlation time [7, 13, 14, 24]. The spin correlation time is a T_1 like process that encompasses the effect of both the pulse infidelity of the AFP and the spin-lattice

relaxation time T_1. To quantify the fidelity of the AFPs in the MAGGIC protocol as a function of Rabi frequency u, the AFP fidelities are characterized with a parameter $\alpha(u)$ as follows

$$\begin{aligned}\alpha(u) &= \left|\langle\uparrow| U_{\text{AFP}}^{\dagger}(u)\sigma_z U_{\text{AFP}}(u) |\uparrow\rangle\right| \\ &= \left|\langle\uparrow| U_{\text{AFP}}^{\dagger}(u) \left(\mathbb{1} - 2 |\downarrow\rangle \langle\downarrow|\right) U_{\text{AFP}}(u) |\uparrow\rangle\right| \\ &= \left|1 - 2 \left|\langle\downarrow| U_{\text{AFP}}(u) |\uparrow\rangle\right|^2\right|, \end{aligned} \tag{2.2}$$

where $U_{\text{AFP}}(u)$ is the AFP propagator at Rabi frequency u [14].

An MRFM experiment, as shown in Figure 2.5(A) consists of repeated cycles of a spin control and measurement block. During the spin control block, different spin control techniques of interest may be implemented, such as the NOVEL protocol to hyperpolarize proton spins, or encoding spatial information for an imaging experiment. This is then followed by the measurement block, in which the MAGGIC protocol is applied to generate a resonant force on the SiNW that can be detected. A measurement block has a duration τ_0, which, when measuring the mean magnetization, is usually on the order of two or three times τ_m. During a measurement sequence the signal will decay to zero with time constant τ_m as shown in Figure 2.6. A MAGGIC primitive waveform consists of a gradient modulation pulse with duration τ_1 followed by an AFP pulse, with the total duration of the MAGGIC primitive being τ. By considering N repeated applications of a MAGGIC primitive in a measurement block, with an inversion pulse fidelity α, and a T_1 decay in the magnetization during each MAGGIC primitive, we can derive an explicit expression for the spin correlation time τ_m during a measurement block as

$$\begin{aligned} e^{-\frac{Nt}{\tau_m}} &= \alpha^N e^{-\frac{Nt}{T_1}} \\ \frac{t}{\tau_m} &= \frac{t}{T_1} - \ln\alpha \\ \tau_m &= \frac{\tau T_1}{\tau - T_1 \ln\,\alpha}, \end{aligned} \tag{2.3}$$

where τ is the length of a MAGGIC primitive as shown in Figure 2.5. If the pulse fidelity is $\alpha = 1$ then τ_m becomes T_1 exactly. It is important to note that the magnetization after a measurement is close to zero due to the application of the AFPs. As a result, when measuring a mean magnetization we must wait a time on the order of the spin-lattice relaxation time T_1 to allow the spins to repolarize. In the case where we measure statistical polarization however, we do not need to wait for the spins to repolarize since we are measuring the statistical fluctuations in the number of spins pointing up and down.

This removes the constant overhead in measurement time that exists when measuring the mean polarization and improves the SNR for a given experiment time under which the data is averaged over. In the next section we discuss in more detail how mean and statistical polarization signals are measured.

2.3 Mean and Statistical Polarization Measurements

2.3.1 Thermal Polarization Measurements

In this section, we detail how measurements of the thermal or mean polarization are made. The mean z-magnetization at the start of the measurement block is denoted by $m_0 = \mathbb{E}[h(\mathbf{r}, 0)]$ where the associated probability distribution for the initial population is $\mathbb{P}[h(\mathbf{r}, 0) = \pm 1] = (1 \pm m_0)/2$. As mentioned previously, the distribution of spin flips is Poisson distributed from which we can derive an expression for $\mathbb{E}[h(\mathbf{r}, t)]$ shown in Appendix A, yielding

$$\mathbb{E}[h(\mathbf{r}, t)] = m_0(\mathbf{r}) e^{-t/\tau_m}. \tag{2.4}$$

In an experiment, when measuring the thermal polarization of the sample, we measure the sample average of the force signal from Equation 2.1 over M realizations, $\mathcal{F}(t) = \sum_{i=1}^{M} F_i(t)/M$ where i is the index for a particular realization of the signal. It is important to note that when measuring thermal ensembles we must wait a time on the order of T_1 for the spin system to repolarize such that we are measuring independent realizations of the force signal. From Equation 2.1 and Equation 2.4, we can derive an expression for the expectation value of the force signal

$$\langle F(t) \rangle = \frac{\mu D}{\sqrt{2}} \int d^3r \; n(\mathbf{r}) G(\mathbf{r}) \langle h(\mathbf{r}, t) \rangle \tag{2.5}$$

$$= \frac{\mu D}{\sqrt{2}} e^{-t/\tau_m} \int d^3r \; n(\mathbf{r}) G(\mathbf{r}) m_0(\mathbf{r}) \tag{2.6}$$

This force expression can be translated to a displacement signal by taking the convolution of the time-domain force signal with the impulse response of a simple harmonic oscillator. The mean displacement of the SiNW is then

$$\langle Y(t) \rangle = \frac{\mu D Q_c}{\sqrt{2} k} \frac{e^{-t/\tau_m} - e^{-t/\tau_Q}}{1 - \tau_Q/\tau_m} \int d^3r \; n(\mathbf{r}) G(\mathbf{r}) m_0(\mathbf{r}), \tag{2.7}$$

where we have assumed $Q_c \gg 1$. Q_c is the damped quality factor of the oscillator, $Q_c \sim 900$, k is the spring constant, and $\tau_Q = 2Q_c/\omega_c \sim 1$ ms, is the characteristic response time of the oscillator. In the limit where $\tau_m, t \gg \tau_Q$, we have the measured displacement signal is proportional to the force ignoring the fast rise in the initial part of the signal due to the limited bandwidth of the SiNW, $\langle Y(t)\rangle \simeq (Q_c/k)\langle F(t)\rangle$. Equation 2.7 is used for modelling the fits to the time records presented in this work. Figure 2.6 provides an example time record of the average force signal when measuring the thermal polarization of proton spins. The figure illustrates the initial rise in the force signal due to the finite bandwidth of the oscillator and the decay in magnetization to zero with time constant τ_m.

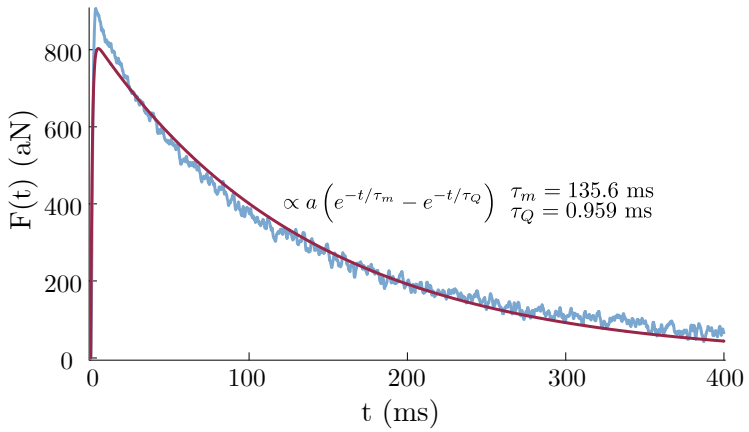


Figure 2.6: **Average Force time Record.** Average force time record (blue) and fitted data (red) of hyperpolarized proton spins. To increase the response time of the oscillator, the SiNW was damped to a quality factor of 900.

The acquired time records for processing the force signal can be processed using different schemes where we want to map the force time record to a single number. One method of achieving this is to take the mean of the time domain signal. However, for optimal SNR, a matched filtering scheme is employed [70]. The goal here is to find a kernel function $w(t)$ for which the inner product $\bar{F} = \langle w(t)|F(t)\rangle = \int_0^{\tau_0} dt\; w(t)F(t)$ maximizes the SNR SNR $= \langle\bar{F}\rangle/\sqrt{\mathrm{Var}(\bar{F})} \propto \langle w(t)|F(t)\rangle\,/\|w(t)\|$. Therefore, the kernel function that maximizes the SNR is proportional to $F(t)$ by the Cauchy-Schwartz inequality [24]. Also, by normalizing $w(t)$ such that $\int_0^{\tau_0} dt\; w(t) = 1$, we can interpret $\bar{F}$ as a weighted average of $F(t)$ where the larger amplitudes at the beginning of the time record are weighted more than points at the end of the decay. In our experiments, we fit a function of the form of Equation 2.7 to a measured hyperpolarized thermal signal (when measuring proton signal) and use it for

the kernel function $w(t)$. In the above analysis, it is assumed that noise in the measured thermal signal is approximately white. The matched filter kernel is then used to process subsequent data. Since $\tau_0, \tau_m \gg \tau_Q$ the initial rise time in the signal from Equation 2.7 can be ignored and we take $w(t) \propto e^{-t/\tau_m}$. Combining this with Equation 2.6 the form of $\bar{F}$ becomes

$$\langle \bar{F} \rangle = \frac{\mu D}{2\sqrt{2}}(1 + e^{-\tau_0/\tau_m}) \int d^3r \; n(\mathbf{r})G(\mathbf{r})m_0(\mathbf{r}). \tag{2.8}$$

2.3.2 Statistical Polarization Measurements

When measuring the statistical polarization using MAGGIC, the mean polarization is zero. Thus, one way to measure the statistical fluctuations of the signal is by measuring the displacement spectral density of the SiNW signal. Importantly, we can use this to find the RMS force, as well as the time scale of spin correlations, τ_m. In Figure 2.7 we show the single-sided displacement spectral density taken during a statistical measurement. The displacement spectral density was calculated by first acquiring 5 s long time records of the spin signal from which we compute a FFT signal to generate the frequency domain spectra. We then take the magnitude squared of the signal and average over 453 different realizations to produce the displacement spectral density. The figure shows the spin signal superimposed on the SiNW response which has been damped to $Q_c = 900$.

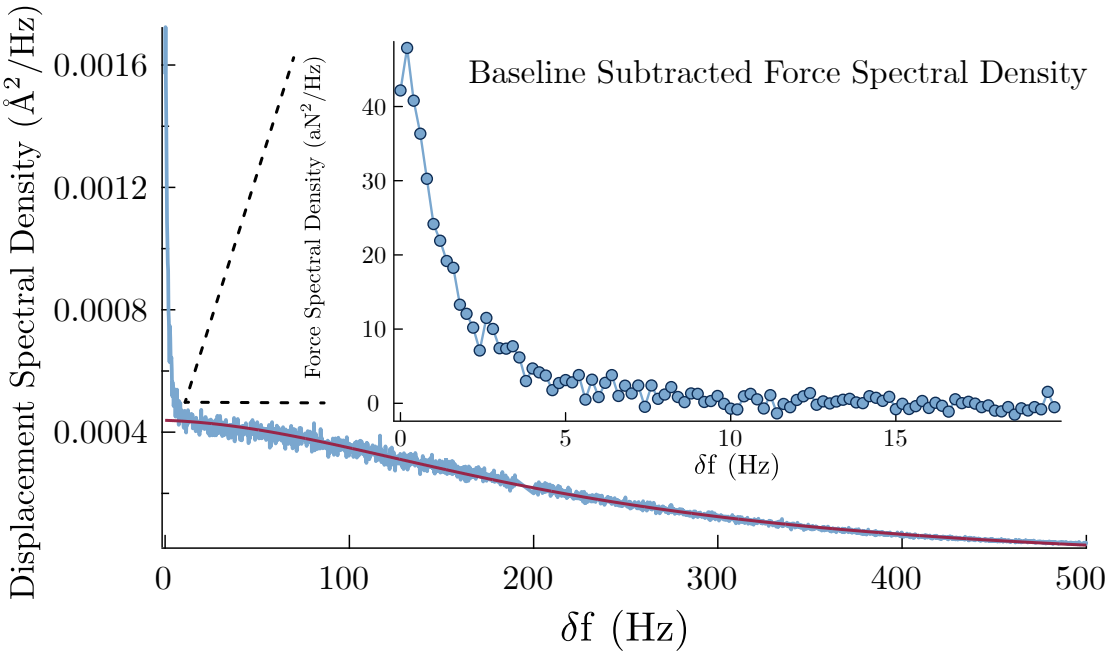


Figure 2.7: **Average Single Sided Displacement Spectral Density of Proton Spin signal.** The average single-sided displacement spectral density of the proton signal superimposed on the damped SiNW response. (Inset) The fitted baseline response of the SiNW has been subtracted and converted to force units to show the force spectral density of the signal. Both spectra are shown as a function of offset frequency δf from the carrier frequency, which is referenced to the mechanical resonance of the SiNW.

For spectroscopic or imaging purposes however, in order to measure encoded information in the spin states, measuring the displacement or force spectral densities is not sufficient. Instead, we measure correlations between measure blocks placed before and after a spin encoding sequence. As a result, this can provide information on the effect the encoding pulse sequences have on the statistical fluctuations [71]. For measuring the statistical polarization, we compute an average correlation function between adjacent measurement blocks where the length of the measurement blocks τ_0 is chosen to be much shorter than the spin correlation time τ_m. The correlation function for the time-averaged force signal between adjacent measure blocks is constructed as

$$C = \frac{1}{M-1}\sum_{i=1}^{M-1} \bar{F}_i \bar{F}_{i+1}, \tag{2.9}$$

where $\bar{F}_i$ is the time average of the force signal for the i^{th} measure block with a uniform weighting [7, 13, 14, 71]. In contrast to measurements of the average polarization which require a wait time to repolarize the spins, measurements of statistical polarization can be done with no overhead. The spin signal obtained for average correlation is outlined below with a timing diagram given in Figure 2.8 [13, 14, 24]

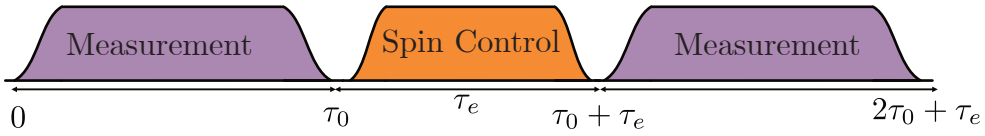


Figure 2.8: **Timing diagram for Statistical Polarization measurements**

The average correlation $\langle C \rangle$ is

$$\langle C \rangle = \frac{1}{M-1} \sum_{i=1}^{M-1} \frac{1}{{\tau_0}^2} \int_{(i-1)(\tau_0+\tau_e)}^{(i-1)(\tau_0+\tau_e)+\tau_0} dt_1 \int_{(i)(\tau_0+\tau_e)}^{(i)(\tau_0+\tau_e)+\tau_0} dt_2 \, \mathbb{E}[\bar{F}(t_1)\bar{F}(t_2)], \tag{2.10}$$

where $\mathbb{E}[\bar{F}(t_1)\bar{F}(t_2)]$ is,

$$\mathbb{E}[\bar{F}(t_1)\bar{F}(t_2)] = \frac{\mu^2 D^2}{2} \sum_{\mathbf{r},\ \mathbf{r}'} G(\mathbf{r}) G(\mathbf{r}') \mathbb{E}[h(\mathbf{r}, t_1), h(\mathbf{r}', t_2)]. \tag{2.11}$$

We assume the random spin flips at position $\mathbf{r}, \mathbf{r}'$ are not correlated with each other and that the encoding time is much smaller than τ_m and T_1, then [71]

$$\begin{aligned} \mathbb{E}[\bar{F}(t_1)\bar{F}(t_2)] &= \frac{\mu^2 D^2}{2} \sum_{\mathbf{r},\ \mathbf{r}'} G(\mathbf{r}) G(\mathbf{r}') \underbrace{\mathbb{E}[h(\mathbf{r}, t_1), h(\mathbf{r}', t_2)]}_{\delta_{\mathbf{r},\mathbf{r}'} \xi(\mathbf{r}) e^{-|t_2 - t_1|/\tau_m}} \\ &= \frac{\mu^2 D^2}{2} \sum_{\mathbf{r}} G^2(\mathbf{r}) e^{-(t_2 - t_1)/\tau_m}, \qquad (t_2 > t_1 \text{ in integration domain}) \end{aligned} \tag{2.12}$$

Equation 2.10 then becomes

$$\langle C\rangle = \frac{1}{M-1}\sum_{i=1}^{M-1}\frac{1}{{\tau_0}^2}\frac{\mu^2D^2}{2}\sum_{\mathbf{r}}G^2(\mathbf{r})\xi(\mathbf{r})\int_{(i-1)(\tau_0+\tau_e)}^{(i-1)(\tau_0+\tau_e)+\tau_0}dt_1\int_{(i)(\tau_0+\tau_e)+\tau_0}^{(i)(\tau_0+\tau_e)+\tau_0}dt_2\ e^{-(t_2-t_1)/\tau_m} \tag{2.13}$$

$$= \frac{1}{{\tau_0}^2}\frac{\mu^2D^2}{2}\sum_{\mathbf{r}}G^2(\mathbf{r})\xi(\mathbf{r})\frac{1}{M-1}\sum_{i=1}^{M-1}\tau_m^2\ e^{-i(\tau_0+\tau_e)/\tau_m}(1-e^{-\tau_0/\tau_m})e^{-(i-1)(\tau_0+\tau_e)/\tau_m}\times e^{(i-1)(\tau_0+\tau_e)/\tau_m}(e^{\tau_0/\tau_m}-1) \tag{2.14}$$

$$= \frac{\mu^2D^2}{2}\left(\frac{\tau_m}{\tau_0}\right)^2(1-e^{-\tau_0/\tau_m})^2\sum_{\mathbf{r}}G^2(\mathbf{r})\xi(\mathbf{r})\frac{1}{M-1}\sum_{i=1}^{M-1}e^{-\tau_e/\tau_m}(1-e^{-\tau_0/\tau_m})^2 \tag{2.15}$$

$$= \frac{\mu^2D^2}{2}\left(\frac{\tau_m}{\tau_0}\right)^2(1-e^{-\tau_0/\tau_m})^2\sum_{\mathbf{r}}G^2(\mathbf{r})\xi(\mathbf{r}), \tag{2.16}$$

In the continuum limit $\langle C\rangle$ becomes

$$\langle C\rangle = \frac{\mu^2D^2}{2}\left(\frac{\tau_m}{\tau_0}\right)^2(1-e^{-\tau_0/\tau_m})^2\int d^3r\ n(\mathbf{r})G^2(\mathbf{r})\xi(\mathbf{r}), \tag{2.17}$$

where $\xi(\mathbf{r} = \mathrm{Tr}[\sigma_z\rho_f(\mathbf{r})]$ is proportional to the expectation value of the z magnetization and $\rho_f(\mathbf{r})$ is the reduced density matrix of a spin at position $\mathbf{r}$, due to the evolution of the spin during the spin control sequence, where the spin starts from an initial state $|\uparrow\rangle$ [13, 14, 24]. Comparing Equation 2.17 and Equation 2.8 reveals that the correlation signal is proportional to the $G^2(\mathbf{r})$ instead of $G(\mathbf{r})$. This has the effect of narrowing the detection volume of the spins and weighting the signal from spins that are closer to the CFFGS more than the spins that are further away.

As mentioned previously, when working with small ensembles measuring statistical polarization has two main advantages over measuring thermal polarization. Firstly, since the realizations between adjacent measure blocks do not need to be independent, there is no requirement to wait for the spins to repolarize in between measurement blocks. For a fixed experiment time, and assuming the spin control blocks are short compared to the measurement time τ_0, a higher percentage of the experiment time can be spent acquiring the signal and averaging, increasing the SNR of the signal. In addition, the statistical polarization is larger than the thermal polarization for small ensembles, as shown in Figure 1.1, therefore yielding a larger signal. We will show later, however, that with DNP, for a given experiment time, the thermal signal can be enhanced sufficiently to provide an SNR advantage over measuring statistical polarization.

2.4 Electronics

In this section, we provide an overview of the electronics needed to generate pulses used for spin control and detecting electrons and protons in our system. Importantly, the electronics needed for ESR control had not been previously developed, and this is a new addition to the experimental setup. As a result, this section explores the use of different components in the circuit. The electronics can be divided into three primary sections that operate in different frequency bands: 1) low frequency (LF) (0 - 2 MHz) used for generating the gradient modulation waveforms used in the MAGGIC Protocol, 2) RF (2 - 50 MHz) responsible for proton spin manipulation, and 3) ESR (9 - 9.4 GHz)) responsible for generating microwave pulses used for controlling the trityl-OX063 radical. Proton and electron spin manipulation require pulses that can be generated near their respective Larmor frequencies, $\omega_{0I}/2\pi = 14$ MHz, and $\omega_{0S}/2\pi = 9.26$ GHz. Figure 2.9 provides a schematic for generating the RF and microwave pulses for proton and electron spin manipulation, with their respective frequency bands of operation highlighted as well.

The schematic shows that the RF and low frequency signals are combined using a passive filter network, *bias-Tee*. The electron spin control signals are then added to the combined RF and low frequency signals using a diplexer. The diplexer is a three port device that uses different frequency band filters to combine the signals. The utilized diplexer has a low pass port, DC - 2 GHz, and a high pass port, 4 GHz - 20 GHz, the output of which directly connects to the CFFGS device.

In total, two arbitrary waveform generators (AWGs) are used to generate the ESR, NMR and spin detection pulses used in our experiments. As shown in Figure 2.9, AWG2 is responsible for generating the gradient modulation waveforms. The gradient modulation pulses are driven differentially to ensure that at the center of the CFFGS device, there is an electric field node, thereby minimizing any electrical interactions that may occur with charges on the SiNW. A consideration when choosing the AWG for this task is the output noise of the AWG. Output noise from the amplifier during the gradient modulation will contribute to detection noise. As a result, we seek to minimize any noise sources that will be present in the gradient modulation pulse. The output noise of the NI AWG is reported as -145 dBm/Hz. As shown in the previous section, where we discussed the MAGGIC protocol, the measured signal was proportional to the applied magnetic field gradient, which is proportional to the applied current through the CFFGS. In this experiment, the gradient modulation pulses are driven with a $I_{pk} = 49$ mA. To achieve this, we use a low-noise amplifier to provide the necessary gain.

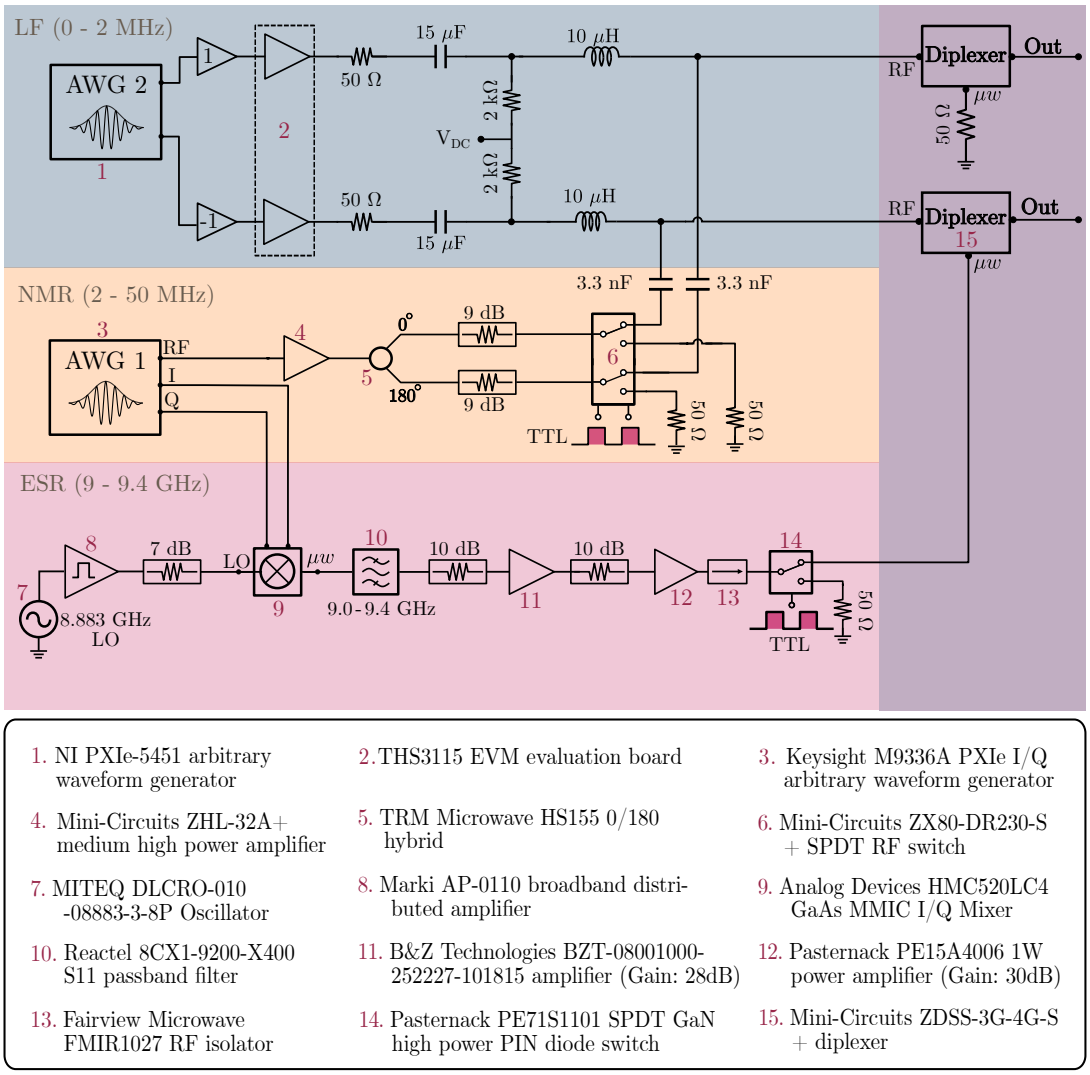


Figure 2.9: **Block Diagram of Electronics** Schematic of the circuit used for spin manipulation and detection. The circuitry for generating gradient modulation waveform is shown in the LF section. The RF pulses applied to the protons are generated via the circuitry in the NMR section. Both the RF and LF pulses are driven differentially to minimize the electrostatic coupling to the sample and are combined using a passive filter network. The microwave electronics used for electron control are shown in the ESR section, are driven single ended and are combined with the LF and RF pulses using the diplexer.

Meanwhile, one channel of AWG2 (Keysight M9336A PXIe I/Q AWG) is responsible

for generating the RF pulses that are used for NMR control as well as generating the AFPs that are used for spin detection during the MAGGIC protocol. To combine the RF and LF signal, a bias-Tee circuit was designed and characterized, with the low pass and high pass characteristics shown in Figure 2.10. Where the -3 dB cutoff of the LF and RF responses is roughly 1 MHz and 1.5 MHz, respectively. The primary requirement for this design was to maximize the bandwidth in which the RF pulses could be used to enable control of protons and potentially other nuclei, such as carbon, whose Larmor frequencies are 14 and 3.5 MHz, respectively, while ensuring minimal leakage into the LF branch of the circuitry.

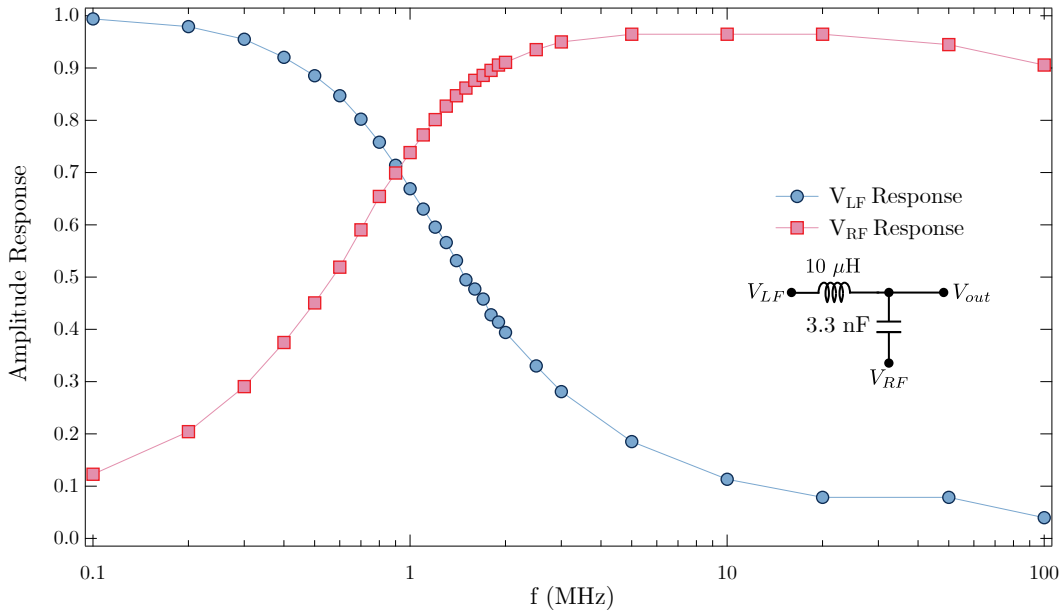


Figure 2.10: **BiasTee Filter** Measured LF and RF responses through the bias-Tee network. To measure the low pass response of the circuit V_{LF} was excited while the V_{RF} port was terminated to ground. Similarly, the high pass response was measured by exciting V_{RF} and terminating the V_{LF} port.

Another important aspect of the circuit design that must be considered is output noise from the RF and microwave amplifiers, which can cause undesirable relaxation. As a result, high-frequency switches are placed after the amplifiers to ensure the amplifiers are only on during the application of RF or microwave pulses. Note that the timings of the output pulses and switches are controlled with an FPGA digital circuit shown in Figure 2.4. However, a challenge when implementing the control pulses for the switches is ensuring

that the output from the FPGA is correctly synchronized with the clocks of the AWG responsible for outputting the pulses. For example, in the DNP experiments, given the fast sampling rate of the AWG, which is 1.2 GSa/s, and the long duration of the DNP experiments ~ 7 s, small phase variations between the clocks of the FPGA and AWG can lead to the amplifier being switched off or on unintentionally. To solve this problem, we use an external 10 MHz Rubidium clock from which the FPGA and AWGs derive their clocks, ensuring both are phase synchronous.

In order to generate the pulses used for ESR control at microwave frequencies, a single-sideband IQ mixer is used to up-convert a baseband signal at an intermediate frequency (IF), $\sim \omega_{IF} = 374$ MHz to the Larmor frequency of the electrons, $\omega_{0S} = 9.26$ GHz. The IF signal consists of the in-phase ($I(t)$) and quadrature ($Q(t)$) envelope functions that are defined and mixed in software and are outputted from AWG1 at the IF frequency. An IQ mixer upconverts the baseband ($I(t)$ and $Q(t)$) signals to generate the control pulse at $\omega_{LO}+\omega_{IF}$ using the scheme shown in 2.11, where ω_{LO} is the frequency of the reference local oscillator (LO). The LO has a constant sinusoidal output at $\omega_{LO} = 8.8883$ GHz that is split into two branches that are phase shifted 90° relative to one another. The two branches are then multiplied with the baseband $I(t)$ and $Q(t)$ signals, where Q port is mixed with the phase-shifted signal [72]. The two branches of the signals are then combined to generate a signal at $\omega_{LO} + \omega_{IF}$.

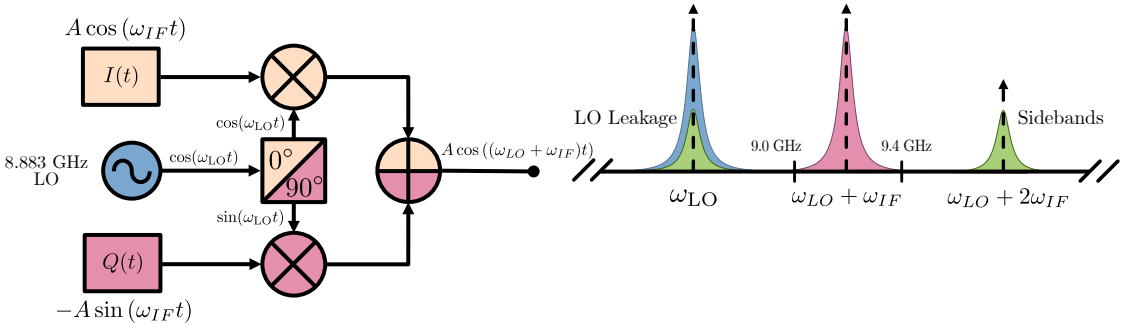


Figure 2.11: **Frequency Upconversion.** IQ mixer multiples LO with the baseband IQ signals and combines them to generate an output at $\omega_{LO}+\omega_{IF}$. A non-ideal IQ mixer can also generate unwanted sidebands at harmonics of ω_{IF} as well as spectral content at ω_{LO} (LO leakage)

An ideal mixer will generate spectra at only $\omega_{LO}+\omega_{IF}$ however, in practice, imperfections in the mixing due to amplitude and phase imbalances in the I and Q mixing paths

generate unwanted sidebands at different harmonics of the baseband carrier frequency, as well as LO leakage [72, 73]. To minimize pulse distortions that may result from additional sidebands generated by the IQ mixer, a filter is placed after the mixer to prevent unwanted frequency components in our signal. The filter's pass-band is designed to be between 9.0 and 9.4 GHz, thereby filtering out frequency content due to LO leakage and the sidebands. One disadvantage of mixing and then filtering the signal, however, is that it restricts the available bandwidth of the control pulses that can be applied. Figure 2.12 shows the amplitude and phase response of the filters used in our experiment.

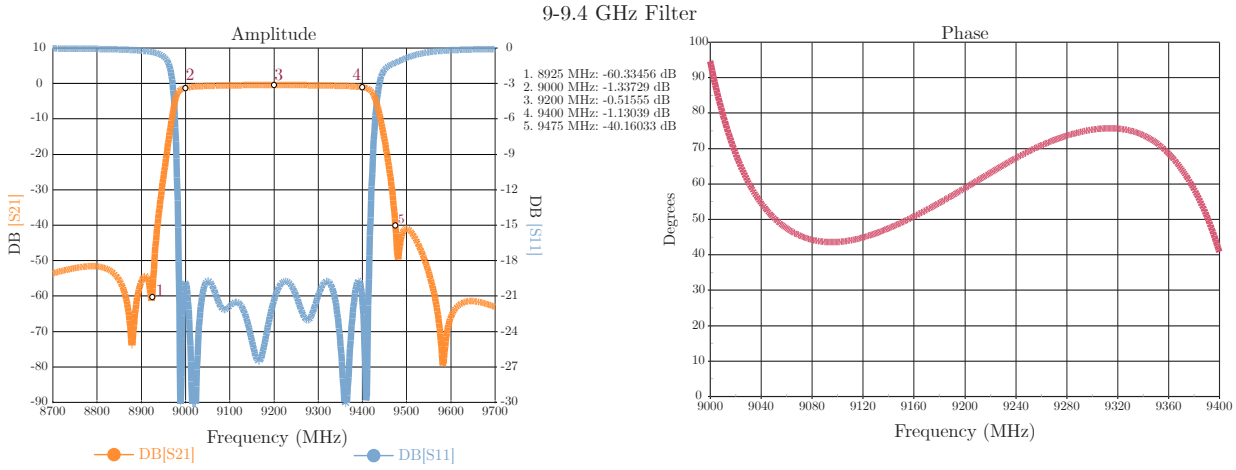


Figure 2.12: **Amplitude and Phase Response of Reactel 8CX1-9200-X400 Filter. (A)** Amplitude Response. The passband of the filter is designed to be between 9 and 9.4 GHz. **(B)** Phase Response.

Another consideration when designing the IQ mixer microwave circuit is the phase noise of the LO. Ideally, the reference oscillator that is used for mixing is a noiseless pure tone at ω_{LO}. No oscillator is ideal, however, and due to the presence of phase noise, there will be some spread in spectral content around the LO frequency. This will contribute to unwanted frequency content in the mixed signal [74]. Phase noise of the oscillator is typically characterized by measuring the output power within a 1 Hz bandwidth relative to the carrier frequency as a function of offset frequencies from the carrier. Figure 2.13 shows the phase noise response for the LO used in our experiments.

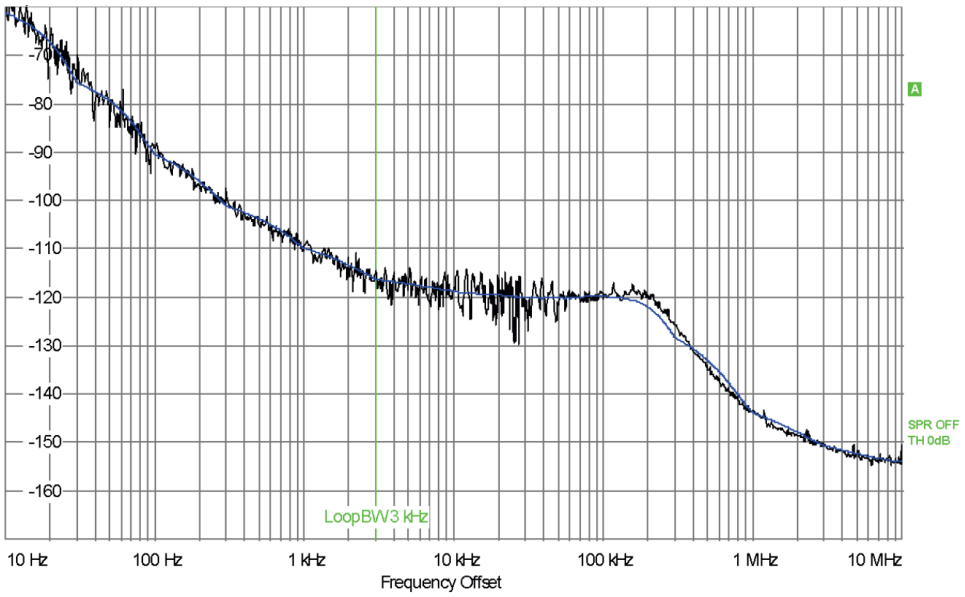


Figure 2.13: **Phase Noise of LO supplied by nardarmiteq.**

Due to the implementation of internal circuitry used for the IQ mixers, rather than using a sinusoid as the input for the LO path, it is beneficial to use a square wave input instead, which improves the mixing performance and reduces the levels of spurious harmonic frequencies [75]. The Marki AP-0110 broadband amplifier operating in the saturation regime was used to generate the square wave input.

A key consideration in the design of the microwave electronics is the insertion loss through coaxial cables and microwave components. Maximizing the current through the CFFGS is critical as the strength of the B_1 field produced is directly proportional to the current density through the CFFGS. In general greater B_1 fields can enable shorter duration pulses with higher fidelities, as well as higher resolution imaging, and offers greater flexibility and control when engineering pulses. The primary source of attenuation in our experiment are beryllium copper coax cables that carry the currents to the CFFGS from the output of the diplexer, with a loss of $\sim$ 24.5 dB. To overcome this insertion loss, a 1 W power amplifier with a gain of 30 dB was used to provide sufficient amplification to achieve the necessary current through the CFFGS. In the experiment, we were able to achieve a peak current of 6 mA through the constriction corresponding to a Rabi frequency

of roughly 80 MHz near the tip of the sample, and was large enough to enable DNP and application of ESR pulses for studying the electron spins. An additional pre-amplification stage was inserted to bias the input power to the second stage 1 W amplifier to ensure maximum amplification could be achieved while still operating within the linear regime of the amplifier. To minimize pulse distortions, as mentioned previously, it is important to operate in the linear regime of the amplifiers. The $P_{1\text{dB}}$ compression point is one measure used to set an upper bound on the linear output regime of the amplifiers. The $P_{1\text{dB}}$ compression is defined as the point where the output power of the amplifier deviates from an ideal linear response by 1 dB. Figure 2.14 shows the measured response of the entire microwave circuit where P_{out} is output from the diplexer and P_{in} is the input power to the IQ mixer from AWG1. Note that the figure includes any losses that may occur through coaxes connecting different components together. The measured $P_{1\text{dB}}$ compression point occurs at 29.44 dBm.

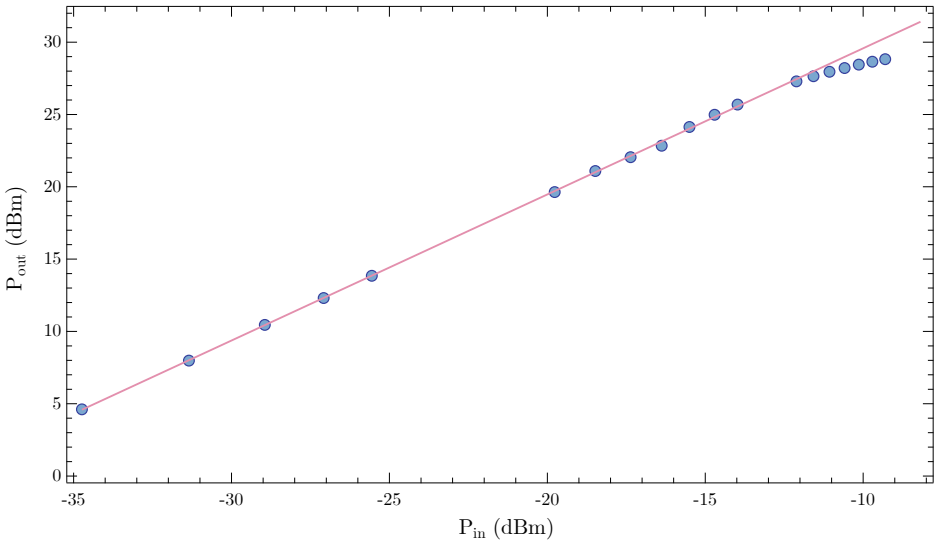


Figure 2.14: **Output power of Microwave Electronics circuit.** Measured output power at the output of the diplexer as a function of the input power incident to the IQ mixer. The measured $P_{1\text{dB}}$ compression point is at 29.44 dBm.

Additionally, an isolator circuit is placed in front of the amplifier to protect it from damage in the event there are high power reflections travelling back towards the output port of the amplifier. The 10 dB attenuator shown in the circuit schematic, is used to bias the input power to the amplifiers as well as to minimize reflections when connecting

different microwave components.

To characterize the extra noise added by the amplifier, the noise figure of the 1 W amplifier is quoted as 3 dB. The noise figure NF of a system is defined as the ratio of the signal-to-noise power at the input to the signal-to-noise power ratio at the output NF $= (S_i/N_i)/(S_0/N_0)$. For an ideal amplifier, $NF = 1$, as no extra noise is added to the signal. Noise from the amplifiers corresponds to a current noise in the CFFGS, which can cause unwanted relaxation of the electron spins [76, 77]. If the noise has spectral content at the electron Larmor frequency, it can cause shorter spin-lattice relaxation times [78]. Similarly, spectral content at the Rabi frequency can cause a decrease in the spin-lattice relaxation time in the rotating frame $T_{1\rho}$. To minimize the effect of noise from the amplifiers, a fast, high-powered switch is placed before the diplexer to ensure the amplifier is on only when pulses are applied [24].

Chapter 3

Ramped Amplitude DNP Protocol

The force-detected magnetic resonance setup presented thus far, relies on a CFFGS to generate the magnetic field detection gradients, as well as the B_1 fields used for spin control. Figure 2.3(A) shows the non-uniformity of the Rabi fields. Due to this non-uniformity, when using the NOVEL protocol for DNP the Hartman-Hahn matching condition would only be satisfied in a particular region of our sample. To mitigate this, we implement a modified version of the NOVEL protocol known as ramped-amplitude NOVEL (RA-NOVEL), which allows for efficient polarization throughout our sample and is robust to the spatial variation in the Rabi field. In NOVEL, the spins are tipped into the transverse plane with a $\pi/2$ pulse followed by a continuous resonant spin locking drive. Under the continuous drive, polarization is exchanged between the electrons and nuclei. However, in powder or amorphous samples the distribution of dipolar couplings and distances between molecules in the sample causes inefficient polarization transfer [46]. This is because the different couplings cause the state of all spin pairs to evolve at different rates.

In RA-NOVEL the amplitude of the drive is adiabatically swept through the Hartman Hahn condition, $\omega_{1S} = \omega_{0I}$. Adiabatic evolution refers to the fact, that if a state starts out as an eigenstate of the Hamiltonian, and if the Hamiltonian is changed slowly then, it will remain in an instantaneous eigenstate during the evolution [79]. For RA-NOVEL, this means that so long as the sweep rate of the drive is long compared to the times scale of the pseudo-secular coupling, and long compared to timescale of the microwave frequency, then adiabatic exchange of polarization will occur for all spins regardless of their orientations relative to the static field, and distribution of distances between spin pairs [46]. As a result of this, RA-NOVEL has shown higher polarization transfer efficiency compared to NOVEL [46].

As mentioned previously, The polarization occurs via adiabatic evolution of the eigenstates from $|\uparrow\uparrow\rangle$ to $|\downarrow\downarrow\rangle$, while the $|\downarrow\uparrow\rangle$, and $|\uparrow\downarrow\rangle$ states are left invariant in the case where the DQ transition is excited. To satisfy the adiabatic condition, the ramp rate $\dot{\omega}_{1S}$ must satisfy the condition $B^2/16\dot{\omega}_{1S} \gg 1$ [46]. With adiabatic sweeps the differences in coupling strengths do not matter, so long as the sweep is slow compared to the smallest couplings in the system, the spins states can be exchanged. Additionally, the adiabatic condition also implies that stronger pseudo-secular couplings enable faster sweep rates [46].

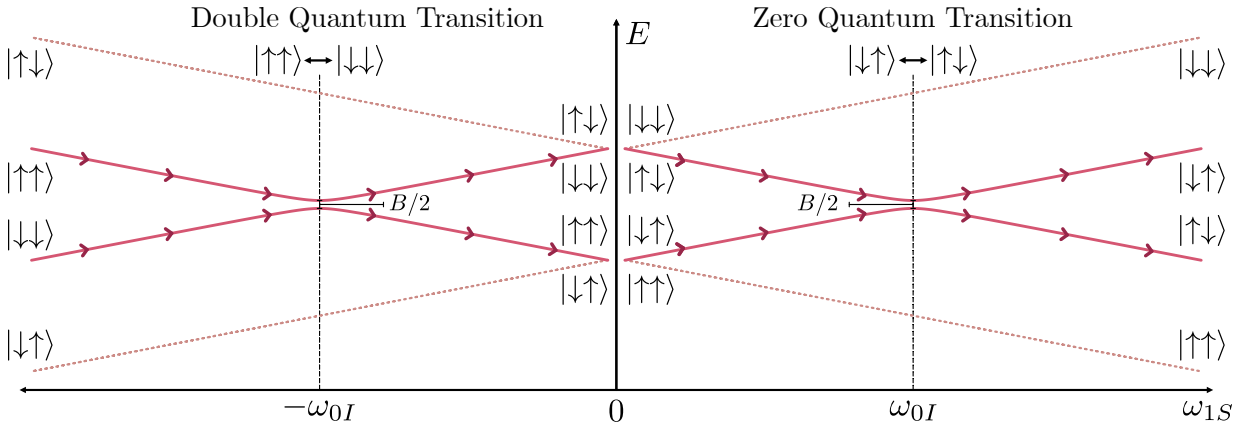


Figure 3.1: **Double Quantum and Zero Quantum Transitions**. The eigenstates trajectory calculated from Equation 1.33 and 1.34. The Rabi field is swept adiabatically through the Hartmann-Hahn matching frequency (shown in red arrows). The state adiabatically follows the trajectory from the $|\uparrow\uparrow\rangle \leftrightarrow |\downarrow\downarrow\rangle$ for the double quantum transition, and $|\downarrow\uparrow\rangle \leftrightarrow |\uparrow\downarrow\rangle$ for the zero quantum transition. The energy splitting between the two eigenstates is also shown, where at $\omega_{1S} = \pm\omega_{0I}$, the splitting is $B/2$, where B is the pseudo-secular hyperfine coupling. Note, that the $|\uparrow\downarrow\rangle, |\downarrow\uparrow\rangle$ states are left invariant during the double quantum transition and similarly the $|\uparrow\uparrow\rangle, |\downarrow\downarrow\rangle$ states are left invariant during the zero quantum transitions.

In Figure 3.1, we plot the eigenstates of the polarization transfer Hamiltonian as a function of applied Rabi frequency for a double quantum or zero quantum transitions. Polarization transfer occurs when the Rabi field is swept through the Hartmann-Hahn condition. In the case where we excite the double quantum transition, $\omega_{1S} = -\omega_{0I}$, from the figure, we can see that if the an electron-proton spin system begins in $|\uparrow\uparrow\rangle$, and the Rabi field is swept adiabatically, the system will end up in the $|\downarrow\downarrow\rangle$ state.

In addition to RA-NOVEL providing a higher efficiency of polarization transfer, a ramped waveform allows for polarization transfer to occur even when there is spatial vari-

ation in the Rabi frequency, which is present in our force-detected magnetic resonance setup.

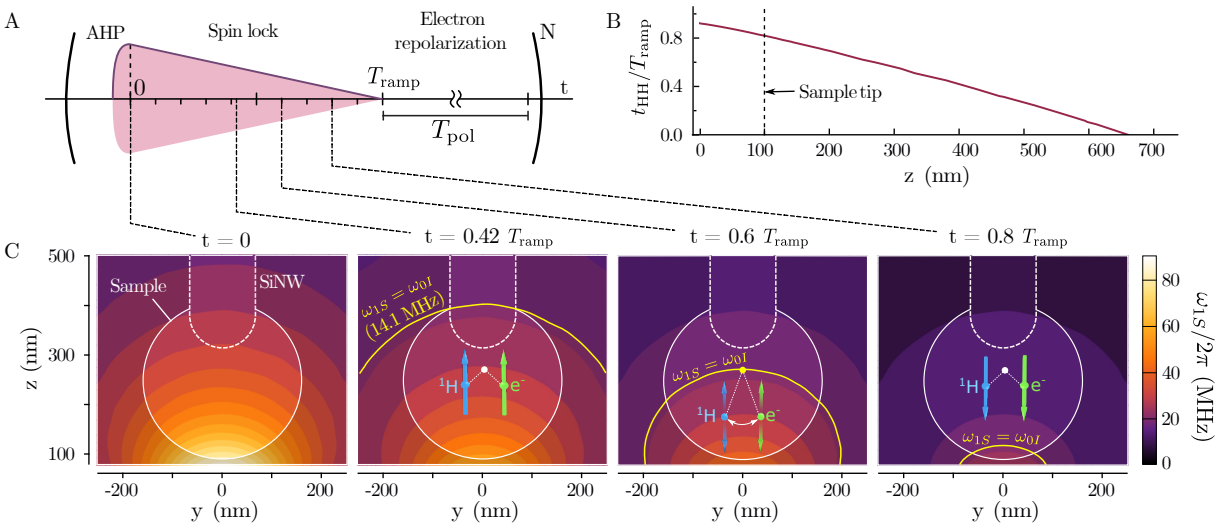


Figure 3.2: **RA-NOVEL. (A)** RA-NOVEL waveform primitive applied to the electrons consisting of an adiabatic half passage (AHP) to the tip the spins into the transverse plane, followed by an electron spin locking pulse that is swept to 0 over a duration T_{ramp}, followed by repolarization of the electrons for a time T_{pol}. By repeating the waveform N times, the proton polarization in the sample can be built up for a time T_b, which is limited by the T_{1p} of the protons. **(B)** The time at which the Hartmann-Hahn matching condition is met (t_{HH}) for an electron-proton pair at a distance z from the center of the CFFGS ($x = 0, y = 0$) during the ramp waveform. **(C)** Rabi contours during different stages of the ramp. The yellow contour outlines where the Hartmann-Hahn condition is met. As ω_{1S} is swept through the matching condition, an electron-proton pair (white circle) will undergo adiabatic transfer of polarization. Due to the inhomogeneity in the B_1 field spin furthest away from the CFFGS undergo exchange at earlier times of the ramp than spins near the sample tip. The arrows shown indicate the spin states in the tilted rotating frame.

The RA-NOVEL pulse sequence used in our DNP experiments is presented in Figure 3.2(A). The RA-NOVEL waveform primitive begins by tipping the electron spins into the transverse plane using an adiabatic half passage (AHP), and applying a resonant spin locking drive that is linearly swept to zero with a duration of T_{ramp}. We then wait for a time T_{pol} during which the electrons begin to repolarize to their Boltzmann populations.

Additionally, it is during the T_{pol} time that the enhanced proton polarization is carried away into the bulk sample via spin diffusion.

Figure 3.2 [24] illustrates the ω_{1S} contours generated by the CFFGS. The yellow contour shows the Hartman-Hahn matching condition, where $\omega_{1S}/(2\pi) = \omega_{0I}/(2\pi) = 14.1$ MHz. The figure shows that the Hartmann-Hahn condition is satisfied at different times for different regions. Thus, by employing a ramped-amplitude waveform, we not only allow for adiabatic polarization transfer, but also sweep the matching condition throughout the entire sample where spins furthest away from the CFFGS will undergo polarization exchange first, and spins closer to the CFFGS will transfer towards the end of the ramp. So long as the initial drive amplitude is large enough such that spins far away from the CFFGS begin with a Rabi frequency greater than the proton Larmor, all spins in the sample will undergo polarization transfer as the amplitude is swept to zero.

Through successive applications of the RA-NOVEL waveform, the polarization in the sample can be built up [46]. The total length for which the RA-NOVEL DNP protocol can be applied is limited by the spin-lattice relaxation time of the protons, T_{1p} as any buildup in polarization beyond this timescale will cancel with the decay in polarization from the T_{1p} process for longer and longer build-up times.

The timescale of different relaxation mechanisms is crucial when doing DNP. The spin-lattice relaxation time of the electrons T_{1e} determines how long it will take the electrons spins to repolarize. A shorter T_{1e} will mean that the DNP primitive waveform can be repeated more often for a fixed buildup time, and polarization can be transferred at higher rates enabling greater enhancements. Conversely a long T_{1e} increases the length of the T_{pol} time thereby reducing the repetition rate of the RA-NOVEL waveform primitive, and the maximum possible enhancement in polarization. The electron spin-lattice relaxation time under a constant drive $T_{1\rho}$ sets the maximum duration of the spin locking pulses. A larger $T_{1\rho}$ enables longer ramps which satisfy the adiabatic condition, ensuring efficient polarization exchange. As mentioned previously, the DNP buildup time is also limited by a timescale on the order of the spin-lattice relaxation time of the protons T_{1p} as this dictates the total build-up time.

Chapter 4

Nanoscale DNP

Applying the techniques of dynamic nuclear polarization along with the enhanced detection sensitivity of magnetic resonance force microscopy provides an exciting opportunity to image nanoscale ensembles, in $\sim$ (100 nm)^3 volumes, especially for imaging biomolecules such as proteins and virus particles. These regimes were previously extremely difficult or unfeasible to explore using conventional NMR techniques. DNP-enhanced nanoMRI can provide an improvement in SNR over schemes that measure the statistical polarization of nanoscale ensembles.

As mentioned previously, for nanoscale samples statistical polarization usually yields significantly higher SNR over thermal polarization. Firstly, for small ensembles, the fluctuations in the number of up vs down spins are much larger than the mean polarization of the sample; i.e statistical polarization is greater than thermal polarization. Secondly, when measuring thermal polarization, there is an overhead in the experiment duration to wait for the magnetization to repolarize between measurement blocks, whereas when measuring the statistical population there is no such requirement, which allows for more averaging in the same experiment duration. Therefore, the DNP process must have sufficient enhancement to overcome the continuous data acquisition advantage of statistical polarization.

In this section, we discuss force-detected magnetic resonance measurements that use the RA-NOVEL DNP protocol and trityl-OX063 radicals to enhance the polarization of protons suspended in a sugar-water nanodroplet attached to the tip of a SiNW. We discuss optimizing the efficiency of the DNP process by measuring the dependence of the enhancement on different parameters in the RA-NOVEL protocol. Furthermore, we demonstrate the improvement in SNR enabled by DNP compared to statistical polarization measurements.

Different relaxation mechanisms play important roles in achieving large enhancements in DNP. Importantly, we observed increased spin-lattice relaxation rates of the OX063 electron spins due to spin diffusion to fast-relaxing paramagnetic defects on the surface of the SiNW. The increased relaxation rates allow for a shorter T_{pol} in the RA-NOVEL primitive waveform, thereby increasing the efficiency of the DNP process. In this section, we present spin diffusion simulations that accurately model the effect of fast-relaxing defect spins on the intrinsic T_1 of the trityl-OX063 radicals. The figures and data presented in this chapter can be found in Reference [24], of which I am a co-author.

4.1 DNP measurements

To quantify the enhancement in polarization DNP provides, we use the RA-NOVEL pulse sequence shown in Figure 4.1(A). The sequence begins by scrambling the initial proton polarization [46]. We then transfer the electron polarization to the protons for a buildup time $T_b = N(T_{\text{ramp}} + T_{\text{pol}})$, where N refers to the number of repetitions of the RA-NOVEL waveform primitive. Note that we have omitted the duration of the AHP pulsed used for tipping the spins into the transverse plane, as its 70 ns duration is negligible. The MAGGIC protocol is then used to measure the average force signal (Equation 2.6) coming from the hyperpolarized proton polarization. The measured time records were then processed with the matched filtering scheme discussed in Section 2.3.1. The average measured force for a given time record $F(t)$ is constructed as $\bar{F} = \int_0^{\tau_0} dt\ w(t)F(t)$, where τ_0 is the length of the measure block, and $w(t)$ is the matched filter kernel. The bare thermal polarization of the protons was measured in a similar fashion, by first scrambling the proton polarization and then waiting for a buildup time of T_b during which the protons repolarize before measuring the polarization using MAGGIC.

The *enhancement* η in proton polarization due to the DNP process is defined as $\eta(T_b, T_{\text{pol}}, T_{\text{ramp}}) = \bar{F}_{\text{hp}}(T_b, T_{\text{pol}}, T_{\text{ramp}})/\bar{F}_{\text{th}}(T_b)$, which is the ratio of the hyperpolarized $\bar{F}_{\text{hp}}$ and thermal $\bar{F}_{\text{th}}$ matched filter outputs for the same buildup time T_b. During the polarization process, there are competing dynamics to consider. While extending the polarization buildup time T_b can yield higher enhancement factors, it also results in a higher overhead time in the experiment, thereby lowering the number of acquisitions. Importantly, the tradeoff between increased polarization buildup and lower acquisition rates points towards an optimal buildup time set by the $\sim T_{1p}$, where $\sim T_{1p}$ is the spin-lattice relaxation time of the protons, thereby limiting the maximum enhancement that can be achieved. Thus, there exists an optimal buildup time $T_{\text{b,opt}}$ that maximizes the detection SNR of the measured signal. To determine the optimal DNP buildup time $T_{\text{b,opt}}$, we measure the hy-

perpolarized signal as a function of buildup time, as depicted in Figure 4.1(B)(inset), and measure the time constant τ_{DNP} of the buildup curve. The optimal T_b is chosen such that it maximizes the detection SNR, which is $\propto \sqrt{N_{\mathrm{avg}}}(1 - e^{-T_b/\tau_{\mathrm{DNP}}})$, where N_{avg} represents the number of averages, and is defined as the ratio of the total experimental duration T_e to the buildup time T_b [24]. For subsequent measurements involving DNP we set the buildup time to be $T_b = T_{\mathrm{b,opt}}$. In this section we will mainly focus on data measured for Sample A, where the buildup time was determined to be $T_{\mathrm{b,opt}} = 7.7$ s. The full set of parameters for the DNP process along with measured enhancements for the different samples is presented in Table 4.1.

Table 4.1: **Summary of nanoscale DNP results**, including measured DNP enahncements and spin relaxation times.

	Sample	**A**	**B**	**C**	**D**
DNP performance	η_{opt}	105(8)	118(8)	78(3)	40.6(4)
	τ_{DNP} (s)	6.7(1)	0.67(1)	8.4(2)	14.9(5)
	$T_{b,\mathrm{opt}}$ (s)	7.7	0.8	10.5	20.8
	$T_{\mathrm{pol,opt}}$ (ms)	10.24	1.28	10.24	5.12
	$T_{\mathrm{ramp,tabopt}}$ (µs)	16	8	16	100
Relaxation times	T_{1p} (s)	10.2(3)	1.01(3)	10.8(6)	20(1)
	$T_{1\rho e}$ (ms)	2.5(1)	0.45(4)	3.5(1)	7.5(3)
	T_{1e} (ms)	20.5(3)	2.5(1)	28.6(7)	30.0(4)

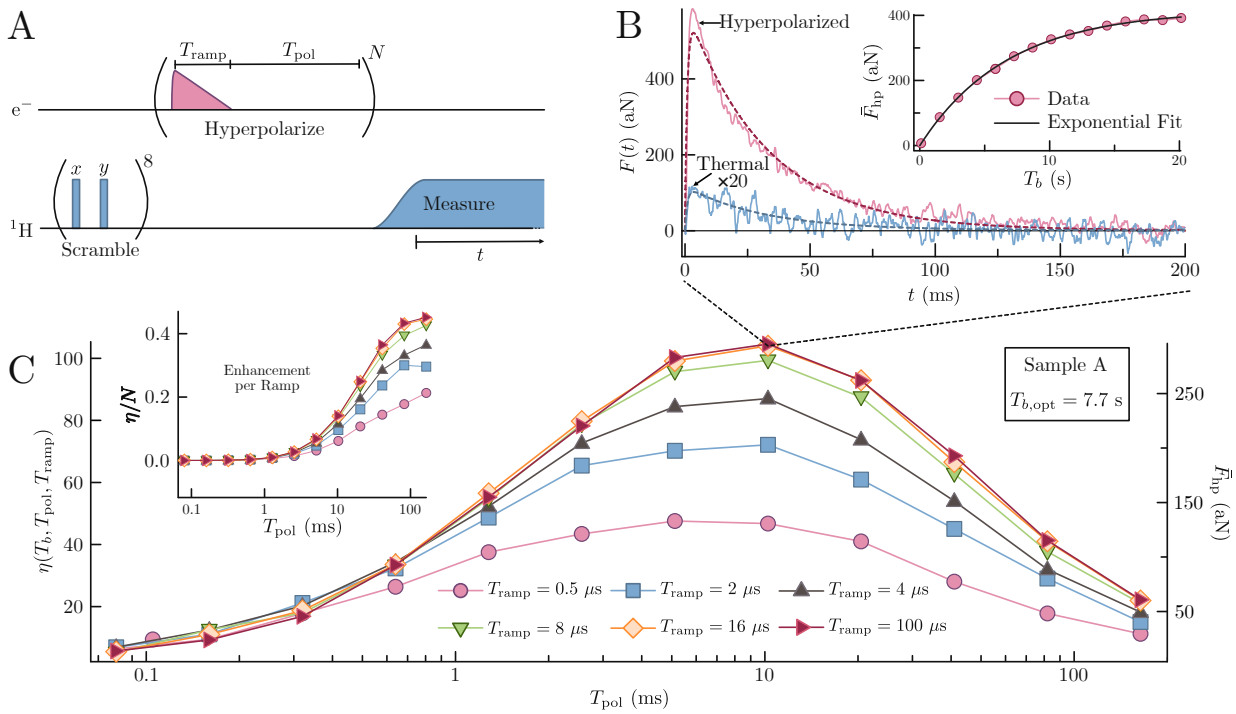


Figure 4.1: **DNP Measurements. (A)** Pulse sequence used for DNP measurements. The proton polarization is first scrambled using $(\pi/2)_x$ and $(\pi/2)_y$ pulses with a dephasing time in between. Repeated applications of the RA-NOVEL waveform primitive are then applied to the electrons for a build-up time T_b before measuring the magnetization of the proton spins. **(B)** Measured expectation values of the hyperpolarized (58 averages) and thermal (7080 averages) signals for Sample A. The data is fitted to a model of the mechanical response of the SiNW (dashed lines), with the initial rise in the data being due to the finite bandwidth of the oscillator. The signals decay with a spin correlation time $\tau_m = 31.9(2)$ ms. (Inset) DNP enhanced proton polarization as a function of build time (58 averages/point). **(C)** The DNP enhancement is shown for different T_{pol} and T_{ramp} for an optimal buildup time $T_{b,opt} = 7.7$ s (58 averages/point). (Inset) The enhancement per ramp depicts the increase in efficiency and saturation of polarization transfer for longer T_{pol} and T_{ramp}. We found the maximum enhancement $\eta = 105(8)$ in proton polarization with a $T_{\text{pol}} = 10.24$ ms and $T_{\text{ramp}} = 16$ μs.

In RA-NOVEL DNP, the maximum enhancement, η, depends on two factors: the electron repolarization time T_{pol}, and the ramp time T_{ramp}, during which the polarization transfer occurs. To optimize these parameters, we measured η as a function of these two

timescales, as shown in Figure 4.1(C). As expected, as the duration of T_{ramp} increased, the maximum enhancements increased as well, until either the ramp times exceeded the time scale set by the pseudo-secular hyperfine coupling or when the times scale became comparable to the measured spin-lattice relaxation time in the rotating frame $T_{1\rho e}$. The maximum η was achieved for a $T_{\text{ramp}} = 16$ μs which is significantly smaller than the measured $T_{1\rho e} = 2.5$ ms. Thus, the ramp duration is predominantly determined by the pseudo-secular hyperfine coupling strength B [24]. For a weaker coupling strength, we expect the optimal T_{ramp} time to increase in order to satisfy the adiabatic condition. Consequently, a strong coupling ensures that the ramp time for the DNP process can be short, enabling greater repetition of the primitive waveform. Furthermore, Figure 4.1 shows a trade-off concerning the duration of T_{pol}. While longer electron spin repolarization times (governed by T_{1e}) allow for a larger initial polarization to transfer at the beginning of a ramp, they reduce the maximum number of DNP waveform repetitions that can be applied within a fixed buildup time T_b, thereby lowering the maximum enhancement. The optimal T_{pol} was found to be 10.24 ms, beyond which η the enhancement begins to decrease. Note that the optimal T_{pol} is lower than the repolarization time constant set by T_{1e}. For longer T_{pol} durations, however, the polarization transfer in any given ramp should theoretically become more effective as a greater polarization is built up and subsequently transferred. To see this, we calculate the enhancement per sweep by normalizing the measured enhancement to the number of sweeps performed for a given build-up time. As demonstrated in Figure 4.1(C) (inset), the data shows that the efficiency of the polarization transfer increases with increasing T_{pol}. This is consistent with a larger amount of polarization being built up when T_{pol} increases. As T_{pol} surpasses T_{1e} significantly, the efficiency of transfer begins to saturate as the electron polarization has reached equilibrium.

For maximizing the enhancement achieved with DNP, it is beneficial to have short T_{1e}, without affecting T_{1p}, and creating spin diffusion barriers, as it allows for the maximum amount of polarization to be transferred from the electron at a higher rate. In our experiment, we note that the measured T_{1e} is shorter than reported values in literature at similar concentrations. Section 4.3 provides a detailed discussion of the measured relaxation rates and possible sources of the shortened T_{1e}. Figure 4.1(C) shows an enhancement of $\eta_{\text{opt}} = 105(8)$ with $T_{\text{pol}} = 10.24$ ms, and $T_{\text{ramp}} = 16$ μs.

This marks an advancement over previous works that have shown moderate enhancements of roughly 10 to 20 [3]. In addition, contrary to previous work where the enhancement varied within the sample, our platform allows for a polarization transfer process that is decoupled from the readout gradient, and is akin to traditional DNP techniques used in NMR and can be readily used for enhanced sensitivity in spectroscopy or imaging applications. This enhancement in the thermal polarization provides an improvement in

the detection sensitivity over statistical polarization, which we discuss in greater detail in section 4.2.

4.2 Comparison of Statistical Polarization and DNP Enhanced Thermal Polarization SNR

Previous discussions in this thesis mention that the polarization of the protons after DNP must not only be larger than the statistical polarization but must also be sufficiently large to overcome the higher acquisition rates when measuring statistical polarization, as discussed in Section 2.2. In this section, we provide an experiment that compares the signal enhancement provided by DNP compared to the signal obtained from statistical polarization. For a detailed treatment of the comparison between statistical and hyperpolarized signals, we refer the reader to the main text and supplements of Reference [24], where experimental and theoretical treatments are provided in greater detail.

To assess the SNR enhancement provided by DNP, the proton Rabi distribution was measured using the spatially varying B_1 gradients generated by the CFFGS for phase encoding of the proton spins. This Fourier encoding approach is detailed in previous studies [13, 14], where Rabi gradients from the CFFGS enabled one-dimensional phase encoding of proton spins. In this method, a resonant RF pulse is applied in the x-direction with the associated unitary transformation represented by $U(\mathbf{r},t) = e^{-iI_x\Theta(\mathbf{r},t)}$. Here, the spins accrue a position dependent phase $\Theta(\mathbf{r},t) = \gamma_p B_1(\mathbf{r}) = \omega_{1I}\tau$ where τ is the pulse duration, and $B_1(\mathbf{r})$ is the spatially varying Rabi field. The z-axis magnetization is then measured, with the signal being $s(\tau) \propto \int_0^\infty du\ \rho(u)\cos(2\pi u\tau)$, where $u = \omega_{1I}/(2\pi)$ is the Rabi frequency, and $\rho(u)$ is the Rabi-dependent spin density.

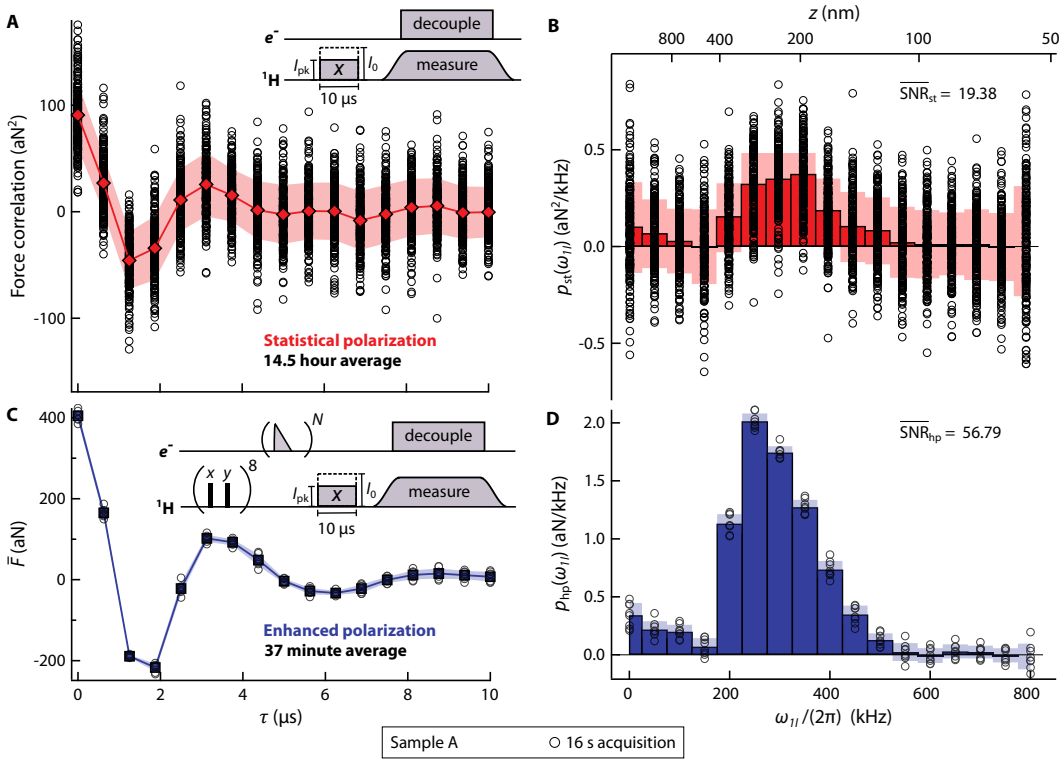


Figure 4.2: **SNR Comparison of DNP Enhanced and Statistical Polarization Experiments.** **(A)** Measured time-domain Fourier encoding data for **(A)** statistically polarized and **(C)** hyperpolarized proton spins in sample A. The corresponding images in the Rabi frequency domain are shown in **(B)** and **(D)**, with the top axis indicating the distance from the surface of the CFFGS ($z = 0$) along the center of the constriction ($x = y = 0$ line). The frequency resolution of each image is 50 kHz. The shaded regions indicate the standard deviation of the acquired data (open circles) for each point in the time record, and the corresponding Rabi frequency distributions. The insets show the pulse sequence used for the two types of measurement. We applied a constant amplitude excitation at ω_{0S} to decouple the electrons while acquiring the proton signal. The decoupling procedure resulted in extending the proton spin correlation time from 31.9 ms to 135.6 ms during the acquisition period. The differences observed in the statistical and hyperpolarized distributions stem from how each spin interacts with the detection gradient. In statistical polarization, the contribution of a spin at position $\mathbf{r}$ to the signal is proportional to $G^2(\mathbf{r})$, while for the hyperpolarized signal, $G(\mathbf{r})$. Consequently, spins closer to the CFFGS have a more pronounced impact on the statistically polarized image, leading to increased spectral content at higher Rabi frequencies in **(B)** compared to **(D)**.

In our experiment, we applied 10 μs long resonant pulses. The amplitude I_{pk} of the pulses was varied in 17 steps between 0 mA and 29 mA, and the spin signal was recorded as function of effective encoding time $\tau_{\text{eff}} = 10\ \mu\text{s} \times I_{pk}/I_0$, where $I_0 = 29$ mA is the maximum current pushed through the CFFGS. The data that compares the SNR of the statistical and hyperpolarized Rabi distributions for sample A is provided in Figure 4.2 [24]. For the DNP data, we first hyper-polarize the proton spins using the optimal DNP parameters for sample A, $T_{\text{pol}} = 10.24$ ms, $T_{\text{ramp}} = 16\ \mu s$, $T_b = 7.7$ s. The measure block lengths were 400 ms in length. In Figure 4.2(C) where we present the time-domain Fourier data, the open circles corresponds to the average of two measurements of the signal, with a total duration of $2T_b + 2\tau_{\text{enc}} + 2\tau_0 = 16.3$ s, where τ_{enc} refers to the duration of the phase encoding pulses, and τ_0 is the measure block duration. For the measurements made with statistical polarization, the spin signal was collected continuously for 16.1 s where the average force was calculated from 100 ms long measure blocks that were applied before and after the 10 μs long encoding pulses, from which we construct the average correlation of consecutive measurements [24]. Each open circle in Figure 4.2(A) represents the average measured correlation over a period of 16.1 s. This time was chosen to avoid clutter in the Figure. For the statistical polarization measurements, the filled points represent the average over 192 data points for each value of τ_{eff}, which amounts to a total experiment time of 14.5 h. For the hyperpolarized data set, the number of measured data points for a given τ was 8, which corresponds to a total measurement time of 37 min. The measured Rabi-frequency distribution and its corresponding standard deviation are represented by $p(\omega_{1I})$ and $\sigma_p(\omega_{1I})$ respectively [24]. The average SNR is then defined as $\overline{\text{SNR}} = \sum_{i=1}^{17} p(\omega_i)\ \text{SNR}_i / \sum_{i=1}^{17} p(\omega_i)$, with ω_i represents the i^{th} Rabi frequency bin and $\text{SNR}_i = p(\omega_i)/\sigma_p(\omega_i)$ [24]. The measured SNR for the hyperpolarized data was $\overline{\text{SNR}}_{\text{hp}} = 56.79$, and for statisitical was $\overline{\text{SNR}}_{\text{st}} = 19.38$. Thus, in order to reach the same SNR for hyperpolarized and statistical data, this equates to a reduction in averaging time for the DNP data of $(\overline{\text{SNR}}_{\text{hp}}/\overline{\text{SNR}}_{\text{st}})^2 \times 14.5\ \text{h}/37\ \text{min} = 204$ [24]. This is significant as not only is DNP-enhanced polarization of the proton spins larger than the statistical polarization, but the experiment reveals that enhancements of 105 can yield a reduction in averaging time by a factor of 200 fold.

Measurements of a similarly prepared sample (Sample C) also yielded similar results. The parameters used in the DNP sequence were $T_b = 10.5$ s, $T_{\text{pol}} = 10.24$ ms, and $T_{\text{ramp}} = 16\mu$ s, with a measure block duration $\tau_0 = 500$ ms. Similar to the previous statistical polarization measurements, the data was taken with 100 ms measure block lengths. The total duration of the statistical measurements was 15.2 h, and for hyperpolarized measurements, it was 2.1 h. The measured SNRs were $\overline{\text{SNR}}_{\text{hp}} = 112.05$, $\overline{\text{SNR}}_{\text{st}} = 21.99$, and yielded a reduction in averaging time of 189 to achieve the same average SNRs for statistical and hyperpolarized data sets [24]. Additionally, the result shows that the sample attach-

ments of the nanodroplets on the SiNW can faithfully reproduce the large enhancements observed in Sample A.

4.3 Relaxation

In this section, we characterize the relaxation time scales of the electron and proton spins in Sample A at 6 K. The T_{1p}, $T_{1\rho e}$, T_{1e} are of particular interest as they play an important role in the DNP process. The T_{1e} was measured with an inversion recovery sequence. Firstly, the electrons are given some time to polarize. The polarization is then inverted with an AFP pulse. We then wait a variable time τ to allow the spins to equilibrate and then measure the magnetization. As mentioned in section 2.4, we use fast high-powered switches to ensure that during the polarization time and variable time τ, noise from the amplifiers does not induce any unwanted relaxation of the spins.

The electron T_{2e}^*, due to inhomogeneous broadening, was measured with a Ramsey experiment with time-proportional phase-increment (TPPI) scheme [80]. The spins were tipped to the transverse plane with an AHP, followed by a variable free evolution time τ over which the spin evolves due to dipolar interactions, as well as other sources such as local fields from neighboring spins that induce resonance offsets. An inverse AHP is then applied to bring the spins back to the z-axis where the magnetization is measured. A phase shift $\varphi = \omega_{\text{TPPI}}\tau$ was added to the inverse AHP, where φ varied in proportion to τ, to artificially add a resonance offset to shift the spectrum to an offset frequency of $\omega_{\text{TPPI}}/(2\pi) = 30$ MHz. This offset introduces oscillations into the measured spectrum, which can help to determine the center frequency. Without TPPI, if the carrier frequency of the drive is on resonance, then the signal would be proportional to $e^{-\tau/T_{2e}^*}$. However, if there is a difference δf between the carrier frequency and Larmor then the signal is proportional to $\cos(2\pi\tau\delta f\tau)e^{-\tau/T_{2e}^*}$. TPPI can be used to introduce more oscillations to provide a better fit to the data, especially if δf is small compared to the times scale of decay T_{2e}^*. We can fit the measured signal to the following form $\cos(2\pi\tau(\delta f + \omega_{\text{TPPI}}/2\pi))e^{-\tau/T_{2e}^*}$. For electrons the measured $\delta f = -144$ kHz.

The spin-lattice relaxation time under constant dive $T_{1\rho e}$ was measured by tipping the spins into the transverse plane, after which a resonant spin-locking drive is applied for a variable time τ after which the spin is tipped back to point along the z direction. We also ensure that during the application of the pulses, the RF amplifier is switched off to prevent unwanted relaxation of the electron spins.

Relaxation measurements of proton spins were made after applying DNP pulses, with a $T_{b,\text{opt}} = 7.7$ s, to increase the detection SNR. T_{1p} measurements were made by allowing

the hyperpolarized spins to equilibrate for a variable time τ, after which the longitudinal magnetization was measured. For measuring the spin-spin relaxation time T_{2p}, which is the dephasing time of the spins in the transverse plane due to dipolar interactions, a σ_z decoupling sequence made up of repeated applications of AFPs, and a free evolution time of $\delta\tau = 5$ μs is used [24,81]. The T_{2p} is measured by applying an AHP, after which the spin is allowed to evolve under the σ_z decoupling sequence for a total free evolution time $\tau = n\delta\tau$ which is varied, after which an inverse AHP is used to align the spins with the z direction. T_{2p}^* measurements were made in a similar fashion to the electrons. $\omega_{\mathrm{TPPI}}/(2\pi) = 80$ kHz, and was fit to a Gaussian decay $\propto e^{-(\tau/T_{2p}^*)^2}$, with $\delta f = 5.2$ kHz from the fit. Figure 4.3 provides the measured relaxation data for Sample A. Table 4.2 presents the relaxation data for all samples.

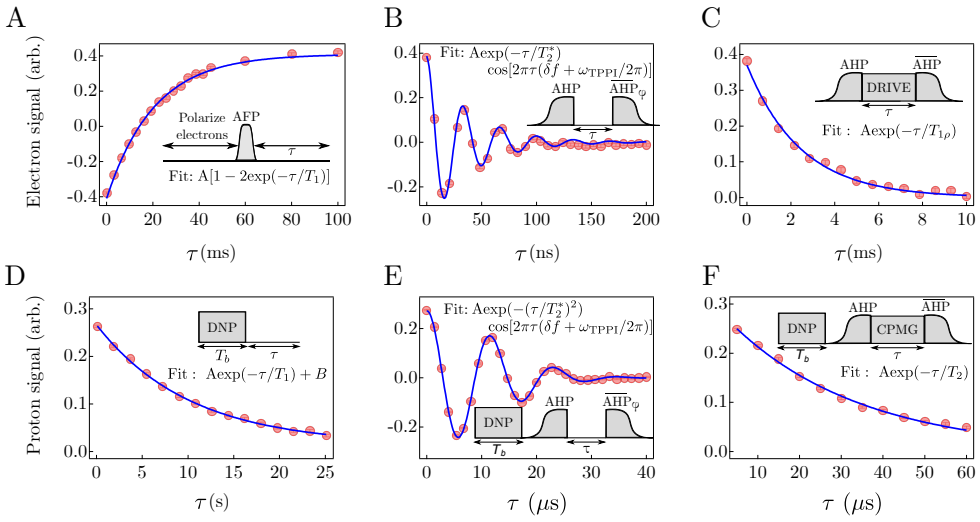


Figure 4.3: **Relaxation Times.** Spin relaxation data for Sample A, with associated pulse sequences. **(A)** T_{1e} measurement, with inversion recovery pulse sequence. **(B)** Electron T_{2e}^* measurement using a Ramsey experiment with a time-proportional phase increment (TPPI) scheme, ($\omega_{\mathrm{TPPI}}/(2\pi) = 30$ MHz). **(C)** Electron $T_{1\rho e}$ measurement with a resonant constant-amplitude drive. **(D)** Proton T_{1p} measurement by measuring the decay in the longitudinal magnetization of the hyperpolarized proton ensemble. **(E)** Proton T_{2p}^* measurement using a Ramsey experiment on the hyperpolarized proton ensemble with $\omega_{\mathrm{TPPI}}/(2\pi) = 80$ kHz. **(F)** Proton T_{2p} measurement with a σ_z decoupling sequence on the proton hyperpolarized ensemble.

Table 4.2: **Electron and proton relaxation times** for the measured samples. T_{2p} and T_{2p}^* were not measured for sample D.

	Relaxation Time	**A**	**B**	**C**	**D**
Electrons	T_{1e} (ms)	20.5(3)	2.5(1)	28.6(7)	30.0(4)
	T_{2e}^* (ns)	38(2)	27(3)	42(2)	50(3)
	$T_{1\rho e}$ (ms)	2.5(1)	0.45(4)	3.2(1)	7.5(3)
Protons	T_{1p} (s)	10.2(3)	1.01(3)	10.8(6)	20(1)
	T_{2p}^* (μs)	17.0(2)	16.8(2)	16.8(2)	-
	T_{2p} (μs)	31.4(7)	31(1)	30(1)	-

Of particular interest from the measured data was the measured T_{1e} of the sample. As mentioned previously, T_{1e} plays a critical role in the DNP process as it affects the time that must be spent repolarizing the electron spin, T_{pol}. A short T_{1e} would enable greater repetition of the DNP primitive waveforms, potentially allowing for greater efficiency and larger enhancements in proton polarization.

Previous studies of the T_{1e} of the trityl-OX063 radical in bulk samples have demonstrated that at concentrations ranging from 1 mM to 60 mM, the spin-lattice relaxation time varies from 10 s to 50 ms [25] at 6 K with a static field of $B_0 = 0.35$ T. This is in stark contrast to the much shorter T_{1e} measured in our nanoscale droplets attached to the tip of the SiNW. The samples prepared had a similar concentration range for the trityl radicals ranging from 1.3 mM - 49.4 mM but with T_{1e} ranging from 70 ms to 2.5 ms. In addition, samples that had similar concentrations also had large variations in the T_{1e}.

To determine the possible sources of relaxation, a dilute 1.3 mM reference sample was prepared, which had a measured $T_{1e} = 70$ ms. A dilute sample is used as it will exhibit higher sensitivity to external factors that may be causing relaxation. We first measured the thermal electron spin polarization of the spins as a function of temperature. To do this, we first measured the operating temperature of the SiNW. The temperature of the SiNW depends on the incident light level, which we characterize as follows: We measure the thermal displacement spectral density of the SiNW on a spectrum analyzer as a function of incident laser power. For each light level, the integrated power of the spectrum within a 5 kHz bandwidth centered at ω_c is subtracted from a baseline integrated power over the same bandwidth far away from resonance to take out the contribution of other noise sources to the interferometer signal. The integrated displacement power is shown in Figure 4.4(A) [24]. In the absence of incident light from the laser, the base temperature of the

SiNW should be at 4.2 K. At low light levels, we can fit a linear function to the first few points in the curve, where the temperature changes linearly with light power. The temperature calibration is achieved by setting the vertical intercept of the fit to be at 4.2 K, which corresponds to 0 incident light. The resulting temperature-light level calibration is depicted in Figure 4.4(A), where the blue dot in Figure 4.4(A) corresponds to the operating temperature of the experiment. As shown in Figure 4.4(B) using the calibration for the temperature in Figure 4.4(A), the electron polarization as a function of temperature can be measured by probing the electron signal at different incident light powers. During these measurements, the switches were on to prevent unwanted heating from the microwave amplifiers. A fit to the data shown in 4.4(B) shows that the electron spin polarization is inversely proportional to temperature, which is consistent with the Curie-Weiss Law. From this, we conclude that the spins are thermalizing toature the SiNW temper and that the additional relaxation mechanism is in thermal equilibrium with the SiNW. This rules out non-thermal sources of noise such as 50 Ω Jhonson noise as a possible T_{1e} relaxation mechanism [24, 76].

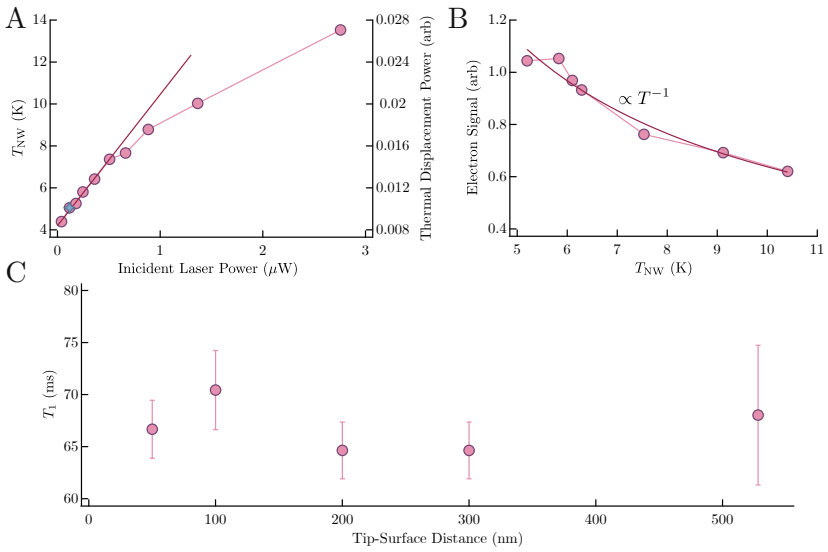


Figure 4.4: **Thermometry Meausurements for 1.3 mM Reference Sample. (A)** (right axis) measured thermal displacement power as a function of the incident laser power, (left axis) extrapolated SiNW temperature. The operating light level of the measurements for this sample is indicated by the blue data point. (**B**) Measurement of the thermal electron spin polarization as a function of the temperature of the SiNW. **(C)** T_{1e} measured at different tip-surface distances from the CFFGS. The T_{1e} remains consistent at different heights.

Conduction electrons in a metal can generate fluctuating electromagnetic fields from their random thermal motion (Johnson noise) which shorten the relaxation times of spins near the metal surface. [76]. We investigate whether Johnson noise from the CFGGS can affect the T_{1e} of electrons in the sample. Figure 4.4(C) shows the measured T_{1e} as a function of distance of the sample tip to the CFFGS. The figure reveals no variation in the spin-lattice relaxation time over the large variation in tip-surface distances examined. We thus rule out Johnson noise as a dominant relaxation mechanism.

4.4 Surface-Induced Spin-Lattice Relaxation

Bloembergen found in 1949 that paramagnetic impurities could cause relaxation of spins in the bulk sample via spin diffusion [38]. At the surface of the SiNW exists a Si/SiO_2 interface, where there are unterminated (dangling) bonds between the Si and SiO_2. These

paramagnetic defects are known to exhibit short spin-lattice relaxation times of order $T_d = 50$ μs [27, 28]. The surface defect density can be as high 10^{12} cm^{-2} or 10^{13} cm^{-2} [82–85]. To investigate the role the fast-relaxing paramagnetic defects have on the spin-lattice relaxation time of the bulk trityl-OX063 radicals, we conduct a semi-classical spin diffusion simulation that models the dipole-dipole interactions in a probabilistic manner and takes into account a variety of parameters such as the sample geometry, electron concentrations, lineshapes of the surface and bulk spins and is simulated for a range of surface defect densities.

As an overview of the details of the simulation, we begin by modelling the sample geometry based on images taken from a scanning electron microscope (SEM). We then generate a random realization of spin locations within the sample geometry according to the expected concentration of trityl radicals for the given sample and a range of surface defect densities ranging from 10^{10} cm^{-2} to 10^{14} cm^{-2}. In the model, we assume that the spin states are pointing along z such that they are either in the $|\uparrow\rangle$ or $|\downarrow\rangle$ state. The evolution of each spin is evolved according to 1) their dipole-dipole interactions with neighboring spins, and 2) the intrinsic bulk T_{1e} of the trityl radicals, and the T_{1d} of the paramagnetic defects. The spin states are evolved probabilistically, where the transition rates due to each of these mechanisms are calculated through a perturbative approach. A gradient-weighted magnetization is calculated at each time step to simulate the detection gradients generated by the CFFGS. The T_{1e} can be determined by fitting an exponential decay to the gradient-weighted magnetization as a function of time.

Firstly, the sample geometry is modelled using the scanning electron microscope (SEM) images shown in Figure 2.1. From the SEM images we approximate the size of the nanoscale droplets containing the trityl-OX063 radical, and their location on the SiNW. We then generate a spatially-random realization of spin locations by mapping a three-dimensional grid of points onto the given geometry, with grid spacing of $\Delta l = 1$ nm. It is assumed that the probability of a spin occupying different positions on the grid are statistically independent. Each point on the grid has a probability of $n_e\ \Delta l^3$ of containing a spin, where n_e is the concentration of OX063 listed in Table 2.1 under the assumption that the droplet contains no water. In the limit of $\Delta l \to 0$, the spatial distribution approaches a spatial Poison process with density n_e [86]. For the modelling the fast-relaxing defect spins, it is assumed they reside in a 1 nm thick layer on the SiNW, which is chosen to approximate the thickness of the Si/SiO_2 interface. The probability of a defect spin occupying a point on the grid in this region is $(\sigma_d/1\,\text{nm})\Delta l^3$ where σ_d is the surface density of paramagnetic defects. Python code for generating the spatial distribution of spins is provided in Appendix B.1.

For modelling the dynamics of the system, a probabilistic approach is taken. Transi-

tion rates between different spin states are governed by dipole-dipole interactions between nearby spins and the spin-lattice relaxation processes of the individual spins. Spin diffusion dynamics between a pair of electrons is governed by the secular dipolar Hamiltonian, $H_D = D(3S_1^z S_2^z - \mathbf{S_1} \cdot \mathbf{S_2})$, where $D = \mu_0 \hbar \gamma_e^2 (1 - 3\cos^2\theta)/(4\pi r^3)$ in angular frequency units, θ is the angle between static field and the line connecting the spin pairs, and r is the distance between the two spins. The transition rates from $|\uparrow\downarrow\rangle \leftrightarrow |\downarrow\uparrow\rangle$ states are calculated using Fermi's Golden Rule as follows [38, 87]. In the presence of a strong static external field, the Hamiltonian for a homonuclear two spin system is given by

$$H = \underbrace{-\omega_{01} S_1^z - \omega_{02} S_2^z}_{H_0} - H_D \tag{4.1}$$

where H_0 are the Zeeman terms for the two spins. The eigenstates of H_0 are $|\uparrow\downarrow\rangle, |\downarrow\uparrow\rangle$ with eigenvalues $(\omega_{02} - \omega_{01})/2, (\omega_{01} - \omega_{02})/2$ respectively. If $\|H_D\| \ll \|H_0\|$, then from Fermi's Golden Rule, we can calculate the transition probability per unit time as

$$\Gamma_{|\uparrow\downarrow\rangle \to |\downarrow\uparrow\rangle} = 2\pi |\langle\uparrow\downarrow | H_D | \downarrow\uparrow\rangle|^2 \, \delta(\omega_{02} - \omega_{01}) \tag{4.2}$$

The transition rate W is then calculated by integrating over ω_{01}, ω_{02} distributions. Assuming the distributions are statistically independent, the transition rate becomes

$$W = \int_{-\infty}^{\infty} d\omega_{01} \int_{-\infty}^{\infty} d\omega_{02} \, \Gamma_{|\uparrow\downarrow\rangle \to |\downarrow\uparrow\rangle} g_1(\omega_{01}) g_2(\omega_{02}) \tag{4.3}$$

$$W = 2\pi |\langle\uparrow\downarrow | H_D | \downarrow\uparrow\rangle|^2 \int_{-\infty}^{\infty} d\omega \; g_1(\omega) g_2(\omega), \tag{4.4}$$

with $g_1(\omega)$, $g_2(\omega)$ being the normalized inhomogeneous lineshapes where $\int_{-\infty}^{\infty} d\omega \; g_i(\omega) = 1$, $i \in \{1, 2\}$. $g_i(\omega)$ is assumed to have a Lorentzian lineshape with a full width at half maximum $\delta\omega = 2/T_{2e}^*$. Substituting

$$g_i(\omega) = \frac{2}{\pi \delta\omega_i} \frac{1}{1 + 4(\frac{\omega - \omega_{0i}}{\delta\omega_i})^2} \tag{4.5}$$

and $|\langle\uparrow\downarrow | H_D | \downarrow\uparrow\rangle|^2 = D^2/4$ into Equation 4.4 we have

$$W = 2\pi \underbrace{|\langle\uparrow\downarrow | H_D | \downarrow\uparrow\rangle|^2}_{\frac{D^2}{4}} \int_{-\infty}^{\infty} d\omega \; \frac{4}{\pi^2 \delta\omega_1 \delta\omega_2} \frac{1}{1 + 4(\frac{\omega - \omega_{01}}{\delta\omega_1)^2}} \frac{1}{1 + 4(\frac{\omega - \omega_{02}}{\delta\omega_2)^2}}, \tag{4.6}$$

which simplifies as

$$W = \frac{D^2}{\delta\omega_1 + \delta\omega_2 + 4\frac{(\omega_{01}-\omega_{02})^2}{\delta\omega_1+\delta\omega_2}}, \tag{4.7}$$

where ω_{01} and ω_{02} are the Larmor frequencies of the spins in the bulk and surface, where the center frequencies can be different owing to a difference in the distribution of g-factors for the two spin species [28]. In a given time interval Δt, the probability of a spin flip occurring is $\mathbb{P}(\text{flip}) = W\Delta t$. The time step Δt is chosen to be sufficiently small such that the maximum $\mathbb{P}(\text{flip}) \ll 1$, for all spin pairs in the sample. The number of spins in the simulated volume can be quite large ($\sim 700,000$), in which case calculating the pairwise interactions between all spins becomes intractable. The computation time can be reduced considerably by considering the interaction of only those spins within a *sphere of influence*, whose radius is chosen such that the dipole-dipole interaction between the central spin with spins outside the sphere is negligible [24].

The evolution due to the T_1 process is modelled probabilistically with $\mathbb{P}(|\uparrow\rangle \rightarrow |\downarrow\rangle) = 1 - p_e\Delta t/T_{1e}$ and $\mathbb{P}(|\downarrow\rangle \rightarrow |\uparrow\rangle) = p_e\Delta t/T_{1e}$ where p_e is the fractional polarization of the spins in $|\uparrow\rangle$ state at 6 K, and T_{1e} is the intrinsic spin lattice relaxation time of the trityl or defect spins measured inbulk concentrations from literature [25, 85, 88].

The initial state of the system is assumed to be in a pure state with all spins pointing up. At each time step, we iterate through all spin pairs and calculate the spin-flip probability $\mathbb{P}(\text{flip})$. Then, we generate a random number between 0 and 1. If this number is less than $\mathbb{P}(\text{flip})$ we flip the states of the spin pair. At each time step, the spin also undergoes a T_1 process, which may also induce a random spin flip. For simulating the T_1 we apply a similar methodology using probabilities $\mathbb{P}(|\uparrow\rangle \rightarrow |\downarrow\rangle)$ and $\mathbb{P}(|\downarrow\rangle \rightarrow |\uparrow\rangle)$, with the corresponding T_{1e} for the defect spins and OX063 radicals [25, 85]. Table 4.3 provides the parameters used for simulating samples A, B, and C as well as the 1.3 mM *reference sample* that was used for investigating different sources of electron relaxation, such as the height dependence of spin-lattice relaxation time. The procedure is executed K times with a time step of $\Delta t = 1$ ns. At each time step, after evaluating the spin states, we calculate the gradient-weighted polarization in the bulk sample and store the result in memory. The gradient-weighted polarization $p(t)$ is calculated as

$$p(t) = \frac{\begin{bmatrix} S_1(t) & \cdots & S_N(t) \end{bmatrix} \begin{bmatrix} G(\mathbf{r}_1) \\ \vdots \\ G(\mathbf{r}_N) \end{bmatrix}}{\sum_{i=1}^{N} G(\mathbf{r}_i)}, \tag{4.8}$$

where $S_i(t) \in \{-1, 1\}$ refers to the spin state (either down or up) at time t. $G(\mathbf{r}_i)$ is the detection gradient at the position of the i^{th} spin, and N is the number of spins in the bulk sample.

Table 4.3: **Parameters used for Semi-Classical Spin Diffusion Simulations.** Ref. sample refers to the 1.3 mM sample used for investigating different electron relaxation mechanisms.

Sample	**A**	**B**	**C**	**Ref. Sample**
Intrinsic $T_{1e\ \text{OX063}}$ (s)	0.1	0.1	0.1	10
Intrinsic $T_{1e\ \text{defects}}$ (µs)	50	50	50	50
OX063 Concentration (mM)	17.8	49.4	49.4	1.3
T_{2e}^* OX063 (ns)	38	27	42	56
T_{2e}^* defects (ns)	12	12	12	12

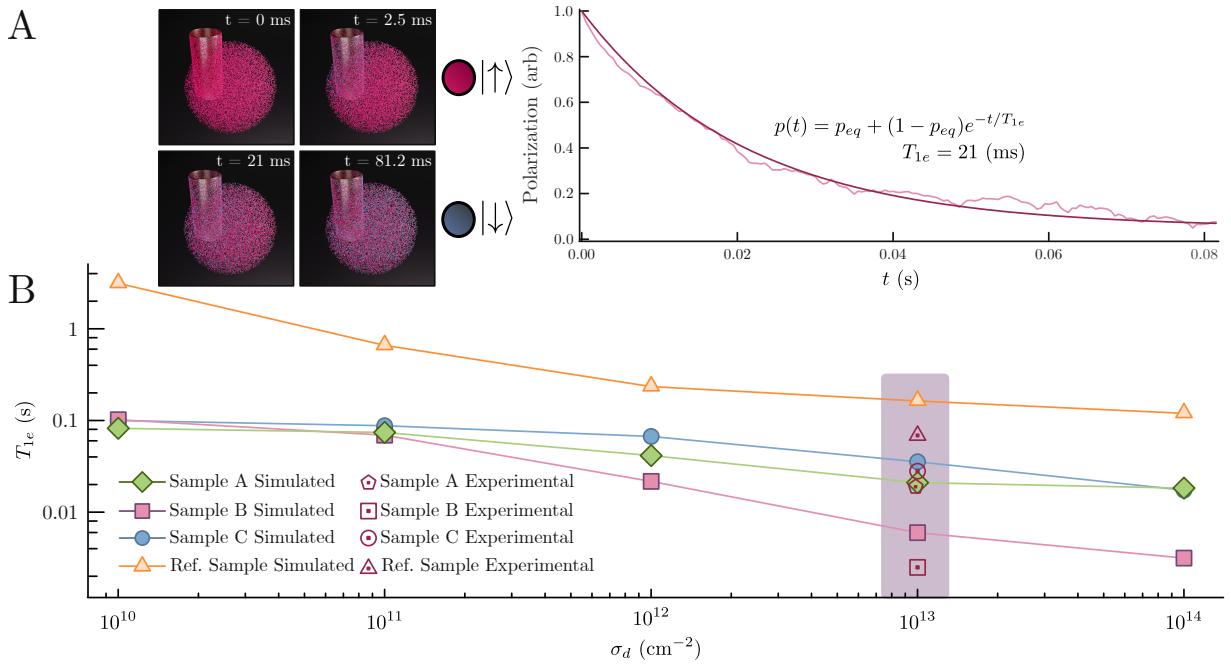


Figure 4.5: **Spin Diffusion Simulation of Surface Induced Spin Lattice Relaxation**. **(A)** Visualization of spin states at different points in T_{1e} decay for Sample A. At $t = 0$, the sample and surface defects are fully polarized. At $t = 2.5$ ms, the fast relaxing spins on the surface of the SiNW have reached thermal equilibrium. At $t = 21$ ms, the bulk polarization has reached the $1/e$ point, and we observe an increase in the number of spins in the down state. At $t = 81.2$ ms ($\sim 3T_{1e}$), the sample has reached thermal equilibrium. The simulated fractional polarization as a function of time for sample A is shown with $T_{1e} = 21$ ms. **(B)** Spin-lattice relaxation times for samples A, B, and C and the reference sample for different defect densities on the surface of the SiNW.

Figure 4.5 shows the simulated T_{1e} of the bulk trityls as a function of surface defect density σ_d for different sample geometries. With an expected surface density $\sigma_d = 10^{13}\,\mathrm{cm}^{-2}$, and spin-lattice relaxation time $T_{1d} = 50\ \mu s$ reported in literature, the experimental and simulated data sets show good agreement with one another [82–85]. Simulations of Sample B and Sample C, which were prepared with the same concentration of trityl-OX063, capture the large variation in T_{1e} that was measured in the experiment. The simulations reveal that the size, shape, and location of the droplet affect the observed relaxation rates. For small droplets containing a high number of spins in contact with the SiNW surface, the relaxation rates exhibit greater sensitivity compared to larger droplets, which have

minimal contact with the SiNW surface, as is the case with Samples B and C. Since the relaxation is mediated by spin diffusion, the greater the coupling to the environment, the larger the effect of cross-relaxation becomes. As a result, these simulations suggest that cross-relaxation with fast-relaxing paramagnetic defects on the surface of the SiNW are primarily responsible for the measured reduction in the T_{1e}.

4.4.1 Software and Hardware Implementation of Spin Diffusion Simulations

In this section, we provide an overview of the computational techniques used to perform the spin diffusion simulations. In particular, we focus on the details of the random number generation, which is used to evaluate the probabilities of spin flips at each simulation time step, as this was an extremely computationally intensive task. As previously noted, the simulated volume can contain a substantial number of spins, leading to a rapid increase in the number of spin pairs for which we must compute dipole-dipole mediated spin-flip transition rates. Given that the probability of spin flips diminishes significantly as the distance between spin pairs increases, we can reduce the computation burden by focusing only on spins with a defined sphere of influence around each spin. Interactions beyond this sphere are deemed negligible, and their spin flip rates are not computed. Despite this, the number of random numbers that need to be generated for the simulation can still be very large.

To understand the computational complexity, consider the following example: in our most dense samples, Samples B and C, the number of spins is roughly 700,000. This equates to approximately $40,000,000$ pairwise interactions between all spins that we consider in our simulation. For each spin pair (i, j), the probability of a spin flip is stored in a 1D array of floating point numbers (`flip_array`). An array of $40,000,000$ random numbers is generated for each time step in the simulation. These numbers are then compared to probabilities in `flip_array`. If the value of the random number is less than the probability of a flip, the spin states of the pair (i, j) are swapped. A similar procedure is followed for doing the T_1 flips. Given that the simulation time scales can be as large as 100 ms, and the simulation time step is 1 ns, the number of random numbers that need to be generated for evaluating these probabilities can be as large as 4×10^{15}.

In practice, we found that efficient generation of these large arrays of random numbers is computationally expensive and slow on central processing unit (CPU) based systems. To address this concern, the random number generation and spin-flip condition evaluations for each spin pair can be done in parallel to enhance the efficiency and speed of our simu-

lations. As a result, implementing the spin diffusion simulations on a graphics processing unit (GPU) offers significant advantages as GPUs are extremely well-suited for parallel computations, being able to evaluate functions across thousands of instances as compared to CPU systems which have limited parallel computation abilities.

In our simulations, we made use of NVIDIA® H100 Tensor Core GPUs for our spin diffusion simulations, where a mixture of Python and CUDA C++ programming languages was needed for the implementation. Although there exist Python packages that allow for interfacing with GPU hardware, such as PyTorch, TensorFlow, and PyCUDA, we found that none could match the performance requirements to the same degree as a native implementation of the simulation code using CUDA C++ code. CUDA is a programming language that enables easy interfacing with NVIDIA GPUs. As a result, a hybrid approach was used where Python was used to generate the random spatial distribution of the spins, as well as pre-computing binaries that contained a list of spin-flip probabilities, the locations of fast-relaxing and bulk spins, as well as the associated T_1s of each. CUDA code was used to generate and compare the random numbers for evaluating spin flips due to the T_1 process and the dipole-dipole interactions at each time step. It was also used to calculate the magnetization at each time step. Figure 4.6 provides a flow chart with a simplified overview of various tasks involved in performing the simulations. Appendix B.1 provides relevant Python code for generating the spins' random spatial distribution. Appendix B.2 contains relevant code for pre-computing the spin-flip probabilities for use in the CUDA code.

The CUDA code can be divided into three main components 1) generation of random numbers for evaluating spin flips, 2) comparing the generated random number with the spin-flip probability and swapping the state of the spins when necessary (`swap_spins` function) 3) comparing the generated random number with the probabilities associated with the T_1 process, and flipping the state when necessary (`apply_T1` function). Code for performing the spin flips due to dipole-dipole interactions `swap_spins`, and the T_1 process `apply_T1` are provided in the Appendix B.3. However, the main performance bottleneck in the simulations is the generation of random numbers.

In our CUDA code, we use the CURAND library, which provides various routines for implementing random number generators (RNGs). When generating large arrays of random numbers, it is important to minimize correlations in the RNG to ensure accuracy in the simulations. As a result, we use the Philox 4x32 generator with 10 rounds, which is known for its high performance while maintaining good statistical properties [89].

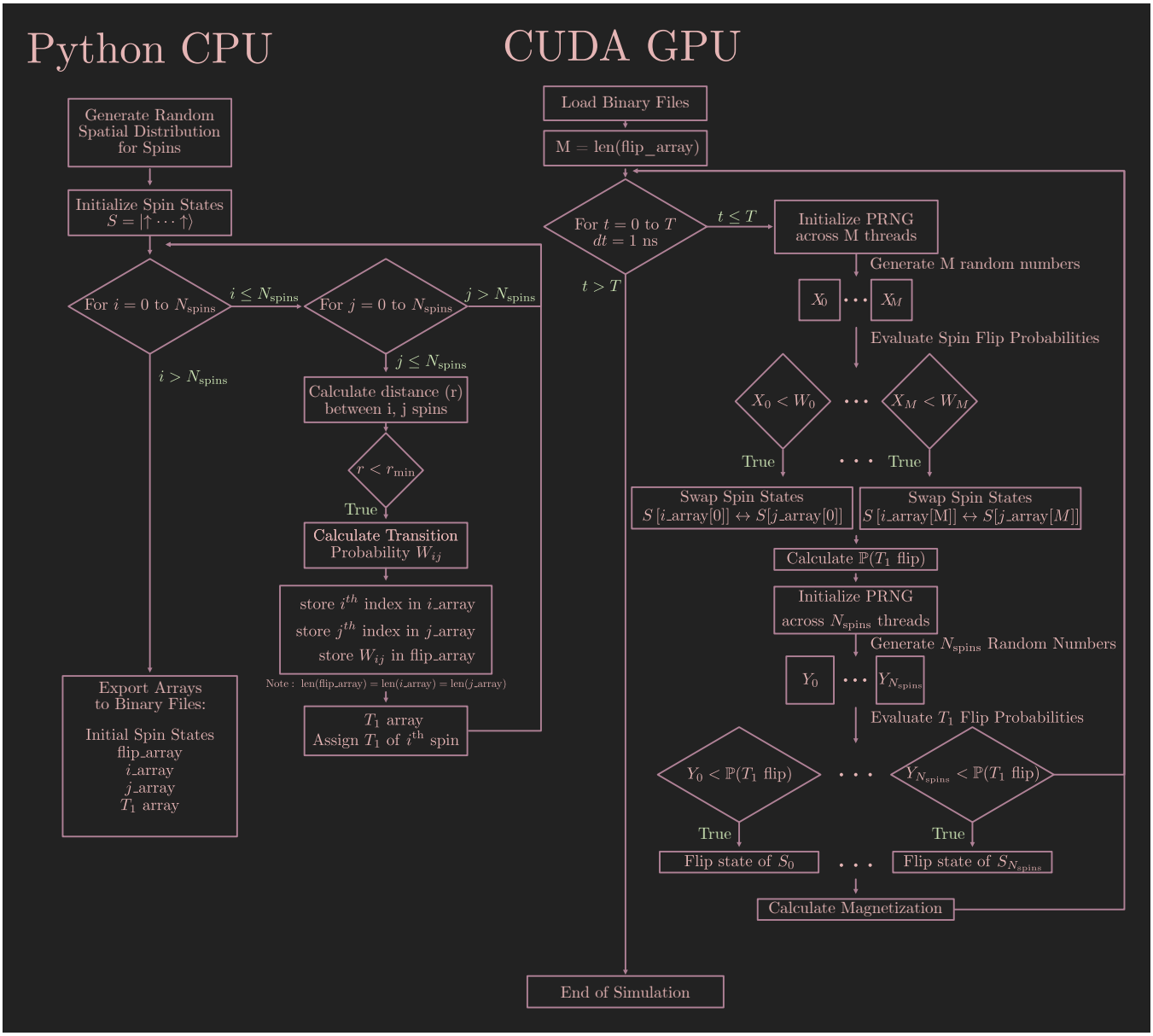


Figure 4.6: **Caption next page.**

Figure 4.6: (Previous page.) **Flow Chart of Simulation Code.** In the Python section, we pre-computed the dipole-dipole mediated transition probabilities for all spin pairs within a minimum radius $r_{\min}$ as described in Section 4.4, and store them in a 1D array (`flip_array`). We also stored the indices of the (i, j) interacting spin pairs for the corresponding transition probability. For example, the 0^{th} entry in `flip_array` may correspond to the probability of a spin flip between the 4^{th} and 10^{th} labelled spins in our geometry. As a result, the 0^{th} entry of `i_array` and `j_array` will be 4, and 10 respectively. We also assign each spin its own intrinsic T_1 based on whether the spin resides in the bulk sample or on the surface of the SiNW. The arrays are then exported to binary files. In the GPU program, we begin by loading the arrays from the binary files. The simulation is conducted for a simulation time T with step size $\delta t = 1$ ns. A pseudo-random number generator is then used to generate $M = \text{len}(\texttt{flip\_array})$ random numbers in parallel. The spin-flip conditions are also evaluated in parallel, where the spin states are swapped if the necessary conditions are met. A similar procedure was followed for evaluating spin flips due to the T_1 process. After each time step, the gradient-weighted magnetization is calculated and stored in a text file.

When programming the GPU for parallel computation, the architecture is organized into a hierarchy of thread groups made up of *thread blocks* and *grids* of blocks. A thread is the smallest sequence of instructions that can be executed. Contrary to a CPU, the GPU sacrifices the complexity and speed of a few individual threads to execute thousands of threads in parallel at lower speeds but with greater throughput. Each thread executes an independent instance of a function (also known as a kernel), such as generating a random number. Threads can be organized into larger groups known as blocks that execute together on the same physical core, which is optimized for sharing memory and synchronizing operations of different threads. In practice, there are limitations to how large a block can be based on the GPU architecture, and choosing different block sizes can affect the performance of the code depending on how data needs to be shared between threads in the simulation. We found that the optimal block size was made up of 256 threads. A collection of blocks that executes the kernel across multiple cores on the GPU is known as a grid. Grids are used to manage and synchronize the execution of thread blocks across multiple cores. The grid size in our simulation is set by the number of random numbers we need to generate. In our case, for each spin pair, we assign a unique thread that is responsible for generating its own independent stream of random numbers. These can then be used to evaluate the spin-flip probabilities at each time step. Figure 4.7 provides an overview of the GPU architecture. If there are N spin-flip probabilities in `flip_array`, then there will also be the same number of threads that will need to be

organized into the grid structure. If the block size is 256 threads, we calculate the grid size to be $N_{\text{blocks}} = (N + \text{blockSize} - 1)/\text{blockSize}$ which ensures that the block size is large enough even when N is not a multiple of the block size, where $N_{\text{threads}} = 256 \times N_{\text{blocks}} \geq N$.

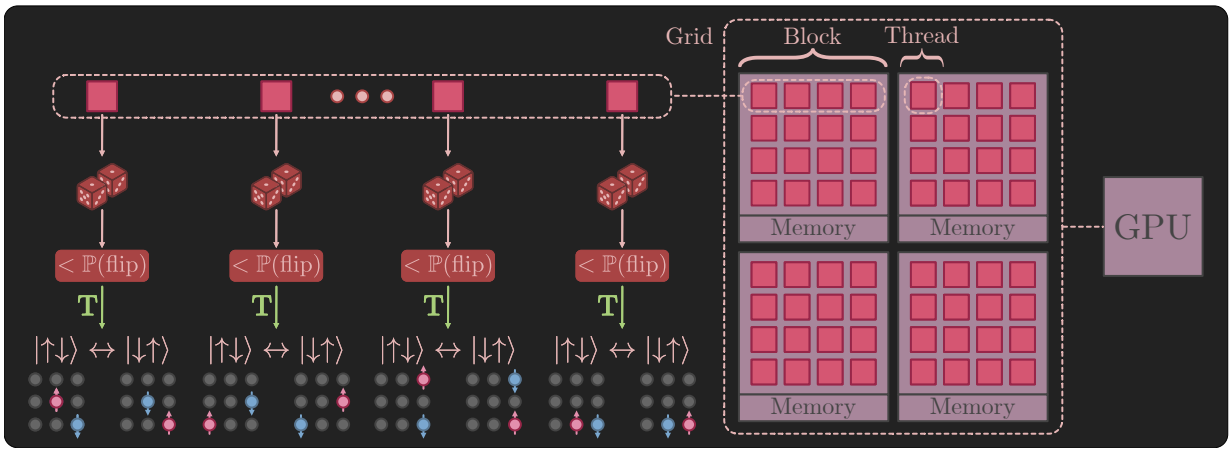


Figure 4.7: **Overview of GPU Architecture Schematic.** Each thread is responsible for generating its own stream of random numbers. The number of threads is equal to the number of pairwise interactions between the spins that are being considered in the simulation. Each random number X is compared to the $\mathbb{P}(\text{flip})$ of the spin pair. If $X < \mathbb{P}(\text{flip})$ then the spin states are swapped. Different threads are organized into thread blocks that share memory resources, and multiple blocks are organized into a grid.

The RNGs in our simulation are initialized by calling the `curand_init(seed, sequence_number, offset, &state)` kernel, which is responsible for initializing the state of the pseudorandom number generator (PRNG). The function arguments require that we pass an initial seed value, a sequence number, and an object which provides the memory address where the internal state variables of the RNG will be stored. As mentioned previously, we employ the Philox algorithm for the PRNG, which is a counter-based PRNG that generates random numbers based on the value of an internal counter. This counter increments with each call to the function, ensuring each number is unique and reproducible when the same initial conditions are used. The period of the Philox algorithm used is 2^{128}, where the period refers to the sequence of numbers that can be generated before a repeat occurs.

In the PRNG mentioned above the initial seed value is used to generate a deterministic random number sequence. This feature of the PRNG ensures that the same sequence of random numbers will always be generated given the same initial seed value. This has the advantage of providing reproducibility of the PRNG, which is useful for debugging

purposes. The `sequence_number` is used as a modifier for the initial seed value. It is the combination of the sequence number and the initial seed value that is responsible for the sequence of random numbers that will be generated from the GPU. When generating random numbers in parallel across multiple threads, even though the initial seed value is usually the same across all threads, by providing a unique sequence number for each, it allows for a statistically independent set of random numbers between threads to be generated.

When multiple threads use the same seed but different sequence numbers, they each produce a distinct stream of random numbers, thereby ensuring that no correlations occur between threads that could skew the simulation outcomes. The combination of a seed and a sequence number thus defines a unique random number stream per thread. Without unique sequence numbers, threads initialized with the same seed would generate identical sequences, leading to potential data correlation and biased results.

The `&state` variable in the `curand_init` kernel is a pointer to the memory address of the state variable, which stores initialization data, such as the initial seed, sequence number, internal counter state, as well as data associated with previous calls to the RNG. Each time the PRNG is called, the internal `state` of the PRNG needs to be updated. Updating the `state` refers to adjusting the internal counter and other elements of the PRNG in order to prepare for the next call to the kernel. Updating the state in this manner ensures continuous and independent random number generation across threads.

Each thread has its own state variable, allowing it to generate random numbers independently and asynchronously of other threads. Overall, this architecture of the PRNG ensures that each thread can execute independently and efficiently. Below, we have provided the code for initializing the Philox random number generator as well as a function that can be used to generate random numbers from a uniform distribution.

```
// Initialize CURAND states with Philox
__global__ void init_curand_states(curandStatePhilox4_32_10_t *state, unsigned long
↪   seed, int n) {
    int idx = threadIdx.x + blockIdx.x * blockDim.x;
    if (idx <  n) {
        curand_init(seed, idx, 0, &state[idx]);
    }
}
```

```cpp
// Generate random numbers using Philox
__global__ void generate_random_numbers(curandStatePhilox4_32_10_t *states, double *rand_nums, double *rand_num1, double *rand_num2, int n, int n_spin_values) {
    int idx = threadIdx.x + blockIdx.x * blockDim.x;
    if (idx < n) {
        curandStatePhilox4_32_10_t localState = states[idx];
        rand_nums[idx] = curand_uniform_double(&localState);
        if (idx < n_spin_values) {
            rand_num1[idx] = curand_uniform_double(&localState);
            rand_num2[idx] = curand_uniform_double(&localState);
        }
        states[idx] = localState;
    }
}
```

The CUDA code illustrated above initializes, and utilizes the Philox algorithm for generating random numbers. The codeidx variable is used to assign a unique thread across the different thread blocks, where `idx = threadIdx.x + blockIdx.x * blockDim.x`. This ensures that each thread in a given thread block is assigned a unique `idx` value. For example, the threads in block 0 will have an idx value ranging from 0 to 255, while threads in block 1 range from 256 to 511. This variable is then passed to the sequence number parameter of the `curand_init function`, guaranteeing that each thread generates a distinct sequence of random numbers.

In addition, to ensure independent and asynchronous generation of random number streams, each thread is also associated with its individual Philox state object (`&state[idx]`), which encapsulates all the necessary data for the PRNG, including the initial seed, sequence number, and the internal counter state.

The `generate_random_numbers` kernel uses these initialized states to generate 64-bit floating point numbers that are uniformly distributed. The kernel also keeps track of and updates the thread to ensure that on the next iteration of the simulation, state for each a new random number is generated. Also note that in our simulation we generate three distinct sets of random numbers in the simulation. The `rand_nums` variable has the same size as the `flip_array` and is utilized by the swap spins kernel for evaluating flip-flop interactions. The random numbers used for calculating a spin flip due to the T_1 process are stored in the variables `rand_num1` and `rand_num2`.

4.5 Conclusion and Outlook

The goal of this work was to demonstrate that force-detected magnetic resonance and high-efficiency pulsed dynamic nuclear polarization could be used together to improve the detection capabilities of magnetic resonance when detecting nanoscale spin ensembles. We showed that the thermal polarization of proton spins could be enhanced using DNP by a factor of ~ 100. Importantly, we demonstrated that in a 1D Fourier imaging experiment, this enhancement corresponded to a 204-fold reduction in acquisition time compared to measurements made with statistical polarization. In contrast to previous work done on incorporating DNP in MRFM, the platform discussed in this thesis provides a few advantages. Firstly, the use of a CFFGS for generating spin encoding and detection pulses allows for the application of efficient pulsed DNP methods for polarization transfer. Secondly, the platform has also been used for angstrom scale Fourier encoding of samples utilizing dynamical decoupling sequence to extend the spin coherence times during imaging [14, 22]. The combination of being able to do Fourier encoding of spins alongside dynamical decoupling sequences, ultrasensitive spin detection using SiNW force sensors, and large enhancement DNP is an important step to realizing high-resolution 3D imaging of nanoscale biological samples.

A contributing factor to the large enhancement factors measured, were the short T_{1e}s of the trityl-OX063 radicals. The reduced spin relaxation times were mediated by spin diffusion to paramagnetic defect spins on the surface of the SiNW. Simulations of the spin diffusion process provided good agreement with the measured spin-lattice relaxation data. The work also provided a detailed explanation for implementing these simulations on parallel computing hardware.

The work presented in this thesis provides a foundation for future experiments. Despite the progress made in being able to combine DNP with force-detected magnetic resonance there is room to further optimize the sensitivity and detection capabilities. One method for improving the sensitivity is by increasing the polarization of the spins by operating at lower temperature and higher static fields. For example, assuming the same DNP efficiency, operating at 0.3 K and 1 T would boost the SNR by a factor of 400 over measurements made using statistical polarization. Being able to perform 3D imaging in these conditions would require the development of new CFFGS devices that can support transmission of higher microwave frequencies as well as being able to generate uniform gradients in three directions for high-resolution 3D imaging.

References

[1] C. L. Degen, M. Poggio, H. J. Mamin, C. T. Rettner, and D. Rugar. Nanoscale magnetic resonance imaging. *Proceedings of the National Academy of Sciences*, 106(5):1313–1317, 2009.

[2] Albert W. Overhauser. Polarization of nuclei in metals. *Phys. Rev.*, 92:411–415, Oct 1953.

[3] Corinne E. Issac, Christine M. Gleave, Paméla T. Nasr, Hoang L. Nguyen, Elizabeth A. Curley, Jonilyn L. Yoder, Eric W. Moore, Lei Chen, and John A. Marohn. Dynamic nuclear polarization in a magnetic resonance force microscope experiment. *Phys. Chem. Chem. Phys.*, 18:8806–8819, 2016.

[4] Lloyd Lumata, Zoltan Kovacs, A. Dean Sherry, Craig Malloy, Stephen Hill, Johan van Tol, Lu Yu, Likai Song, and Matthew E. Merritt. Electron spin resonance studies of trityl ox063 at a concentration optimal for dnp. *Phys. Chem. Chem. Phys.*, 15:9800–9807, 2013.

[5] Jean-Paul Renaud, Ashwin Chari, Claudio Ciferri, Wen-ti Liu, Hervé-William Rémigy, Holger Stark, and Christian Wiesmann. Cryo-EM in drug discovery: achievements, limitations and prospects. *Nature Reviews Drug Discovery*, 17(7):471–492, July 2018.

[6] Gal Porat-Dahlerbruch, Amir Goldbourt, and Tatyana Polenova. Virus structures and dynamics by magic-angle spinning nmr. *Annual Review of Virology*, 8(1):219–237, 2021.

[7] J. M. Nichol, E. R. Hemesath, L. J. Lauhon, and R. Budakian. *Nanomechanical Detection of Nuclear Magnetic Resonance using a Silicon Nanowire Oscillator. Phys. Rev. B*, 85:054414, 2012.

[8] P. Maletinsky, S. Hong, M. S. Grinolds, B. Hausmann, M. D. Lukin, R. L. Walsworth, M. Loncar, and A. Yacoby. *A Robust Scanning Diamond Sensor for Nanoscale Imaging with Single Nitrogen-Vacancy Centres. Nat. Nanotechnol.*, 7(5):320–324, May 2012.

[9] J. M. Nichol, T. R. Naibert, E. R. Hemesath, L. J. Lauhon, and R. Budakian. *Nanoscale Fourier-Transform Magnetic Resonance Imaging. Phys. Rev. X*, 3:031016, 2013.

[10] T. Häberle, D. Schmid-Lorch, F. Reinhard, and J. Wrachtrup. *Nanoscale Nuclear Magnetic Imaging with Chemical Contrast. Nat. Nanotechnol.*, 10(2):125–128, Feb 2015.

[11] M. Kost, J. Cai, and M. B. Plenio. *Resolving Single Molecule Structures with Nitrogen-Vacancy Centers in Diamond. Sci. Rep.*, 5(1):11007, Jun 2015.

[12] D Rugar, R Budakian, H J Mamin, and B W Chui. Single spin detection by magnetic resonance force microscopy. *Nature*, 430(6997):329–332, July 2004.

[13] William Rose, Holger Haas, Angela Q. Chen, Nari Jeon, Lincoln J. Lauhon, David G. Cory, and Raffi Budakian. High-resolution nanoscale solid-state nuclear magnetic resonance spectroscopy. *Phys. Rev. X*, 8:011030, Feb 2018.

[14] Holger Haas, Sahand Tabatabaei, William Rose, Pardis Sahafi, Michèle Piscitelli, Andrew Jordan, Pritam Priyadarsi, Namanish Singh, Ben Yager, Philip J. Poole, Dan Dalacu, and Raffi Budakian. Nuclear magnetic resonance diffraction with subangstrom precision. *Proceedings of the National Academy of Sciences*, 119(40):e2209213119, 2022.

[15] J. A. Sidles, J. L. Garbini, K. J. Bruland, D. Rugar, O. Züger, S. Hoen, and C. S. Yannoni. Magnetic resonance force microscopy. *Rev. Mod. Phys.*, 67:249–265, Jan 1995.

[16] Y. Tao and C. L. Degen. *Single-Crystal Diamond Nanowire Tips for Ultrasensitive Force Microscopy. Nano Lett.*, 15(12):7893–7897, Dec 2015.

[17] M. Héritier, A. Eichler, Y. Pan, U. Grob, I. Shorubalko, M. D. Krass, Y. Tao, and C. L. Degen. *Nanoladder Cantilevers Made from Diamond and Silicon. Nano Lett.*, 18(3):1814–1818, Mar 2018.

[18] Pardis Sahafi, William Rose, Andrew Jordan, Ben Yager, Michèle Piscitelli, and Raffi Budakian. Ultralow dissipation patterned silicon nanowire arrays for scanning probe microscopy. *Nano Lett.*, 20(1):218–223, January 2020.

[19] M J Bereyhi, A Beccari, R Groth, S A Fedorov, A Arabmoheghi, T J Kippenberg, and N J Engelsen. Hierarchical tensile structures with ultralow mechanical dissipation. *Nature Communications*, 13(1):3097, June 2022.

[20] Y. Tao, A. Eichler, T. Holzherr, and C. L. Degen. *Ultrasensitive Mechanical Detection of Magnetic Moment using a Commercial Disk Drive Write Head. Nat. Commun.*, 7(1):12714, Sep 2016.

[21] H. J. Mamin, C. T. Rettner, M. H. Sherwood, L. Gao, and D. Rugar. *High Field-Gradient Dysprosium Tips for Magnetic Resonance Force Microscopy. Appl. Phys. Lett.*, 100(1):013102, Jan 2012.

[22] G.S. Boutis, P. Cappellaro, H. Cho, C. Ramanathan, and D.G. Cory. Pulse error compensating symmetric magic-echo trains. *Journal of Magnetic Resonance*, 161(2):132–137, 2003.

[23] Kent R Thurber, Lee E Harrell, and Doran D Smith. 170nm nuclear magnetic resonance imaging using magnetic resonance force microscopy. *Journal of Magnetic Resonance*, 162(2):336–340, 2003.

[24] Sahand Tabatabaei, Pritam Priyadarsi, Pardis Sahafi Namanish Singh, Daniel Tay, Andrew Jordan, and Raffi Budakian. Large-enhancement nanoscale dynamic nuclear polarization near a silicon nanowire surface. 2024. arXiv:2402.16283.

[25] Hanjiao Chen, Alexander G. Maryasov, Olga Yu. Rogozhnikova, Dmitry V. Trukhin, Victor M. Tormyshev, and Michael K. Bowman. Electron spin dynamics and spin–lattice relaxation of trityl radicals in frozen solutions. *Phys. Chem. Chem. Phys.*, 18:24954–24965, 2016.

[26] Yonatan Hovav, Akiva Feintuch, and Shimon Vega. Dynamic nuclear polarization assisted spin diffusion for the solid effect case. *The Journal of Chemical Physics*, 134(7):074509, February 2011.

[27] R. P. Wang. *Defects in Silicon Nanowires. Appl. Phys. Lett.*, 88(14):142104, 04 2006.

[28] A. Baumer, M. Stutzmann, M. S. Brandt, F. C.K. Au, and S. T. Lee. *Paramagnetic Defects of Silicon Nanowires. Appl. Phys. Lett.*, 85(6):943–945, 08 2004.

[29] Murali C. Krishna, Sean English, Kenichi Yamada, John Yoo, Ramachandran Murugesan, Nallathamby Devasahayam, John A. Cook, Klaes Golman, Jan Henrik

Ardenkjaer-Larsen, Sankaran Subramanian, and James B. Mitchell. Overhauser enhanced magnetic resonance imaging for tumor oximetry: Coregistration of tumor anatomy and tissue oxygen concentration. *Proceedings of the National Academy of Sciences*, 99(4):2216–2221, 2002.

[30] Maciej Serda, Yen-Ku Wu, Eugene D. Barth, Howard J. Halpern, and Viresh H. Rawal. Epr imaging spin probe trityl radical ox063: A method for its isolation from animal effluent, redox chemistry of its quinone methide oxidation product, and in vivo application in a mouse. *Chemical Research in Toxicology*, 29(12):2153–2156, 2016.

[31] Whylder Moore, Joseph E. McPeak, Martin Poncelet, Benoit Driesschaert, Sandra S. Eaton, and Gareth R. Eaton. 13c isotope enrichment of the central trityl carbon decreases fluid solution electron spin relaxation times. *Journal of Magnetic Resonance*, 318:106797, 2020.

[32] Jeffrey R. Brender, Shun Kishimoto, Gareth R. Eaton, Sandra S. Eaton, Yu Saida, James Mitchell, and Murali C. Krishna. Trehalose as an alternative to glycerol as a glassing agent for in vivo dnp mri. *Magnetic Resonance in Medicine*, 85(1):42–48, 2021.

[33] Michel Bauer, Raphael Chetrite, Kurusch Ebrahimi-Fard, and Frédéric Patras. Time-Ordering and a Generalized Magnus Expansion. *Letters in Mathematical Physics*, 103(3):Pas encore connu, 2012.

[34] F. J. Dyson. The radiation theories of tomonaga, schwinger, and feynman. *Phys. Rev.*, 75:486–502, Feb 1949.

[35] Fei Xue, D. P. Weber, P. Peddibhotla, and M. Poggio. Measurement of statistical nuclear spin polarization in a nanoscale gaas sample. *Phys. Rev. B*, 84:205328, Nov 2011.

[36] A Abragam and M Goldman. Principles of dynamic nuclear polarisation. *Reports on Progress in Physics*, 41(3):395, mar 1978.

[37] T. R. Carver and C. P. Slichter. Polarization of nuclear spins in metals. *Phys. Rev.*, 92:212–213, Oct 1953.

[38] N. Bloembergen. On the interaction of nuclear spins in a crystalline lattice. *Physica*, 15(3):386–426, 1949.

[39] Kong Ooi Tan, Michael Mardini, Chen Yang, Jan Henrik Ardenkjær-Larsen, and Robert G. Griffin. Three-spin solid effect and the spin diffusion barrier in amorphous solids. *Science Advances*, 5(7):eaax2743, 2019.

[40] T. V. Can, J. J. Walish, T. M. Swager, and R. G. Griffin. Time domain DNP with the NOVEL sequence. *The Journal of Chemical Physics*, 143(5):054201, 08 2015.

[41] S. R. Hartmann and E. L. Hahn. Nuclear double resonance in the rotating frame. *Phys. Rev.*, 128:2042–2053, Dec 1962.

[42] Chester F. Hwang and D. A. Hill. New effect in dynamic polarization. *Phys. Rev. Lett.*, 18:110–112, Jan 1967.

[43] Chester F. Hwang and Daniel A. Hill. Phenomenological model for the new effect in dynamic polarization. *Phys. Rev. Lett.*, 19:1011–1014, Oct 1967.

[44] Kan-Nian Hu, Vikram S. Bajaj, Melanie Rosay, and Robert G. Griffin. High-frequency dynamic nuclear polarization using mixtures of TEMPO and trityl radicals. *The Journal of Chemical Physics*, 126(4):044512, January 2007.

[45] Kong Ooi Tan, Ralph T Weber, Thach V Can, and Robert G Griffin. Adiabatic solid effect. *J. Phys. Chem. Lett.*, 11(9):3416–3421, May 2020.

[46] T. V. Can, R. T. Weber, J. J. Walish, T. M. Swager, and R. G. Griffin. Ramped-amplitude NOVEL. *The Journal of Chemical Physics*, 146(15):154204, 04 2017.

[47] A. Henstra and W.Th. Wenckebach. The theory of nuclear orientation via electron spin locking (novel). *Molecular Physics*, 106(7):859–871, 2008.

[48] Thorsten Maly, Galia T. Debelouchina, Vikram S. Bajaj, Kan-Nian Hu, Chan-Gyu Joo, Melody L. Mak–Jurkauskas, Jagadishwar R. Sirigiri, Patrick C. A. van der Wel, Judith Herzfeld, Richard J. Temkin, and Robert G. Griffin. Dynamic nuclear polarization at high magnetic fields. *The Journal of Chemical Physics*, 128(5):052211, February 2008.

[49] A Abragam and M Goldman. Principles of dynamic nuclear polarisation. *Reports on Progress in Physics*, 41(3):395, mar 1978.

[50] Changguo Tang and J. S. Waugh. Dynamics of classical spins on a lattice: Spin diffusion. *Phys. Rev. B*, 45:748–754, Jan 1992.

[51] C Ramanathan. Dynamic nuclear polarization and spin diffusion in nonconducting solids. *Applied Magnetic Resonance*, 34(3):409–421, August 2008.

[52] W. E. Blumberg. Nuclear spin-lattice relaxation caused by paramagnetic impurities. *Phys. Rev.*, 119:79–84, Jul 1960.

[53] GR Khutsishvili. Spin diffusion and magnetic relaxation of nuclei. *Sov. Phys. JETP*, 15:909, 1962.

[54] G R Khutsishvili. Spin diffusion. *Soviet Physics Uspekhi*, 8(5):743, may 1966.

[55] M. Goldman. Impurity-controlled nuclear relaxation. *Phys. Rev.*, 138:A1675–A1681, Jun 1965.

[56] Quentin Stern, Samuel François Cousin, Frédéric Mentink-Vigier, Arthur César Pinon, Stuart James Elliott, Olivier Cala, and Sami Jannin. Direct observation of hyperpolarization breaking through the spin diffusion barrier. *Science Advances*, 7(18):eabf5735, 2021.

[57] E. Philip Horvitz. Nuclear spin diffusion induced by paramagnetic impurities in nonconducting solids. *Phys. Rev. B*, 3:2868–2872, May 1971.

[58] A. R. King, J. P. Wolfe, and R. L. Ballard. Nmr of nuclei near a paramagnetic impurity in crystals. *Phys. Rev. Lett.*, 28:1099–1102, Apr 1972.

[59] J. P. Wolfe. Direct observation of a nuclear spin diffusion barrier. *Phys. Rev. Lett.*, 31:907–910, Oct 1973.

[60] A.D.A. Hansen and J.P. Wolfe. Measurement of the nuclear spin diffusion barrier around eu2+ ions in caf2. *Physics Letters A*, 66(4):320–322, 1978.

[61] Alessandro Chessari, Samuel F. Cousin, Sami Jannin, and Quentin Stern. Role of electron polarization in nuclear spin diffusion. *Phys. Rev. B*, 107:224429, Jun 2023.

[62] Guinevere Mathies, Sheetal Jain, Marcel Reese, and Robert G Griffin. Pulsed dynamic nuclear polarization with trityl radicals. *J. Phys. Chem. Lett.*, 7(1):111–116, January 2016.

[63] Michael Garwood and Lance DelaBarre. The return of the frequency sweep: Designing adiabatic pulses for contemporary nmr. *Journal of Magnetic Resonance*, 153(2):155–177, 2001.

[64] Sahand Tabatabaei, Holger Haas, William Rose, Ben Yager, Michèle Piscitelli, Pardis Sahafi, Andrew Jordan, Philip J. Poole, Dan Dalacu, and Raffi Budakian. Numerical engineering of robust adiabatic operations. *Phys. Rev. Appl.*, 15:044043, Apr 2021.

[65] Holger Haas, Daniel Puzzuoli, Feihao Zhang, and David G Cory. Engineering effective hamiltonians. *New Journal of Physics*, 21(10):103011, oct 2019.

[66] B. C. Stipe, H. J. Mamin, T. D. Stowe, T. W. Kenny, and D. Rugar. Noncontact friction and force fluctuations between closely spaced bodies. *Phys. Rev. Lett.*, 87:096801, Aug 2001.

[67] Seppe Kuehn, Roger F. Loring, and John A. Marohn. Dielectric fluctuations and the origins of noncontact friction. *Phys. Rev. Lett.*, 96:156103, Apr 2006.

[68] J. L. Garbini, K. J. Bruland, W. M. Dougherty, and J. A. Sidles. Optimal control of force microscope cantilevers. I. Controller design. *Journal of Applied Physics*, 80(4):1951–1958, 08 1996.

[69] M. Poggio, C. L. Degen, H. J. Mamin, and D. Rugar. Feedback cooling of a cantilever's fundamental mode below 5 mk. *Phys. Rev. Lett.*, 99:017201, Jul 2007.

[70] G. Turin. *An Introduction to Matched Filters. IRE Trans. Inf. Theory IEEE*, 6(3):311–329, 1960.

[71] Rose, William. *Nanoscale nuclear spin imaging: Dynamical decoupling and diffraction in a magnetic resonance force microscope*. PhD dissertation, University of Illinois at Urbana-Champaign, 2021.

[72] Johannes Herrmann, Christoph Hellings, Stefania Lazar, Fabian Pfäffli, Florian Haupt, Tobias Thiele, Dante Colao Zanuz, Graham J. Norris, Flavio Heer, Christopher Eichler, and Andreas Wallraff. Frequency up-conversion schemes for controlling superconducting qubits, 2022.

[73] S. W. Jolin, R. Borgani, M. O. Tholén, D. Forchheimer, and D. B. Haviland. Calibration of mixer amplitude and phase imbalance in superconducting circuits. *Review of Scientific Instruments*, 91(12):124707, December 2020.

[74] A. Demir, A. Mehrotra, and J. Roychowdhury. Phase noise in oscillators: a unifying theory and numerical methods for characterization. *IEEE Transactions on Circuits and Systems I: Fundamental Theory and Applications*, 47(5):655–674, 2000.

[75] W. B. Warren. Effects of local oscillator waveform on mixer spurious response levels. In *1966 Symposium Digest: 8th National Symposium on Electromagnetic Compatibility*, pages 1–4, 1966.

[76] S. Kolkowitz, A. Safira, A. A. High, R. C. Devlin, S. Choi, Q. P. Unterreithmeier, D. Patterson, A. S. Zibrov, V. E. Manucharyan, H. Park, and M. D. Lukin. Probing johnson noise and ballistic transport in normal metals with a single-spin qubit. *Science*, 347(6226):1129–1132, 2015.

[77] Peihao Huang and Xuedong Hu. Spin relaxation in a si quantum dot due to spin-valley mixing. *Phys. Rev. B*, 90:235315, Dec 2014.

[78] Brian Cowan. *Nuclear Magnetic Resonance and Relaxation*. Cambridge University Press, 1997.

[79] M Born and V Fock. Beweis des adiabatensatzes. *Zeitschrift für Physik*, 51(3):165–180, March 1928.

[80] Dominique Marion, Mitsuhiko Ikura, Rolf Tschudin, and Ad Bax. Rapid recording of 2d nmr spectra without phase cycling. application to the study of hydrogen exchange in proteins. *Journal of Magnetic Resonance (1969)*, 85(2):393–399, 1989.

[81] S. Meiboom and D. Gill. Modified Spin-Echo Method for Measuring Nuclear Relaxation Times. *Review of Scientific Instruments*, 29(8):688–691, 08 1958.

[82] K. L. Brower and T. J. Headley. *Dipolar Interactions Between Dangling Bonds at the (111) Si-SiO_2 Interface. Phys. Rev. B*, 34:3610–3619, Sep 1986.

[83] B. Nouwen and A. Stesmans. *Dependence of Strain at the (111) Si/SiO_2 Interface on Interfacial Si Dangling-Bond Concentration. Mater. Sci. Eng., A*, 288(2):239–243, 2000.

[84] R. Rurali. *Colloquium: Structural, Electronic, and Transport Properties of Silicon Nanowires. Rev. Mod. Phys.*, 82:427–449, Feb 2010.

[85] A Stesmans. *The .Si Identical to Si_3 Defect at Various (111)Si/SiO2 and (111) Si/Si_3N_4 Interfaces. Semicond. Sci. Technol.*, 4(12):1000, dec 1989.

[86] A. Papoulis and S.U. Pillai. *Probability, Random Variables, and Stochastic Processes*. McGraw-Hill, 2002.

[87] J. J. Sakurai and Jim Napolitano. *Modern Quantum Mechanics*. Cambridge University Press, 2 edition, 2017.

[88] J. Dalibard, Y. Castin, and K. Mølmer. *Wave-Function Approach to Dissipative Processes in Quantum Optics. Phys. Rev. Lett.*, 68:580–583, Feb 1992.

[89] John K. Salmon, Mark A. Moraes, Ron O. Dror, and David E. Shaw. Parallel random numbers: As easy as 1, 2, 3. In *SC '11: Proceedings of 2011 International Conference for High Performance Computing, Networking, Storage and Analysis*, pages 1–12, 2011.

[90] Jr-Shin Li, Justin Ruths, Tsyr-Yan Yu, Haribabu Arthanari, and Gerhard Wagner. Optimal pulse design in quantum control: A unified computational method. *Proceedings of the National Academy of Sciences*, 108(5):1879–1884, 2011.

[91] Mehran Kardar. *Statistical Physics of Particles*. Cambridge University Press, 2007.

[92] Rick Durrett. *Probability: Theory and Examples*. Cambridge Series in Statistical and Probabilistic Mathematics. Cambridge University Press, 5 edition, 2019.

[93] Haas, Holger. *Engineering Effective Hamiltonians for Magnetic Resonance*. PhD dissertation, University of Waterloo, 2019.

[94] T. J. Schmugge and C. D. Jeffries. High dynamic polarization of protons. *Phys. Rev.*, 138:A1785–A1801, Jun 1965.

APPENDICES

Appendix A

Expectation value of the Random Telegraph Function

Below we derive an expression for $\mathbb{E}[h(\mathbf{r},t)]$ as

$$\begin{aligned}\mathbb{E}[h(\mathbf{r},t)] &= \mathbb{P}[h(\mathbf{r},t)=1] - \mathbb{P}[h(\mathbf{r},t)=-1] \qquad \text{(A.1)}\\ &= \mathbb{P}[h(\mathbf{r},t)=1|h(\mathbf{r},0)=1]\mathbb{P}[h(\mathbf{r},0)=1]+\\ &\quad \mathbb{P}[h(\mathbf{r},t)=1|h(\mathbf{r},0)=-1]\mathbb{P}[h(\mathbf{r},0)=-1]-\\ &\quad \mathbb{P}[h(\mathbf{r},t)=-1|h(\mathbf{r},0)=1]\mathbb{P}[h(\mathbf{r},0)=1]-\\ &\quad \mathbb{P}[h(\mathbf{r},t)=-1|h(\mathbf{r},0)=-1]\mathbb{P}[h(\mathbf{r},0)=-1]. \qquad \text{(A.2)}\end{aligned}$$

For calculating the probabilities in the above equation, we know for a poisson distributed process over an interval $[0,t]$, $\mathbb{P}[n \text{ sign flips}] = e^{-rt}(rt)^n/n!$, where r is the spin flip rate [91, 92]. For the conditional probability

$$\begin{aligned}\mathbb{P}[h(\mathbf{r},t)=\pm 1 \mid h(\mathbf{r},0)=\pm 1] &= \mathbb{P}[\text{even sign flips in } [0,t]]\\ &= \mathbb{P}\left[\bigcup_{n=0}^{\infty}\{2n \text{ sign flips in } [0,t]\}\right] \qquad \text{(A.3)}\end{aligned}$$

Since the events are mutually exclusive Equation A.3 becomes

$$\begin{aligned}&\sum_{n=0}^{\infty} e^{-rt}\frac{(rt)^{2n}}{(2n)!} = e^{-rt}\cosh(rt)\\ &\implies \mathbb{P}[h(\mathbf{r},t)=\pm 1 \mid h(\mathbf{r},0)=\pm 1] = e^{-t/(2\tau_m)}\cosh(t/(2\tau_m)), \qquad \text{(A.4)}\end{aligned}$$

where we have defined the spin flip rate r as $r = 1/(2\tau_m)$. Following a similar methodology for the case where there are an odd number of spin flips in the interval

$$\mathbb{P}[h(\mathbf{r}, t) = \pm 1 \mid h(\mathbf{r}, 0) = \mp 1] = e^{-t/(2\tau_m)} \sinh\left(t/(2\tau_m)\right). \tag{A.5}$$

Substituting Equation A.4 and A.5 Equation A.2 becomes

$$\mathbb{E}[h(\mathbf{r}, t)] = m_0(\mathbf{r}) e^{-t/\tau_m}. \tag{A.6}$$

Appendix B

Code for Simulations of Surface Induced Spin Relaxation

B.1 Random Spatial Distribution of Spins

The following defines the geometry of the SiNW based on SEM images, and generates a random realization for the spins in the bulk, as well as for defect spins at SiNW surface, based on the expected volume and surface densities respectively.

```
# Import Libraries
import numpy as np
# Defining Geometry Boundaries
# Define the dimensions of the cuboid grid and the sphere
# Model the Sample Geometry as a Sphere with radius r taken from SEM Images and
↪  define coordinates on the grid
cuboid_dim_x = 601  # in nm
cuboid_dim_y = 601  # in nm
cuboid_dim_z = 500  # in nm
sphere_radius = 184  # in nm
grid_spacing = 1  # in nm

# Create a 3D grid with an even spacing of 1 nm
x = np.arange(0, cuboid_dim_x, grid_spacing)
y = np.arange(0, cuboid_dim_y, grid_spacing)
z = np.arange(0, cuboid_dim_z, grid_spacing)
grid = np.meshgrid(x, y, z, indexing='ij')
```

```
17
18  # Model the NW geometry and SiO2 layer as cylinders and define coordinates and
    ↪ place in the center of the grid
19  disc_radius = 60  # in nm
20  disc_height = 190  # in nm
21  disc_radius2 = 59  # in nm
22  disc_height2 = 190  # in nm
23  disc_radius3 = 59  # in nm
24  disc_height3 = 189  # in nm
25
26  # Create a 3D array for the disc
27  disc = np.where((grid[0] - cuboid_dim_x/2)**2 + (grid[1] - cuboid_dim_y/2)**2 <=
    ↪ disc_radius**2, 1, 0)
28  disc = np.where((grid[2] >= cuboid_dim_z/2+sphere_radius-disc_height) & (disc ==
    ↪ 1), 1, 0)
29
30  disc2 = np.where((grid[0] - cuboid_dim_x/2)**2 + (grid[1] - cuboid_dim_y/2)**2 <=
    ↪ disc_radius2**2, 1, 0)
31  disc2 = np.where((grid[2] >= cuboid_dim_z/2+sphere_radius-disc_height2) & (disc2 ==
    ↪ 1), 1, 0)
32
33  disc3 = np.where((grid[0] - cuboid_dim_x/2)**2 + (grid[1] - cuboid_dim_y/2)**2 <=
    ↪ disc_radius3**2, 1, 0)
34  disc3 = np.where((grid[2] >= cuboid_dim_z/2+sphere_radius-disc_height3) & (disc3 ==
    ↪ 1), 1, 0)
35
36  outer_shell = disc-disc2
37  bottom_shell = disc2-disc3
38  surface_shell = outer_shell+bottom_shell
39  # Calculate the distance of each point in the grid from the center of the cuboid
40  distances = np.sqrt((grid[0] - cuboid_dim_x/2)**2 + (grid[1] -
    ↪ cuboid_dim_y/2-100)**2 + (grid[2] - cuboid_dim_z/2-40)**2)
41
42  # Create a 3D array where the value is 1 where the sphere is and 0 outside the
    ↪ volume
43  array = np.where(distances <= sphere_radius, 1, 0)
44  spins_loc_vol = array - disc
45  # Assign values to each grid point corresponding to a possible location for either
    ↪ a Trityl or defect spin
46  # according to the previosuly defined geometries.
47  boundary_loc_vol = surface_shell
48  print("shape of spins_loc_vol: ", spins_loc_vol.shape)
49  print("shape of boundary_loc_vol: ", boundary_loc_vol.shape)
50
51
```

```
# Sample Mask is a boolean mask used to denote the possible locations of the spins
# The default grid size should be set to 1nm spacing for a volume that is 601nm *  601nm * 500nm (x,y,z)
# Boundary mask sets the location of the fast relaxing spins
# Boundary mask and Sample Mask should have the same dimensions
sample_mask =  spins_loc_vol
boundary_mask = boundary_loc_vol

# Generating a realization of the spins location in the Sample
# ps is the average desnity of trityl radicals in the volume
# l = is the length scale of the grid which 1nm
ps = 1.0744e25

prob_spin_loc = ps * ((1e-9)**3)
dist = np.random.rand(sample_mask.shape[0], sample_mask.shape[1],sample_mask.shape[2]) < prob_spin_loc

spins_mask = np.multiply(dist, sample_mask)
print('Probability of spins  = ',
        np.count_nonzero(spins_mask)/np.count_nonzero(sample_mask))
print('Number of spins in sample is ', np.count_nonzero(spins_mask))

# Generating a realization of the spins location in the Boundary
# pf is the average desnity of Fast relaxing spins  in the volume
# l = is the length scale of the grid which 1nm

pf = 1e26 #sigma = 1e17 /m^(-3)
prob_spin_loc_fast = pf * ((1e-9)**3)
dist_fast = np.random.rand(boundary_mask.shape[0],
                           boundary_mask.shape[1],
                           boundary_mask.shape[2]) < prob_spin_loc_fast
fast_spins_mask = np.multiply(dist_fast, boundary_mask)
print('Probability of spins in Boundary  = ',
        np.count_nonzero(fast_spins_mask)/np.count_nonzero(boundary_mask))
print('Number of spins in Boundary is ', np.count_nonzero(fast_spins_mask))


# If there is any overlap between spins in the Bulk and the Boundary
# replace with boundary spins.
# Merges the Sample and Boundary masks
# combined_spins has a 2 at the location of the fast relaxing spins
combined_spins = np.maximum(2*fast_spins_mask,spins_mask)
complete_spin_mask = np.where(combined_spins == 2, 1, combined_spins)
total_mask_elements = np.sum(complete_spin_mask)
# Create a boolean array self.spin_values that stores the spin values
```

```
# at any instant and populate it with the random initialization method
print('Mask Shape is', complete_spin_mask.shape)

# We assume the spins begin from a pure state
spin_values = np.multiply(
    complete_spin_mask,
    np.ones(complete_spin_mask.shape)
)

# Defines the indices at which the fast relaxing and slow spins are located
indices = np.where(combined_spins != 0)
indices_list = np.transpose(indices)
fast_indices = np.where(combined_spins == 2)
fast_indices_list = np.transpose(fast_indices)
slow_indices = np.where(combined_spins == 1)
slow_indices_list = np.transpose(slow_indices)
```

B.2 Pre-computing Spin Flip Probabilites

The following defines calculates an array of spin flip probabilities using Equation 4.7. We also assign an associated T_1 value for each spin in the sample. Both arrays are exported to binary files that can be imported by the GPU for use in simulations.

```
# Import Libraries
from scipy.spatial import cKDTree
from scipy.sparse import triu
from scipy.sparse import csr_matrix
import numba

# Define Simulation Parameters
delta_t = 0.000_000_005
# T2 denotes the time constant for an Exponential fit to the FID decay(Phosphorus T2 for ref timescale = 0.000280)
T2_fast_spin = 0.000000012 #12ns
T2_slow_spin = 0.000000038 #27ns
# T1_slow_spin denotes the intrinsic T1 for an electron with a concentration of 1.3mM
T1_fast_spin = 0.000_050
T1_slow_spin = 0.100_000 #100ms
```

```
pe =0.525 # Equilibrium population of spins in the up state

sphere_radius = 15 # Sphere of influence
inner_radius = 1

# Creates a sparse matrix conatining the distances of each spin pair in the sample within its own sphere of influcence.
@numba.jit(nopython=True)
def process_sparse_matrix(r_tri_csr_data, r_tri_csr_indices, r_tri_csr_indptr, indices_list, inner_radius, sphere_radius):
    norm = []
    elements = []
    interaction_list = []

    for i in range(len(r_tri_csr_indptr) - 1):
        start_idx = r_tri_csr_indptr[i]
        end_idx = r_tri_csr_indptr[i + 1]

        for j in range(start_idx, end_idx):
            distance = r_tri_csr_data[j]
            col_idx = r_tri_csr_indices[j]

            if inner_radius < distance < sphere_radius:
                norm.append(distance)
                elements.append(indices_list[col_idx] - indices_list[i])
                interaction_list.append((i, col_idx))

    return norm, elements, interaction_list

kdtree = cKDTree(indices_list)
r = kdtree.sparse_distance_matrix(kdtree, sphere_radius)
r_tri = triu(r)

# Convert r_tri to CSR format
r_tri_csr = csr_matrix(r_tri)
non_zero_count = r_tri_csr.nnz
print("Number of non-zero elements:", non_zero_count)

# Convert COO matrix to CSR format
r_tri_csr = r_tri.tocsr()
r_tri_csr_data = r_tri_csr.data
r_tri_csr_indices = r_tri_csr.indices
r_tri_csr_indptr = r_tri_csr.indptr
print("Making norm, elements and interaction_list")

```

```
# Process the sparse matrix
# norm is a 1D array of distances between each spin pair
# elements 2D array of [x,y,z] vectors. This is the vector of the line connecting the spin pairs
# interaction_list is a 2D array containing the indices of the spin pairs.
norm, elements, interaction_list = process_sparse_matrix(r_tri_csr_data, r_tri_csr_indices, r_tri_csr_indptr, indices_list, inner_radius, sphere_radius)

# Convert to numpy arrays if needed
norm = np.array(norm)
elements = np.array(elements)
interaction_list = np.array(interaction_list)
interaction_list = tuple(interaction_list.T)

print("making ccombined_spins")
ccombined_spins = np.copy(combined_spins)
ccombined_spins[np.where(ccombined_spins ==2)] = 0

# # Calculate Transition Rates of Spin Flips due to dipole-dipole interactions.
print("making spin_i, spin_j ")
spin_i = ccombined_spins[indices_list[interaction_list[0]][:,0],indices_list[interaction_list[0][:,1],i
spin_j = ccombined_spins[indices_list[interaction_list[1]][:,0],indices_list[interaction_list[1][:,1],i
dw1 = 2. / T2_slow_spin
dw2 = 2. / T2_fast_spin
w01 = 2. * np.pi * 9200000000
w02 = 2. * np.pi * 9219274501
fast_rate = ( 1 / (dw2 + dw2 + 4 * (( (w02- w02)**2) / (dw2 + dw2))))
slow_rate = ( 1 / (dw1 + dw1 + 4 * (( (w01- w01)**2) / (dw1 + dw1))))
fast_slow_rate = ( 1 / (dw1 + dw2 + 4 * (( (w01 - w02)**2) / (dw1 + dw2))))
ww = delta_t * ((2 * np.pi * 2.60194365867539 23e7 * (1 - 3 * (np.dot(elements,np.array([0, 0, 1])) / norm) ** 2) / (norm ** 3))**2)
w = fast_slow_rate * np.logical_xor(spin_i,spin_j) + slow_rate * np.logical_and(spin_i,spin_j) + 0*fast_rate * np.logical_and(np.logical_not(spin_i),np.logical_not(spin_j))

# Bloembergen_probabilities is a 1D array containing the probilities of spin a flip between the ith and jth spins
# len(interaction_list) = len() Bloembergen_probabilities)
# the ith entry of Bloemebergen_probabilities has a correspondin spin index pair recorded in interaction_list.

print("making Bloembergen_probabilities")
Bloembergen_probabilities = np.multiply(w,ww)
```

```
# bloembergen_matrix = np.zeros(r.shape)
# bloembergen_matrix[interaction_list]= Bloembergen_probabilities
ss = spin_values.astype(bool)[indices]
spin_values_temp = np.copy(ss)
ones_array = np.ones(ss.shape)


def subset_index_finder(subset_index, total_index_list):
    # Create a dictionary for the total index list
    index_dict = {(total_index_list[0][i], total_index_list[1][i],
    ↪  total_index_list[2][i]): i
                  for i in range(len(total_index_list[0]))}
    subset_index_loc = np.empty(len(subset_index[0]), dtype=np.int32)
    for i, coords in enumerate(zip(subset_index[0], subset_index[1],
    ↪  subset_index[2])):
        subset_index_loc[i] = index_dict.get(coords, -1)  # -1 if not found

    return subset_index_loc
# Records the locations of the slow and fast spins
fast_index_loc = subset_index_finder(fast_indices,indices)
slow_index_loc = subset_index_finder(slow_indices,indices)

# Assign each spin a T1 value depending on whethere it is fast spin or slow spin
# The T1 is used to evaluate spin flips in the CUDA code.
t1_indexed = np.zeros(ss.shape)
t1_indexed[fast_index_loc] = T1_fast_spin
t1_indexed[slow_index_loc] = T1_slow_spin

print(T1_slow_spin,T1_fast_spin,delta_t,ss[fast_index_loc].shape,ss[slow_index_loc].shape)

print(spin_values_temp.shape[0])
print(fast_indices_list.shape)
print(slow_indices_list.shape)
print(indices_list.shape)
print(fast_indices_list.shape[0]+slow_indices_list.shape[0])

# Exports the indices of the spin pairs, Associated Bloembergen_probabilities, the
↪  initial state of each spin,
# and the corresponding T1 asociated with each spin
#Truncate the array to include non zero entries
# ith spins indices
interaction_list_0 = interaction_list[0][np.where(Bloembergen_probabilities!=0)]
# jth spin indices
interaction_list_1 = interaction_list[1][np.where(Bloembergen_probabilities!=0)]
# Truncate non zero entries of array.
```

```
Bloembergen_probabilities = Bloembergen_probabilities[np.where(Bloembergen_probabilities!=0)]

# Type conversion
slow_index_loc_int64 = slow_index_loc.astype(np.int64)
bulk_mask_elements = spin_values_temp[slow_index_loc].shape[0]
bulk_mask_elements
spin_values_temp = spin_values_temp.astype(np.int64)
print(type(Bloembergen_probabilities[0]), type(interaction_list_0[0]), type(interaction_list_1[0]), type(spin_values_temp[0]), type(t1_indexed[0]), type(slow_index_loc_int64[0]))
print(Bloembergen_probabilities.shape, interaction_list_0.shape, interaction_list_1.shape, spin_values_temp.shape, t1_indexed.shape, slow_index_loc_int64.shape)
Bloembergen_probabilities, interaction_list_0, interaction_list_1, spin_values_temp, t1_indexed, slow_index_loc_int64

# File export
sigma = '1e17_100'
interaction_list_0.tofile(f'./{sigma}/interaction_list_0.bin')
interaction_list_1.tofile(f'./{sigma}/interaction_list_1.bin')
slow_index_loc_int64.tofile(f'./{sigma}/slow_index_loc.bin')
spin_values_temp.tofile(f'./{sigma}/spin_values_temp.bin')
Bloembergen_probabilities.tofile(f'./{sigma}/Bloembergen_probabilities.bin')
t1_indexed.tofile(f'./{sigma}/t1_indexed.bin')
```

B.3 Functions for Evolving the Spin States

The following section provides the functions used for evolving the spin states. `swap_spins` is the kernel used to for swapping the spin states due to dipole-dipole interactions. `apply_T1` is used for applying the T_1 relaxation process to each spin in the sample.

```
// Kernel for spin swapping
__global__ void swap_spins(double* d_Bloembergen_probabilities, long long* d_interaction_list_0, long long* d_interaction_list_1, long long* d_spin_values_temp, double* rand_nums, int size_Bloembergen) {
    int idx = threadIdx.x + blockIdx.x * blockDim.x;
    if (idx >= size_Bloembergen) return;

```

```
    double rand_num = rand_nums[idx];
    if (rand_num < d_Bloembergen_probabilities[idx]) {
        long long k = d_interaction_list_0[idx];
        long long l = d_interaction_list_1[idx];
        long long temp = d_spin_values_temp[k];
        d_spin_values_temp[k] = d_spin_values_temp[l];
        d_spin_values_temp[l] = temp;
    }
}

// Kernel for applying T1 relaxation
__global__ void apply_T1(long long* d_spin_values_temp, double* d_t1_indexed,
↪   double* rand_num1, double* rand_num2, double pe, double delta_t, int
↪   size_spin_values_temp) {
    int idx = threadIdx.x + blockIdx.x * blockDim.x;
    if (idx >= size_spin_values_temp) return;

    double t1_factor = (delta_t / d_t1_indexed[idx]);
    bool spin_val = (d_spin_values_temp[idx] != 0);
    bool new_spin_val = (!spin_val && (rand_num1[idx] < (pe * t1_factor)))
↪   (spin_val && (rand_num2[idx] >= ((1 - pe) * t1_factor)));
    d_spin_values_temp[idx] = new_spin_val ? 1 : 0;
}
```